Master's thesis

NTNU
Norwegian University of Science and Technology
Faculty of Natural Sciences
Department of Materials Science and Engineering

Kristina Dyrli Log

Band gap alterations of graphitic carbon nitride for photoelectrochemical water splitting

Master's thesis in Chemical Engineering and Biotechnology
Supervisor: Svein Sunde
Co-supervisor: Henrik Erring Hansen
June 2023

NTNU
Norwegian University of
Science and Technology

Kristina Dyrli Log

Band gap alterations of graphitic carbon nitride for photoelectrochemical water splitting

Master's thesis in Chemical Engineering and Biotechnology
Supervisor: Svein Sunde
Co-supervisor: Henrik Erring Hansen
June 2023

Norwegian University of Science and Technology
Faculty of Natural Sciences
Department of Materials Science and Engineering

NTNU
Norwegian University of
Science and Technology

Preface

This Master's thesis has been performed at the Department of Materials Science and Engineering (IMA) at the Norwegian University of Science and Technology (NTNU) in Trondheim during the spring of 2023. This work concludes five years in the study programme Chemical Engineering and Biotechnology at the respective university, with a specialization in Materials Chemistry and Energy Technology. The thesis is a continuation of a project performed during the fall of 2022 at the same department, with Professor Svein Sunde as my supervisor and PhD candidate Henrik Erring Hansen as my co-supervisor. As such, some of the theory regarding photoelectrochemistry might be similar. Additionally, some of the figures presented in the theory section are modifications of those used in the project.

I would like to thank my supervisor, Professor Svein Sunde, for all the offered help, guidance, suggestions, and explanations provided to me at our weekly meetings. This has helped a lot with my motivation and drive for the work performed in this thesis. Special thanks are also given to my co-supervisor, Henrik Erring Hansen, for always being available for questions, sharing his thoughts and knowledge, and guiding me with the experimental work in the laboratories. Additionally, he has helped me structure my report and provided valuable insights on what a well-written thesis should include. I would also like to thank all the people in the Electrochemistry group at the Department of Materials Science and Engineering, for their shared ideas and discussions, training, and general uplifting spirits. My time spent here would not have been the same without such a good and warm environment.

Lastly, I would like to give a big thank you to my parents, for always offering support and motivational speeches whenever it was needed. Furthermore, I would like to thank my fellow chemistry and non-chemistry friends for making these five years spent here in Trondheim some of my finest. You are the very best!

Trondheim, June 2023

Kristina Dyrli Log

Abstract

An important energy carrier for the future is hydrogen gas, where the development of efficient green production methods is an important step in minimizing the environmental impact of global warming. One such green method is photoelectrolysis of water, where the semiconductor graphitic carbon nitride (g-C_3N_4) can be used as the photocatalyst in the process due to its suitable band gap for water splitting. However, it is desirable to reduce the band gap to exploit more of the available light, thus increasing the H_2 yield of pristine g-C_3N_4. This means that modifications of the band gap through doping could help improve it. In this work we demonstrate that a higher photocatalytic activity was obtained at an acidic pH by doping g-C_3N_4 with boron, due to a reduced band gap and thus more utilization of the incoming light. Boron-doped g-C_3N_4 was synthesized in a simple heating process from $NaBH_4$, and the resulting band gaps were measured using diffuse reflectance spectroscopy. The potentials of the band edges at different pH were found using the Mott Schottky analysis and by investigating the current response of the semiconductor when exposed to the $Fe(CN)_6^{3-/4-}$ redox couple. The target reaction used to measure the photocatalytic efficiency was the oxidation of methyl orange upon illumination. It was found that heavily boron-doped g-C_3N_4 proved to be roughly 2% more efficient than pristine g-C_3N_4 for a pH of 0.3, but pristine g-C_3N_4 proved more efficient than the boron-doped samples for an increased pH. This was likely due to a higher obtained driving force for the oxidation of methyl orange for boron-doped g-C_3N_4 compared to pristine g-C_3N_4 at a pH of 0.3, due to the effect of band edge unpinning upon illumination. At an increased pH, the effect of band edge unpinning upon illumination was likely not enough to compensate for the increasing cathodic potential of the valence bands, which was most prominent for the heavily boron-doped samples.

Sammendrag

En viktig energibærer for framtiden er hydrogengass, hvor utviklingen av effektive grønne produksjonsmetoder er nødvendig for å minimere miljøpåvirkningen av global oppvarming. En slik metode er fotoelektrolyse av vann, hvor halvlederen grafittisk karbonnitrid (g-C_3N_4) kan brukes som fotokatalysatoren i prosessen på grunn av sitt godt egnede båndgap for splitting av vann. Det er derimot ønskelig å redusere båndgapet slik at man kan utnytte mer av lyset og dermed øke utbyttet av hydrogengass sammenlignet med rent g-C_3N_4. Dette betyr at modifikasjoner av båndgapet gjennom doping kan forbedre utbyttet. I dette arbeidet demonstrerer vi at en høyere fotokatalytisk aktivitet blir oppnådd ved en sur pH for bordopet g-C_3N_4, på grunn av det reduserte båndgapet og dermed også høyere utnyttelse av lyset. Bordopet g-C_3N_4 ble syntetisert fra $NaBH_4$ i en enkel oppvarmingsprosess og det resulterende båndgapet ble målt ved hjelp av diffus reflektansspektroskopi. Potensialene til båndkantene ved forskjellig pH ble funnet ved hjelp av Mott Schottky-analyse og undersøkelser av strømresponsen til halvlederen ved eksponering for $Fe(CN)_6^{3-/4-}$ redoksparet. Målreaksjonen som ble brukt til å måle den fotokatalytiske effektiviteten var oksidering av metyloransje ved belysning. Resultatene viste at bordopet g-C_3N_4 var rundt 2 % mer effektiv enn rent g-C_3N_4 ved en pH på 0,3, men rent g-C_3N_4 ble mer effektiv enn de bordopede prøvene for høyere pH-verdier. Dette var mest sannsynlig et resultat av løsnede båndkanter ved belysning for bordopet g-C_3N_4 sammenlignet med rent g-C_3N_4, som førte til en høyere drivkraft for oksideringen av metyloransje ved en pH på 0,3. Ved en økt pH var nok ikke effekten av løsnede båndkanter ved belysning nok til å kompensere for et økende katodisk potensial hos valensbåndene, som økte betydelig for de bordopede prøvene.

Contents

List of terms and abbreviations

ATR Attenuated Total Reflection

B300Air Boron-doped g-C_3N_4 at 300°C in a synthetic air atmosphere

B500Air Boron-doped g-C_3N_4 at 500°C in a synthetic air atmosphere

B500Argon Boron-doped g-C_3N_4 at 500°C in an argon atmosphere

BF Bright Field

CB Conduction Band

CE Counter Electrode

CV Cyclic Voltammetry

DI water Deionized water

DRS Diffuse Reflectance Spectroscopy

EDS Energy-Dispersive X-ray Spectroscopy

eV Electron Volt

$Fe(CN)_6^{3-/4-}$ Ferricyanide/Ferrocyanide

FTIR Fourier Transform Infrared

g-C_3N_4 Graphitic carbon nitride

HER Hydrogen Evolution Reaction

HOMO Highest Occupied Molecular Orbital

IPCE Incident Photon-to-electron Conversion Efficiency

LSV Linear Sweep Voltammetry

LUMO Lowest Unoccupied Molecular Orbital

MO Methyl Orange

OCP Open Circuit Potential

OER Oxygen Evolution Reaction

PZC Potential of Zero Charge

RDE Rotating Disk Electrode

RE Reference Electrode

RhB Rhodamine B

SE Secondary Electrons

S(T)EM Scanning (Transmission) Electron Microscopy

VB Valence Band

WE Working Electrode

XRD X-Ray Diffraction

List of Figures

List of Tables

1 Introduction

The world's energy supply is currently dominated by fossil fuels such as oil and gas, which contribute to global warming. Luckily, the incentive for developing sustainable and renewable energy is growing, where the purpose is to reduce the future effects of global warming. Such a focus has even been emphasized in UN's Sustainable Development Goals 7 and 13 [1]. A promising sustainable and renewable energy carrier is green hydrogen gas. However, this energy carrier is only sustainable if the production method is also sustainable. As most hydrogen gas today is produced by fossil fuels, the development of efficient green production methods is of great importance [2]. One such method is photoelectrolysis, where sunlight provides the energy to split water into hydrogen and oxygen gas [3].

If photoelectrolysis is to be used as a viable option for the production of hydrogen gas, the semiconductor used to convert sunlight into current must be photocatalytically efficient. Graphitic carbon nitride, g-C_3N_4, is a semiconductor that has been recently investigated for this purpose, due to its suitable band gap for water splitting [4]. Additionally, it has a high thermal and chemical stability to oxidation, is metal-free, and is amenable to large-scale synthesis. However, it is desirable to reduce the band gap to exploit more of the available light and thus hopefully increase the H_2 yield [5]. As g-C_3N_4 can be readily doped, incorporation of a dopant into the lattice could achieve such a reduction in the band gap. Zhao et al. demonstrated the successful doping of g-C_3N_4 with boron for a more efficient oxygen evolution reaction [6]. They found that the band gap was reduced with increasing dopant concentration, with band edges moving towards more anodic potentials and thus a higher driving force for oxygen evolution. Wen et al. also reported a reduced band gap and slightly more anodic potential for the conduction band after doping g-C_3N_4 with boron, which resulted in a more efficient hydrogen evolution [7].

As a step towards optimizing g-C_3N_4 for hydrogen production, the ability of g-C_3N_4 to oxidize methyl orange is studied, as this is more convenient to measure compared to the hydrogen evolution. Methyl orange is an organic dye that pollutes waste waters, meaning that g-C_3N_4 can degrade the dye to a less hazardous compound through oxidation reactions [8]. Increased photocatalytic activity of doped g-C_3N_4 towards methyl orange oxidation is expected compared to pristine g-C_3N_4, as the electronic structure of the band gap and the occurrence of band edge unpinning is thought to be influenced by the introduced dopants.

In this work, the photocatalytic degradation of methyl orange was investigated using boron-doped g-C_3N_4. Different doping conditions were examined for the methyl orange degradation to elucidate the semiconductor properties responsible for the photocatalytic degradation. The semiconductor properties including band edges were measured using the Mott Schottky analysis and the current response of the semiconductor when exposed to the $Fe(CN)_6^{3-/4-}$ redox couple. Furthermore, the band gaps were obtained using diffuse reflectance spectroscopy. The obtained positions of the energy bands and the sizes of the band gaps were then correlated to the methyl orange degradation.

2 Theory

2.1 Photoelectrochemistry

2.1.1 Band theory and the semiconductor-electrolyte interface

In a semiconductor, it is the mobility of electrons that provides electronic conductivity [9, p. 36-41]. The electrons are located in atomic orbitals, and for neighboring atoms, these orbitals will overlap and create molecular orbitals. For metallic solids, the number of these overlaps is high enough to provide a continuum, which creates energy bands. Energy bands are separated by gaps of forbidden energy, called band gaps, which is demonstrated in Figure 2.1.

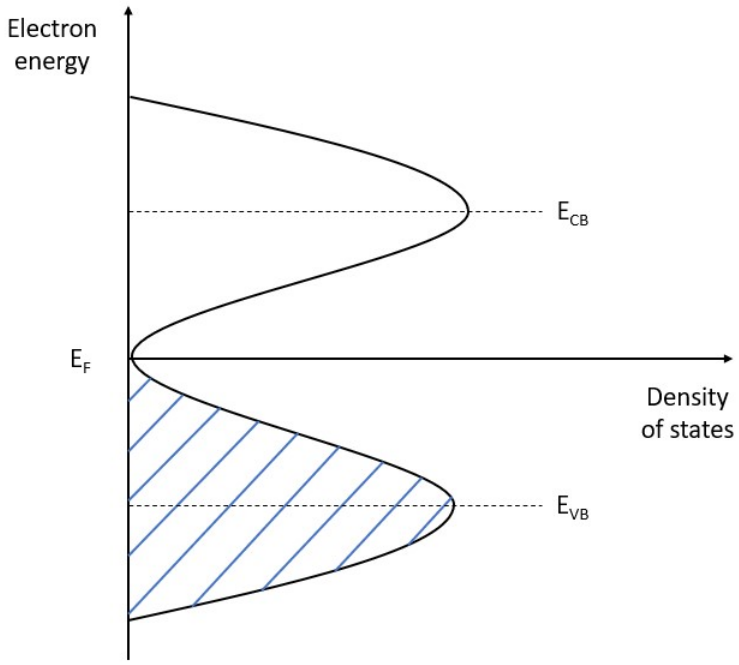

Figure 2.1: Density of states as a function of electron energy for the conduction band and the valence band for an intrinsic semiconductor. The conduction band is unoccupied and the valence band is occupied, as demonstrated by the hatched region. The Fermi level E_{F} is located in the band gap.

The conduction band (CB) and the valence band (VB) separate the band gap in a semiconductor [9, p. 399-409]. It is the lowest unoccupied molecular orbital (LUMO) that forms the conduction band, and the highest occupied molecular orbital (HOMO) that forms the valence band. The band gap determines the required energy to excite an electron from the valence band to the conduction band, and this energy difference is measured in eV and termed E_{g}. In an intrinsic semiconductor, the Fermi level E_{F} lies close to the center of the band gap [10, p. 13-14].

The Fermi level provides the uppermost energy level occupied with electrons at 0 K, which is shown in Figure 2.1. In an extrinsic semiconductor, impurities known as dopants are deliberately introduced to the crystal lattice. In this case, the Fermi level thus depends on the amount and type of doping [10, p. 14-15]. For an n-type semiconductor, where the majority charge carriers are electrons, the Fermi level will be located closer to the conduction band. Similarly, for a p-type semiconductor where the majority charge carriers are holes, the Fermi level will be located closer to the valence band.

When a semiconductor and an electrolyte solution containing a redox pair is in contact, the formation of three different double layers on the semiconductor-electrolyte interface occurs [3]. The one furthest away from the semiconductor is the Gouy-Chapman diffuse double layer, which can be neglected for sufficiently high ion concentrations. Furthermore, the Helmholtz layer is formed by the adsorption of molecules or ions on the semiconductor surface. Lastly, the space charge double layer forms due to the minority charge carriers being distributed a finite distance below the surface of the semiconductor. The developed potential difference across this nanometer-wide space charge layer, denoted as ϕ_{sc}, will appear as a bending of the energy bands corresponding to $e\phi_{sc}$. For a given Fermi level of the electrolyte, this is demonstrated in Figure 2.2 for n- and p-type semiconductors. As a result of the Fermi level of the semiconductor and the electrolyte solution aligning at equilibrium, the respective energy bands will bend upwards and downwards.

In an electrolyte containing a redox pair, the bending of these bands can be tuned by adjusting the electrode potential [11, p. 289-290]. When equilibrium between the semiconductor and the electrolyte solution is reached, the Fermi levels align and as a result, the energy bands in the semiconductor bend either upwards or downwards. By applying a potential, one could separate these Fermi levels and thus inhibit band bending. The required potential to flatten the energy bands is known as the flat band potential, which may correspond to the conduction band of a heavily doped n-type semiconductor and the potential of zero charge (PZC) for a traditional electrode.

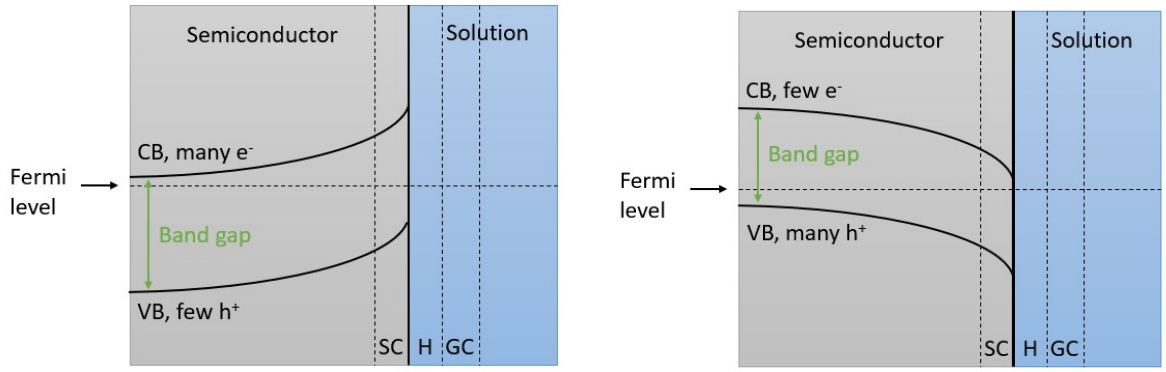

Figure 2.2: Band bending at equilibrium of a) n-type semiconductor and b) p-type semiconductor for a given Fermi level of the electrolyte. For the n-type, the Fermi level of the semiconductor was originally located at a higher potential than the Fermi level of the electrolyte, causing the bands to bend upwards and electrons to be depleted from the conduction band [11, p. 289]. This forms a positive space charge and thus enrichment of holes in the valence band. For the p-type semiconductor, the opposite is true due to the Fermi level of the semiconductor being originally located at a lower potential than the Fermi level of the electrolyte. Furthermore, the Gouy-Chapman diffuse double layer, the Helmholtz layer, and the space charge double layer are illustrated and denoted GC, H, and SC, respectively.

The flat band potential may depend on the pH of the solution, as the pH affects the amount of adsorbed protons and hydroxide ions on the semiconductor surface [12]. This affects the potential drop in the Helmholtz layer, which in turn affects the amount of band bending. When the amount of band bending is decreased, a lower potential is required to flatten the bands [13]. Similarly, an increased band bending results in a higher required potential to flatten the bands. At low pH-values, protons are adsorbed on the semiconductor surface, which lowers the work related to adding one electron from the solution into the semiconductor. Thus, the energy bands are located at lower energies on the vacuum scale for lower pH-values. At higher pH-values, protons are replaced by hydroxide ions, which increases the work related to adding one electron from the solution into the semiconductor, thus placing the band edges at higher energies on the vacuum scale.

For oxide containing semiconductors in aqueous solution, this pH dependence is in most cases a Nernstian one, such as for the hydrogen evolution reaction and the oxygen evolution reaction [12]. Here, the flat band potential decreases with around 59 mV per pH unit due to the surface deprotonation.

2.1.2 Photocatalytic water splitting

The use of photoelectrolysis to split water, where the necessary energy is provided by sunlight, has been researched since the 1970s [3]. For a semiconductor-electrolyte interface, the incoming light creates electron-hole pairs that are separated by an electric field. The resulting electrons reduce water into hydrogen gas at the cathode according to the hydrogen evolution reaction (HER);

$$\begin{aligned} 2\,H_2O + 2\,e^- &= H_2\,(g) + 2\,OH^-, \text{ Alkaline solution} \\ 2\,H^+ + 2\,e^- &= H_2\,(g), \text{ Acidic solution} \end{aligned} \tag{2.1}$$

and the respective holes oxidize water into oxygen gas at the anode according to the oxygen evolution reaction (OER);

$$\begin{aligned} 4\,OH^- &= O_2\,(g) + 2\,H_2O + 4\,e^-, \text{ Alkaline solution} \\ 2\,H_2O &= O_2\,(g) + 4\,H^+ + 4\,e^-, \text{ Acidic solution} \end{aligned} \tag{2.2}$$

There are several conditions that need to be fulfilled when a semiconductor in an electrolyte is used to split water. The first condition concerns the size of the band gap, which must be between 1.23 eV and 3.0 eV [14]. As the potential difference between the HER and the OER is equal to 1.23 V, this corresponds to the theoretical energy needed for water splitting. This means that photons from the incoming light must have a minimum energy of 1.23 eV, which thus provide the lower limit of the band gap. The upper limit of the band gap is related to a low number of generated charge carriers from the reduced amount of excited electrons. The second condition concerns the positions of the CB and VB. The generated electrons from the CB can only reduce water into hydrogen gas if the CB of the semiconductor has a more cathodic potential than the electrode potential of the HER (0 V_{RHE}) [14][15]. This is when electronic energies of the energy bands are converted to electrode potential. Similarly, holes from the VB can only oxidize water into oxygen gas if the VB of the semiconductor has a more anodic potential than the electrode potential of the OER (1.23 V_{RHE}). This is demonstrated in Figure 2.3, where the band edges of three known semiconductors are presented. Here, g-C_3N_4 is the only suitable photocatalyst for water splitting due to the positions of the band edges.

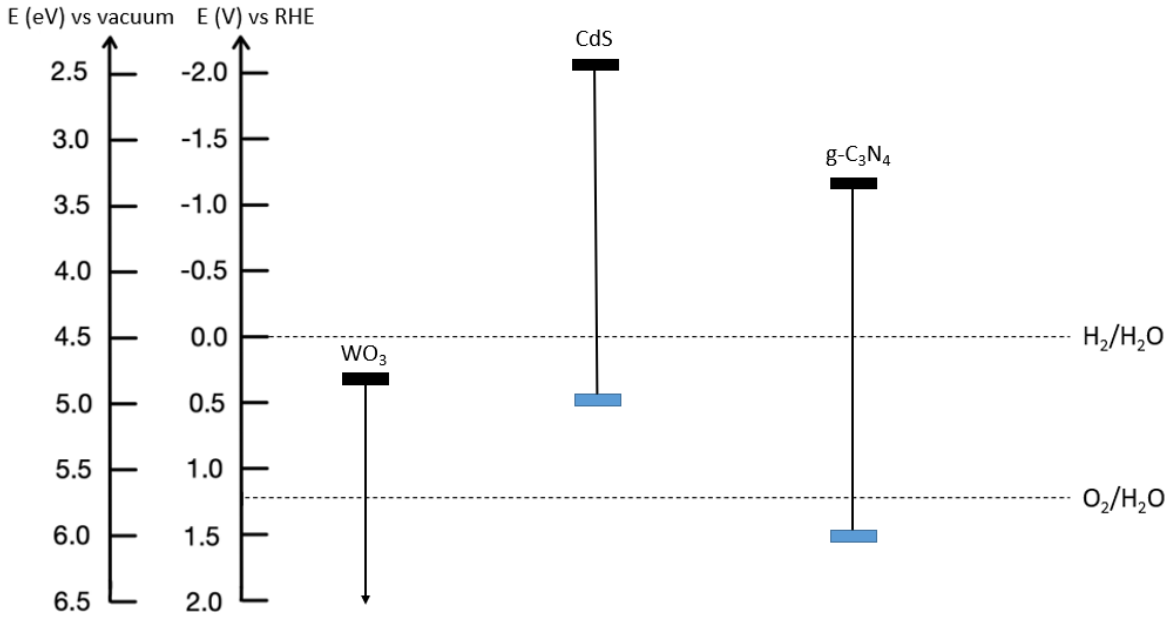

Figure 2.3: Band edges of three different photocatalysts, related to water splitting; WO_3, CdS, and g-C_3N_4. Due to the positions of the band edges relative to the hydrogen evolution reaction and the oxygen evolution reaction, WO_3 and CdS are not suitable for water splitting, but g-C_3N_4 is. Illustration inspired by [16].

In terms of the overpotential related to the HER and OER, the band gap size is important. The overpotentials, in this case, are only dependent on the band gap, the band edges, and the redox potentials of the HER and OER [3]. In Figure 2.3, g-C_3N_4 display a high overpotential for the HER, which indicates a high driving force for the reaction. However, the figure also displays a lower overpotential and thus driving force for the OER, which implies the OER as the rate-limiting reaction in this process. When considering the overpotential in addition to the generation of charge carriers, the optimal size of the band gap for water splitting is not too narrow and not too wide. A too narrow band gap will result in low overpotentials and thus driving forces for the HER and OER, whilst a too wide band gap will result in a low number of charge carriers and thus a low photocatalytic efficiency.

Another aspect to consider regarding photocatalytic efficiency is loss mechanisms related to the generated charge carriers. The charge carriers need to be transported to the semiconductor-electrolyte interface, without being subject to recombination, to facilitate the water splitting [17]. Recombination is a loss mechanism where holes and electrons recombine before being utilized in the water splitting [18]. Due to the involvement of multiple electron and proton steps,

some with high activation energies, this is a particularly problematic loss mechanism in the photoelectrolysis of water. Here, that means the electrons and holes recombine before reaching the interface. Ideally, the system should have a low recombination rate, which corresponds to a long carrier lifetime.

To better understand the water-splitting process for a single particle in a solution, a photoelectrochemical cell can be used [11, p. 290-291][19]. Such a cell is shown in Figure 2.4 for an n-type semiconductor anode connected to a metal cathode through an external circuit. In this case, it is assumed that the Fermi level of the semiconductor is initially higher than the Fermi level of the electrolyte, which results in the energy bands bending upwards. A bending like this leads to an accumulation of holes at the semiconductor-electrolyte interface, which makes the oxidation of the electrolyte possible. In a similar manner, electrons are depleted from the interface and travel toward the external circuit before reducing the electrolyte at the metal cathode. As illustrated in Figure 2.4, the following reactions occur:

$$\mathrm{O(soln)} + \mathrm{e^-(metal)} \longrightarrow \mathrm{R(soln)}$$

$$\mathrm{R(soln)} + \mathrm{h^+(semiconductor)} \longrightarrow \mathrm{O(soln)}$$

where O denotes the oxidized form of the electrolyte specimen and R denotes the reduced form of the electrolyte specimen.

The difference between the photoelectrochemical cell and a single particle in an electrolyte solution is that, for a single particle, the redox processes occur at open circuit potential (OCP) without a counter electrode [3]. Both redox reactions happen at the same particle, but at different sites, demonstrated in Figure 2.5. The reactions will happen simultaneously, meaning that the slowest one determines the overall reaction rate. Both the charge transfer and recombination rates of the charge carriers affect the efficiency of the reaction [17]. Thus, by reducing recombination rates one can increase the overall efficiency. Adding a co-catalyst to the particle may contribute to this, as it captures the photogenerated electrons before being subject to recombination [20]. This is illustrated in Figure 2.5.

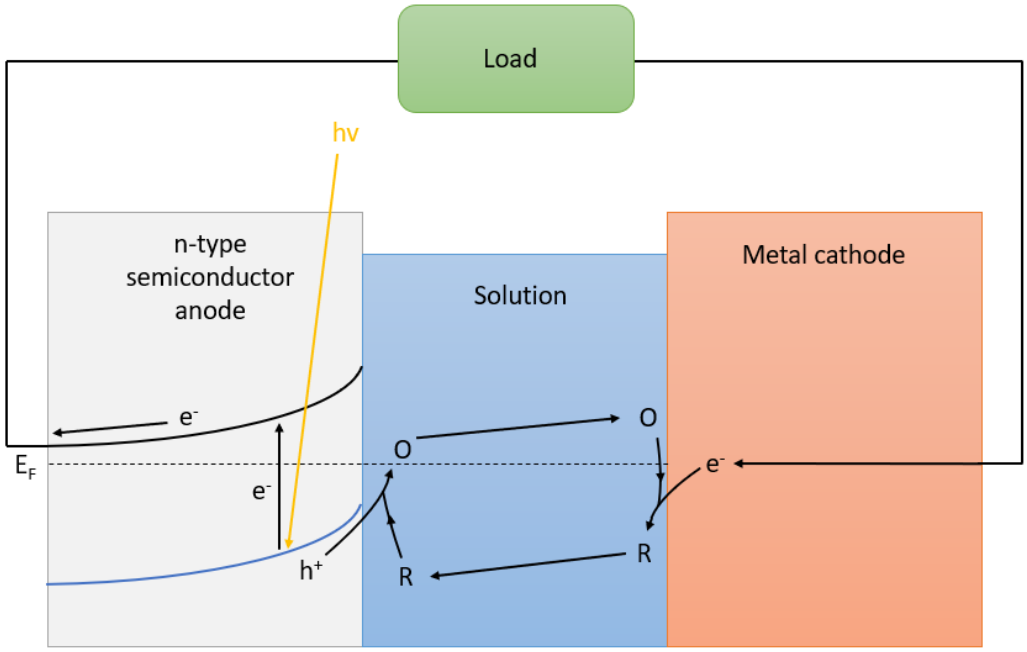

Figure 2.4: A galvanic photoelectrochemical cell for an n-type semiconductor where the Fermi level of the semiconductor is initially higher than the Fermi level of the solution, resulting in the energy bands bending upwards at equilibrium. The anode is the n-type semiconductor, which is coupled to a metal cathode through an external circuit. When the semiconductor is illuminated, holes will travel to the semiconductor-electrolyte interface and oxidize the reduced species, while the electrons will travel through the external circuit to the metal cathode to reduce the oxidized species [11, p. 291].

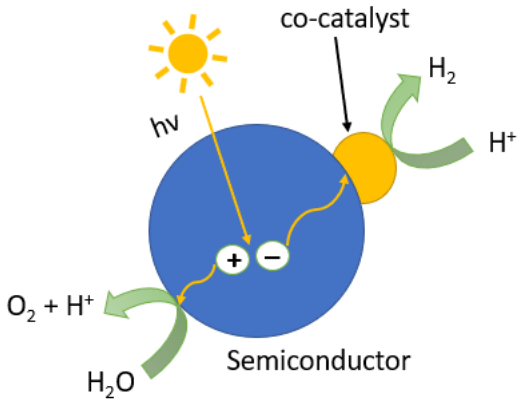

Figure 2.5: A deposited co-catalyst on a semiconductor particle that facilitate the hydrogen evolution reaction. Incoming light will generate electron-hole pairs that are subject to charge transfer and respective oxidation and reduction reactions. The generated electrons pass through the metal co-catalyst before entering the electrolyte. Illustration inspired by [20].

A metal co-catalyst such as platinum deposited on the semiconductor will provide a semiconductor-metal interface, resembling the photoelectrochemical cell in Figure 2.4. In this case, the electrons will not travel through an external circuit but pass through the metal co-catalyst before entering the electrolyte.

2.1.3 Doping of semiconductors

Manipulation of the band gap through doping is possible to obtain desired properties related to both the size and the positions of the band edges. Zhao et al. [6] and Wen et al. [7] both doped g-C_3N_4 with boron to achieve this, whilst other dopants such as nickel, potassium, and cobalt were used by Das et al. [21], Tripathi et al. [22], and Chen et al. [23]. Doped semiconductors have increased charge carrier density, either holes (p-type) or electrons (n-type), as energy levels in the forbidden band gap are introduced [10, p. 10]. This will in turn lead to a reduction of the band gap and thus a larger utilization of the available light. However, it is important to control the positions of the band edges to ensure that water splitting is still possible for the photocatalyst. The band edge positions can be controlled through the concentration of the dopant and monitored through experimental methods like the Mott Schottky analysis [6].

As mentioned before, the Fermi level of extrinsic semiconductors depends on the type and amount of doping. For an n-type semiconductor, the Fermi level will shift towards the CB with increasing dopant concentration. Similarly, the Fermi level shifts towards the VB for p-type semiconductors. In addition to affecting the Fermi level, doping can also influences the flat band potential [21]. This is discussed further in section 2.3.4.

2.1.4 Photocurrent response and band edge unpinning

When photons are incident on a semiconductor surface, a photocurrent is generated as electrons are excited from the VB to the CB [24, p. 198]. Thus, the photocurrent response can provide information about the photocatalytic efficiency of a semiconductor. It is the minority charge carriers in a semiconductor that are responsible for the rate-limiting redox reactions of water, and thus the overall reaction rate [3]. In an n-type semiconductor, these minority charge carriers are holes, and they will accumulate at or near the surface of a particle in a solution. Here, they are subject to recombination with the majority charge carriers; electrons. Using a test method such as chopped light voltammetry, the recombination rates at the particle's surface

can be investigated [18]. The observation of spikes and overshoots in this test method are often interpreted as evidence of recombination. Furthermore, chopped light voltammetry could be used to provide information about charge transfer and band edge unpinning. Band edge unpinning is a process that leads to reduced band bending as a result of an increased potential drop in the Helmholtz layer due to the build-up of charge carriers at the interface [25]. Such a decrease in band bending also leads to a decreased photocurrent. In short, band edge unpinning leads to the band edges moving to either more positive or negative potentials.

Experiments performed by Kelly et al. have reported that flat band potentials may shift upon illumination [25]. An n-type semiconductor shifts towards more anodic potential, and a p-type semiconductor shifts towards more cathodic potentials [10, p. 107-108]. This is due to an unpinning of bands, where the movement of the flat band potential must be interpreted by an equivalent movement of the band edges. For semiconductors in aqueous solutions, this may be due to the minority carriers being trapped in surface states, which is a process that competes with the transfer of minority carriers into the electrolyte. For an n-type semiconductor, this corresponds to holes being trapped in surface states. As the density of electrons is quite low for potentials more positive than the flat band potential, the recombination rate of these holes is also quite low. Thus, a considerable charge can be stored, which leads to a change in potential distribution and a downward shift of the energy bands on the vacuum scale. This shift in flat band potential occurs mostly at very low intensities of light, and at higher light intensities it saturates as all surface states become occupied.

By adding a suitable redox couple to the aqueous electrolyte, the accumulation of minority carriers and thus the resulting shift of band edges upon illumination can be avoided [10, p. 108]. For an n-type semiconductor, the addition of a hole acceptor, such as $Fe(CN)_6^{4-}$, could make the energy bands shift back to their original value. This is due to the minority carriers trapped in surface states being transferred to the hole acceptor in the electrolyte solution. A shift of flat band potential can also occur in the dark if minority carriers are injected into the semiconductor from a redox couple in the electrolyte solution.

Some layered semiconductors, such as WSe_2 and $MoSe_2$, show very low interaction with water as the metals are shielded from the solution [26][10, p. 109]. This leads to very large shifts of the flat band potential in aqueous electrolytes, as the minority carriers cannot be transferred across the semiconductor-electrolyte interface. Thus, the absence of a system in the electrolyte

solution that can accept the minority carriers can lead to band edge unpinning.

2.2 Degradation of organic dyes

An additional application of g-C_3N_4, besides photocatalytic water splitting, is the degradation of organic dyes [21]. By utilizing oxidation and reduction reactions, g-C_3N_4 can photocatalytically degrade such compounds [27]. Previous work performed on boron-doped g-C_3N_4 by Yan et al. has shown that a successful degradation of both methyl orange and rhodamine B, compounds found in waste waters, is possible [8].

Methyl orange (MO) is an organic compound, an anionic azo dye, that can be found in textiles [28]. It is also used as a pH indicator, meaning that its structure is changed at a certain pH. For MO, this pH-value is equal to 4.3 [29]. Rhodamine B (RhB) is also an organic compound, a water-soluble fluorescent xanthene dye, which is used to dye various substances [30]. As both of these compounds are toxic and because dyes, in general, are mutagenic and carcinogenic in nature, it is desirable to remove them from waste waters through degradation [21]. Schematic drawings of the chemical structure of MO and RhB are given in Figure 2.6.

The idea is that these dyes can be successfully degraded by g-C_3N_4 into less hazardous compounds by oxidation reactions. For this to be possible, the VB of g-C_3N_4 needs to be located at a more anodic potential than their respective oxidation potentials. This is so that holes from the VB can move to the semiconductor-electrolyte interface to oxidize the dyes [15]. However, should the VB be located at a potential more cathodic than the oxidation potentials of the dyes, these reactions will not be possible. The respective oxidation potentials can be located using experimental methods such as cyclic voltammetry. By varying the pH of the solution, a pH dependence of the oxidation potential can be established. If this pH dependence is different than that of the VB of g-C_3N_4, an optimum pH exists at which the photocatalytic degradation is the most efficient.

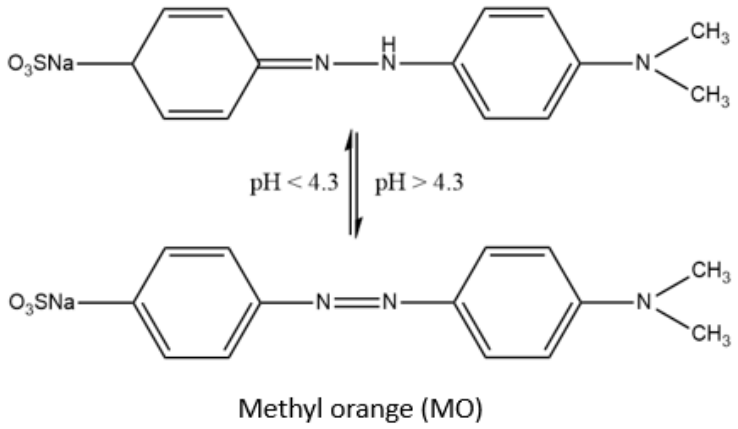

Methyl orange (MO)

(a)

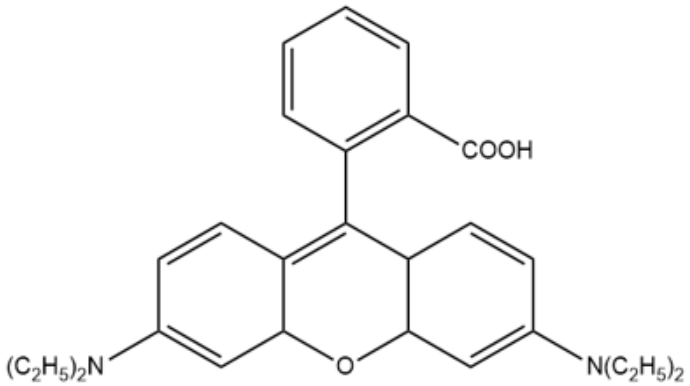

Rhodamine B (RhB)

(b)

Figure 2.6: Chemical structures of a) methyl orange [31] and b) rhodamine B [8].

If these dyes are to be used successfully as target reactions for the photocatalytic efficiency of g-C_3N_4, they cannot absorb light at the same wavelengths as g-C_3N_4. RhB has its light absorbance peak at about 550 nm due to its pink color, whilst MO will have light absorbance peaks located at about 510 nm for its acidic form (colored red) and closer to 470 nm for its neutral and basic form (colored orange to yellow) [32]. This can be determined more precisely using UV-visible spectroscopy. As the band gap of pristine g-C_3N_4 is about 2.7 eV, this corresponds to an absorption of light with wavelengths of 459 nm and lower. As this light absorption overlaps somewhat with MO, it is desirable to shift it towards higher wavelengths. This is obtained by reducing the band gap through doping. Boron-doped g-C_3N_4 synthesized at 400°C gives a band gap of about 2.0 eV, which corresponds to an absorption of light with wavelengths equal to 620 nm and lower [6]. This is enough to avoid overlapping absorbance with both RhB

and MO.

If the absorbance peaks of MO and RhB is to be used as a basis for the amount of oxidized dye, a calibration curve is needed. By performing UV-visible spectroscopy of the dyes at different concentrations, this can be obtained. The absorption peaks can then be plotted as a function of concentration, which is explained in more detail in section 2.3.6. This would give the real amount of oxidized dye, whilst utilization of Faraday's law could give the theoretical amount of oxidized dye [33],

$$m = \frac{ItM}{zF} \tag{2.3}$$

Here, m is the dye's mass, I is the current, t is the time, M is the dye's molar mass, z is the number of transferred electrons and F is Faraday's constant. This equation gives the theoretically expected mass of dye after illumination based on the time of illumination and the obtained current. Thus, one can determine how much of the real current is used to oxidize the dyes by comparing the results with those from the UV-visible spectroscopy.

2.3 Methods

2.3.1 X-Ray Diffraction

X-ray diffraction (XRD) is a characterization method for crystalline materials used to determine crystal structures [9, p. 114-117]. It utilizes a beam of X-rays that are incident on a sample and then diffracted by the crystalline phases of the sample. The result of the measurement is a diffraction pattern that is considered a fingerprint of the sample, which gives intensities as a function of the diffraction angle, θ. The diffractogram can be used to find lattice constants and geometries by applying Bragg's law,

$$\lambda = \frac{2d_{\mathrm{hkl}}}{\sin\theta} \tag{2.4}$$

If peaks are shifted towards lower angles in a diffractogram, this indicates decreased lattice spacing as this corresponds to a lower $\mathrm{d_{hkl}}$ in equation 2.4. Similarly, a shift in the peaks towards higher angles indicates an increased lattice spacing.

2.3.2 Fourier Transform Infrared Spectroscopy

Fourier Transform Infrared Spectroscopy (FTIR) is another characterization technique that provides spectra functioning as fingerprints for different chemical bonds and atoms [34, p. 347-

348]. In between atoms, the chemical bonds vibrate with frequencies determined by the bond strengths and the mass of the atoms. These frequencies are located in the infrared region of the electromagnetic spectrum and they are specific to the group of atoms and type of bond involved in the vibration. The infrared spectrum, resulting from a measurement of the relative intensity vs. the frequency, can be subject to a Fourier transform. This results in an intensity vs. frequency spectrum.

2.3.3 Diffuse Reflectance Spectroscopy and Tauc plots

To determine the band gap of semiconductors, diffuse reflectance spectroscopy (DRS) is a method frequently used [6][7][21][22][23]. By utilizing the Kubelka-Munch relation provided in equation 2.5, one can transform the measured diffuse reflectance to the equivalent absorption coefficient at different wavelengths [35].

$$\alpha = F(R) = \frac{(1-R^2)}{2R} \tag{2.5}$$

Here, α denotes the absorption coefficient, $F(R)$ denotes the Kubelka-Munch relation and R denotes the measured reflectance. This can be used to find the band gap of a semiconductor by usage of Tauc plots, where the Tauc relation

$$(\alpha h\nu) = A(h\nu - E_{\mathrm{g}})^{\mathrm{n}}, \tag{2.6}$$

provides the basis for these plots. In this relation, n provides information about the type of band gap the semiconductor possesses, where an indirect band gap corresponds to n = 1/2 and a direct band gap corresponds to n = 2. Furthermore, hν corresponds to the energy of the incoming light, obtained by 1240 divided by the respective wavelength. Thus, by plotting $(\alpha h\nu)^n$ vs. $h\nu$, one can extrapolate the linear part of the curve to obtain the value of the band gap as the intersection of the hν axis.

2.3.4 Mott Schottky analysis

For an n-type semiconductor, the measured flat band potential E_{fb} is assumed to correspond with the CB edge potential, whilst, for a p-type semiconductor, it is assumed to correspond with the VB edge potential [21]. To measure the flat band potential, Mott Schottky analysis can be utilized. The Mott Schottky equation is obtained by solving Poisson's equation and is given by

$$\frac{1}{C_{\mathrm{s}}^2} = \frac{2}{\varepsilon\varepsilon_0 A^2 e N_{\mathrm{D}}}\left(E - E_{\mathrm{fb}} - \frac{k_{\mathrm{B}}T}{e}\right) \tag{2.7}$$

Here, C_s denotes the capacitance of the semiconductor at the interface, ε denotes the solution's permittivity, ε_0 denotes the permittivity of vacuum, A denotes the interfacial area, e denotes the electronic charge, N_D denotes the carrier donor density, E and E_{fb} denotes the potential and the flat band potential, respectively, k_B denotes Boltzmann's constant and T denotes the temperature. By plotting $1/C_s^2$ vs. V, one can extrapolate the linear part of the curve to obtain the value of the CB or the VB, depending on the type of semiconductor [36]. If the slope is positive, the obtained value of the flat band potential is assumed to correspond with the CB, and the semiconductor displays an n-type behavior [21]. Similarly, a negative slope will result in the flat band potential corresponding to the VB, as the semiconductor displays a p-type behavior.

After obtaining the value of the flat band potential from a Mott Schottky plot, the respective value of the other band edge can be found by adding or subtracting the value of the band gap [21]. As explained in section 2.3.3, the band gap can be found by i.e., DRS.

The slope of a Mott Schottky plot is inversely proportional to the density of donors at the interface. Thus, both dopants and pH may affect the slope [21]. For pristine g-C_3N_4, lone pairs of nitrogen are the primary donors. Additions of dopants may reduce the number of these donors as they can be subject to electronic interaction with the dopant atoms due to nitrogen's excess electrons. This would result in an increased slope in the Mott Schottky plots compared to intrinsic semiconductors. Furthermore, the adsorption of protons and hydroxide ions may also affect the number of these available donors. In particular, protons may bind to the electron-rich nitrogen atoms at the surface, thus decreasing the number of donors and increasing the slope in the Mott Schottky plot. Semiconductors with a higher number of available donors will have an enhanced electric conductivity of the charge carriers, which in turn could lead to a higher photoresponse [37].

2.3.5 Sonochemical synthesis

To produce metal nanoparticles from respective metal salts, a sonochemical synthesis can be utilized [38][39]. This method uses high-power ultrasound to facilitate reduction reactions of metals such as platinum. A transducer that converts electrical energy to sound energy provides this ultrasound, which further creates cavitation bubbles. These cavitation bubbles generate environments of high temperature and pressure upon collapsing, which may cause water to split into hydrogen (H·) and hydroxyl (OH·) radicals. These are known as primary radicals,

and they possess a short lifespan. Secondary radicals with a longer lifespan can be created by adding a radical scavenger such as ethanol to the solution. The creation of these secondary radicals is obtained by ethanol scavenging the primary radicals at the bubble-solution interface. After being created, the secondary radicals can diffuse into the bulk solution and reduce metal salts into metal nanoparticles.

2.3.6 UV-visible spectroscopy

UV-visible spectroscopy is used to analyze electronic transitions in the ultraviolet and the visible range of light [40, p. 196]. In this method, a cuvette containing the target solution is exposed to light in the UV and visible region, providing spectra of measured absorbance as a function of the wavelength of light. These spectra can be considered fingerprints of the different specimens. By utilizing this, one can determine which specimens are present in a solution, i.e., the different oxidation states of a metal. Thus, one can confirm that platinum ions have been reduced to metallic nanoparticles when utilizing the sonochemical synthesis described in section 2.3.5.

UV-visible spectroscopy can also be used to provide concentrations of organic dyes before and after exposure to illumination of the g-C_3N_4 photocatalyst. To obtain this, one must perform a calibration of light absorption values at different concentrations. The result is a linear plot of absorption values as a function of concentration, where the slope corresponds to ε in Beer-Lambert's law [41],

$$A = \varepsilon \cdot c \cdot l \tag{2.8}$$

Here, A is the measured absorption, c is the respective concentration of the dye and l is the length of the cuvette. By comparing the concentration of organic dye obtained from the measured absorption before and after photocatalytic degradation, the photocatalytic efficiency of g-C_3N_4 can thus be estimated.

2.3.7 Scanning (Transmission) Electron Microscopy

Scanning (transmission) electron microscopy (S(T)EM) is a characterization method for nanomaterials and nanostructures, where information about the surface structure and chemical composition is obtained by an electron microscope [34, p. 336-339]. An electron beam is incident on a sample surface when using SEM, where the collected emitted electrons provide images

of the surface. By studying these images, one can obtain information about microstructures, chemical distribution, and morphology. For thin samples, TEM can be used in addition to SEM, where the electrons either deflect or penetrate the material. Images obtained from these electrons provide chemical analyses and structural characterization. Here, heavier elements can easily be distinguished from lighter elements by utilizing the difference in penetration depth of electrons through varying elements. By using energy-dispersive X-ray spectroscopy (EDS), these varying elements can be identified due to the sensitivity of electron scattering to target elements.

2.3.8 Linear sweep and cyclic voltammetry

A three-electrode setup consisting of a working electrode (WE), a counter electrode (CE), and a reference electrode (RE) is usually used for current-potential measurements at semiconductor electrodes [10, p. 61-62]. A potentiostat is used to supply an external voltage to the cell.

A rotating disk electrode (RDE) is often used as the WE in electrochemical measurements [11, p. 162-164]. The RDE consists of a disk insulator embedded with a disk of an electronic conductor such as glassy carbon or platinum. By utilizing rotation at high velocities, it employs forced convection and thus ensures a steady mass transport of the bulk solution to the RDE. At the electrode surface, only diffusion is operative as the convective velocity is zero.

Linear sweep voltammetry (LSV) is an electrochemical technique that, according to equation 2.9, applies a potential that either decreases or increases with time [11, p. 346]. To avoid initially occurring reactions, the initial potential E_0 is set to start before the onset of the chemical reaction. Furthermore, the sweep rate is termed v, and given in Vs^{-1}.

$$E(t) = E_0 + vt \tag{2.9}$$

Nernst equation can be used to obtain the current response due to potential sweep for a simple redox reaction with only one electron transferred:

$$E = E^{0'} - \frac{RT}{nF} \ln\left(\frac{[\text{Reduced species}]}{[\text{Oxidized species}]}\right) \tag{2.10}$$

Where $E^{0'}$ denotes the formal potential, R denotes the gas constant, T denotes the temperature, n denotes the reaction's number of transferred electrons, F denotes Faraday's constant and

the brackets denote concentrations. One can further develop expressions for the current as a function of the potential and sweep rate by considering the potential's time dependence as given in equation 2.9. A surface-controlled reaction displays a current proportional to the sweep rate, whilst a diffusion-controlled reaction displays a current proportional to $\sqrt{v}$. The current vs. potential plot that results from the measurement is known as a voltammogram. An example of a voltammogram is given in Figure 2.7 for the LSV of platinum towards the HER.

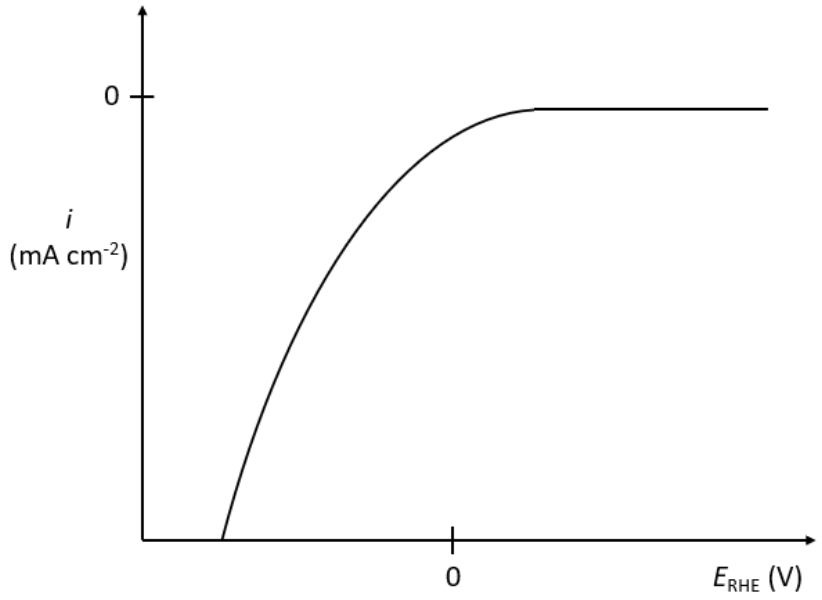

Figure 2.7: An example of a voltammogram where a linear sweep voltammetry of platinum towards the hydrogen evolution reaction (0 V_{RHE}) is displayed. Illustration inspired by [42].

LSV of a redox couple, such as $Fe(CN)_6^{3-/4-}$, can be used to investigate the placement of a semiconductor's VB and CB edges, as stated by Lervik et al. [13], by utilizing faradaic currents. For investigations of an n-type semiconductor such as g-C_3N_4, the obtained anodic and cathodic currents in an electrolyte containing such a redox couple can give information about the relative position of the VB compared to the redox potential of the $Fe(CN)_6^{3-/4-}$ couple [43]. If both anodic and cathodic faradaic currents are present in equal magnitude, the VB is located at approximately the same potential as the redox potential of $Fe(CN)_6^{3-/4-}$, which is demonstrated in scenario a) in Figure 2.8. However, if the cathodic current is a capacitive one, the value is closer to zero at potentials more cathodic than the redox potential of the $Fe(CN)_6^{3-/4-}$ couple. For potentials more anodic than the redox potential of $Fe(CN)_6^{3-/4-}$, the anodic current may still be faradaic and present in a higher magnitude than that of the cathodic current. If so, the VB of the semiconductor is located at a potential that only overlaps with the reduced form of

the $Fe(CN)_6^{3-/4-}$ redox couple, resulting in a more anodic VB than the redox potential of the $Fe(CN)_6^{3-/4-}$ couple. This is demonstrated for scenario b) in Figure 2.8. Likewise, if the only faradaic current is the cathodic one, this indicates that the VB of the semiconductor is located at a potential that only overlaps with the oxidized form of $Fe(CN)_6^{3-/4-}$, resulting in a more cathodic VB than the redox potential of the $Fe(CN)_6^{3-/4-}$ couple.

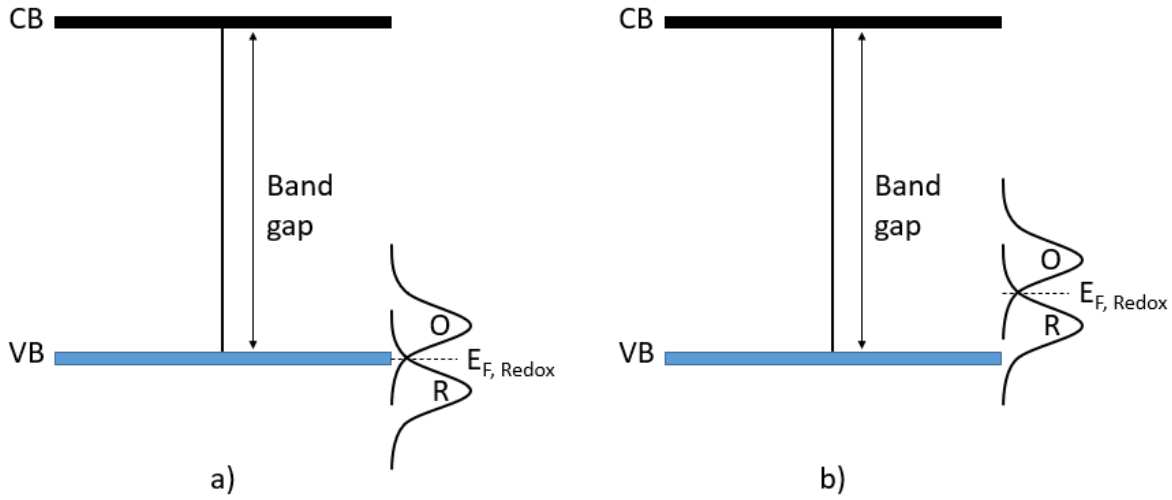

Figure 2.8: An example of how the potential of the valence band of a semiconductor can be determined relative to that of the redox potential of the $Fe(CN)_6^{3-/4-}$ couple, denoted $E_{\text{F, Redox}}$ in the figure, using linear sweep voltammetry. In the figure, *O* denotes the oxidized form of the $Fe(CN)_6^{3-/4-}$ redox couple and *R* denotes the reduced form of the $Fe(CN)_6^{3-/4-}$ redox couple. Illustration inspired by [13] and [43].

Cyclic voltammetry (CV) is obtained by reversing the scanning direction from LSV [40, p. 77-78]. This technique can be used to characterize electrochemical processes and reactions that occur at the electrode-electrolyte interface. Here, a constant scan rate is used to sweep the electrode potential between two limits. These two limits are usually chosen to be the onset of hydrogen evolution and oxygen evolution for platinum.

Electrode processes such as oxidation and reduction, metal dissolution, and adsorption and desorption of species in the electrolyte can be obtained by the resulting voltammogram [40, p. 78]. Furthermore, one can also obtain the kinetics of electron transfer, positions of HOMOs and LUMOs, and thermodynamics of redox systems from CV.

2.3.9 Photoelectrochemical measurements

A light source, a potentiostat, and a three-electrode setup in a photoelectrochemical cell are used when performing photoelectrochemical measurements. The photoanode, which is used as the WE, is submerged in an electrolyte and, through an optically transparent window in the cell, is exposed to the incoming light.

The efficiency at which incoming light is converted into charge carriers is known as quantum efficiency, which is one of the key parameters for photoelectrodes [44]. This is usually measured as a function of the incident light and plotted using a method known as incident photon to current efficiency (IPCE). Here, the ratio of the generated charge carriers to the number of incident photons makes up the IPCE. Thus, the IPCE and the quantum efficiency equals 100% if all incoming photons generate one electron-hole pair each. However, this is an ideal case. For real systems, the IPCE and quantum efficiency is lower.

The lowered efficiency for real systems is due to loss mechanisms such as recombination and reflection of the incoming light [44]. These mechanisms prevent the quantum efficiency and the IPCE from reaching 100%. Additionally, semiconductors can only utilize incoming photons with energies larger than the band gap to create charge carriers. Thus, for photons with energies lower than the band gap, the IPCE and quantum efficiency will be equal to zero.

3 Experimental

3.1 Chemicals

In this experiment, the following chemicals were used: dicyandiamide ($C_2H_4N_4$) (Sigma-Aldrich, 99%), ethanol (EtOH) (VWR chemicals, GPR Rectapur, 96%), methyl orange (MO) (Sigma-Aldrich, indicator ACS, Reag. Ph Eur), Nafion^{TM} 117 containing solution (Sigma-Aldrich, 5% in a mixture of lower aliphatic alcohols and water), platinum(IV) tetrachloride ($PtCl_4$) (Sigma-Aldrich, 96%), potassium ferricyanide ($K_3[Fe(CN)_6]$) (Sigma-Aldrich, for analysis EMSURE® ACS, Reag. Ph Eur), potassium ferrocyanide ($K_4[Fe(CN)_6]$) (Sigma-Aldrich, for analysis EMSURE® ACS, ISO, Reag. Ph Eur), potassium hydroxide (KOH) (Sigma-Aldrich, ACS reagent, $\geq$ 85%), potassium iodide (KI) (Sigma-Aldrich, ACS reagent, $\geq$ 99.0%), 2-propanol (IPA) (VWR chemicals, technical, $\geq$ 98%), rhodamine B (RhB) (Sigma-Aldrich, $\geq$ 95% (HPLC)), sodium borohydride ($NaBH_4$) (Sigma-Aldrich, powder, $\geq$ 98.0%), sodium sulfate (Na_2SO_4) (Merck Millipore, anhydrous for analysis) and sulfuric acid (H_2SO_4) (Sigma-Aldrich, for analysis EMSURE® ISO, 95-97%). Throughout the experiment, deionized water (DI water) (Milli-Q, $18.2\,M\Omega \cdot cm$) was also used.

3.2 Synthesis of graphitic carbon nitride

Based on earlier experiments, graphitic carbon nitride was synthesized using dicyandiamide in a one-step heating process [16]. An amount of 3.0 g dicyandiamide was distributed in an alumina crucible and inserted into a horizontal tube furnace (Carbolite CTF 12/65/550). Using a heating rate of $10^{\circ}C\,min^{-1}$, the precursor was heated up to 550°C and maintained at this temperature for 4 hours before cooling down to room temperature. Throughout the process, a continuous flow of synthetic air was present. The resulting bulk g-C_3N_4 was milled into a fine powder using a mortar and pestle.

3.3 Exfoliation of graphitic carbon nitride

A one-step heating process was used to exfoliate the bulk g-C_3N_4 after a washing procedure. Washing of the powder prior to exfoliation was conducted to remove unwanted impurities. Bulk g-C_3N_4 was transferred to a centrifuge tube, and added a 50/50 mixture of EtOH and DI water. The mixture was centrifuged (Eppendorf 5810 R) for 15 minutes at 12 000 rpm, and the liquid

was discarded. This procedure was conducted a total of three times.

Washed bulk g-C_3N_4 was distributed in an alumina crucible and inserted into a horizontal tube furnace (Carbolite CTF 12/65/550) for exfoliation of the g-C_3N_4 layers. The powder was heated up to 500°C with a heating rate of $5°C\,min^{-1}$ and maintained at this temperature for 4 hours. The atmosphere used was synthetic air, and a steady flow was present throughout the process. The resulting exfoliated g-C_3N_4 was ground to a fine powder by employing a mortar and pestle.

3.4 Doping of boron on graphitic carbon nitride

Bulk g-C_3N_4 and $NaBH_4$ in a ratio of 4:3 were milled together in a mortar for 30 minutes before being distributed in an alumina crucible and inserted into a horizontal tube furnace (Carbolite CTF 12/65/550), following the method of [6]. This has been shown to introduce boron-dopants in the g-C_3N_4. The powders were heated up to 300°C and 500°C at a heating rate equal to $10°C\,min^{-1}$. Due to nitrogen gas not favoring nitrogen leaving the lattice, the atmospheres for the doping process were argon and synthetic air. The temperatures were maintained for 1 hour before the doped powders were cooled down to room temperature. Lastly, the powders were washed with a 50/50 mixture of EtOH and DI water and centrifuged (Eppendorf 5810 R) a total of three times before being dried in a vacuum oven (Binder VD 23) at 60°C overnight. The doped powders were named B300Air, B500Air and B500Argon, where the B denotes boron-doped g-C_3N_4, 300 and 500 denotes the temperature in the doping synthesis, and Air and Argon denotes the atmosphere used.

3.5 Deposition of platinum

A sonochemical synthesis route was utilized to deposit 20 wt% of platinum nanoparticles on pristine and boron-doped g-C_3N_4. Ultrasound with a frequency of 346 kHz and an acoustic power of 42.5 W was used. $PtCl_4$ were thoroughly mixed with 0.5 M EtOH in a 200 mL solution for the precursor liquid. The g-C_3N_4 powder was mixed with 10 mL of DI water in a separate container.

The platinum-containing solution was then transferred to the experimental setup as given in [39], and followed the same sonication procedure. Concentration changes in the oxidation

states of the platinum precursor were verified using a UV-visible spectrophotometer (Thermo Scientific Evolution 220) and the Thermo INSIGHT software. Here, a scan speed of 100 $\mathrm{nm\,min^{-1}}$ and a bandwidth of 1 nm were used to analyze the samples for light with wavelengths ranging from 800 nm to 200 nm. The platinum-containing solution was mixed with KI, forming PtI_6^{2-} and PtI_4^{2-}. The resulting absorption peaks located at 495 nm and 345 nm were used to assess the development of the reduction reaction. After 100 minutes of sonication, the g-C_3N_4 powder was added to the solution and further sonicated for 25 minutes.

The resulting substrate with platinum nanoparticles was centrifuged (Eppendorf 5810 R) to separate the powder from the solution at 12 000 rpm for 15 minutes. The powder was also washed with a 50/50 mixture of DI water and EtOH three times.

3.6 Methods of characterisation

3.6.1 X-Ray Diffraction

A D8 DaVinci Diffractometer with Cu Kα was used to perform XRD, and a 10 mm Si-cavity sample holder was used for the powders. Samples containing boron were covered with a Kapton film. The diffractometer probed from 10° to 80° for 60 minutes, with a step length of 0.010° and a variable divergence slit (V6).

3.6.2 Fourier Transform Infrared Spectroscopy

A vacuum spectrometer (Bruker Vertex 80v) was used to perform FTIR on pristine and boron-doped g-C_3N_4. The samples were scanned from 4000 $\mathrm{cm^{-1}}$ to 550 $\mathrm{cm^{-1}}$ using the attenuated total reflection (ATR) mode. The resolution was equal to 4 $\mathrm{cm^{-1}}$ and the scan time was equal to 100 scans.

3.6.3 Diffuse Reflectance Spectroscopy

Diffuse reflectance spectroscopy of pristine and boron-doped g-C_3N_4 was performed using an integrating sphere (AvaSphere-50) and a monochromator (Newport 74125). Using the reflectance mode, the samples were scanned from 350 nm to 1000 nm. To obtain the respective band gaps, the resulting spectra were transformed to Tauc plots using equations 2.5 and 2.6.

3.6.4 Scanning (Transmission) Electron Microscopy

A Hitachi High-Tech SU9000 was used to investigate the platinum nanoparticles deposited on the g-C_3N_4 substrate. A small amount of g-C_3N_4 powders deposited with platinum nanoparticles were added to a 50/50 mixture of 2-propanol and DI water. 5 µL of this solution was drop cast on a Formvar/Carbon supported copper grid with a size of 300 mesh and dried for a couple of hours. Both Secondary Electron (SE) and Bright Field (BF) modes were used to capture images, and the acceleration voltage and emission current were equal to 30 kV and 10 µA, respectively. EDS was performed to confirm the presence of platinum.

3.6.5 Mott Schottky analysis

A three-electrode setup and a potentiostat (Ivium-n-Stat) were used to obtain Mott Schottky plots at different pH. The working electrode was a glassy carbon RDE deposited with catalyst ink, the counter electrode was graphite and the reference electrode was Hg/HgO for alkaline electrolytes. In neutral or acidic electrolytes, a saturated Ag/AgCl electrode was used.

The ink used in the measurements was prepared by mixing 10 mg g-C_3N_4 without deposited platinum with 475 µL of DI water, 475 µL of 2-propanol, and 50 µL of Nafion. Using an electromagnetic stirrer, the solution was mixed for 10 minutes before being sonicated in an ultrasonic bath (VWR USC300TH) for 30 minutes.

A total of 10 µL of the as-prepared ink was spin cast onto the RDE with a rotation speed of 100 rpm and further dried at a rotation speed of 200 rpm for 20 minutes. The electrolyte solution, consisting of various mixtures of 0.5 M H_2SO_4 and 0.1 M KOH, was purged with Ar(g) (5.0) for a minimum of 20 minutes to remove dissolved oxygen.

For the Mott Schottky plots, potential measurements ranged from -2.5 V_{RHE} to -0.1 V_{RHE} with a potential step equal to 10 mV for 1 kHz, 1.7 kHz, and 3 kHz. In the Ivium software, the Mott Schottky analysis was utilized.

3.6.6 Characterisation of methyl orange and rhodamine B

To obtain oxidation peaks, CV of MO and RhB were performed with a concentration of 0.31 mM and 0.21 mM, respectively, in 0.1 M Na_2SO_4. The pH of the solution was varied by adding H_2SO_4 and KOH to the solution. These measurements were obtained using a three-electrode

setup where glassy carbon was the WE, graphite was the CE and the saturated Ag/AgCl electrode was used as a reference for acidic and neutral solutions. The Hg/HgO electrode was used as a reference for alkaline solutions. The potential limits for RhB were 0.5 V_{RHE} to 1.6 V_{RHE}, whilst for MO the limits were 1.05 V_{RHE} to 1.6 V_{RHE}. The lower limit for MO was chosen to be this high due to the polymerization of MO at potentials lower than 0.95 V_{RHE}, which would have covered the WE [45]. Scan rates of 500 mVs^{-1} were chosen to obtain clearly visible peaks.

MO and RhB in neutral pH were subject to UV-visible spectroscopy (Thermo Scientific Evolution 220) to obtain absorption peaks at different concentrations. The curves were measured from 800 nm to 200 nm with a bandwidth of 1 nm. For MO, the starting concentration was 0.050 mM and the lowest concentration was 0.00208 mM. For RhB, the starting concentration was 0.0125 mM and the lowest concentration was 0.00208 mM. The absorbance values were too high at higher concentrations than 0.050 mM and 0.0125 mM, respectively.

3.6.7 Electrochemical measurements of the $Fe(CN)_6^{3-/4-}$ redox couple

The $Fe(CN)_6^{3-/4-}$ redox couple was used to confirm the placements of the band edges obtained from the Mott Schottky analysis. Here, CV was performed from 0 V_{RHE} to 1.5 V_{RHE} to obtain oxidation potentials at a pH of 2.2 and 4.4. The WE was a platinum RDE, the CE was graphite and the RE was saturated Ag/AgCl. After obtaining the oxidation potential, LSV was performed from 0.98 V_{RHE} to 0.24 V_{RHE} for a pH of 2.2 and from 1.1 V_{RHE} to 0.38 V_{RHE} for a pH of 4.4, centered around where the current was zero. The scan rate was equal to -5 mVs^{-1}. For the LSV, the WE was replaced with a glassy carbon RDE covered with the catalyst ink as described in section 3.6.5. The respective currents were used to determine the placement of the VB relative to the redox potential of the $Fe(CN)_6^{3-/4-}$ couple.

3.6.8 Photoelectrochemical measurements

To measure the photocatalytic efficiency based on the degradation of MO, both pristine and boron-doped g-C_3N_4 were subject to IPCE using a photoelectrochemical cell (Zahner). The electrolytes used were prepared from a 0.025 mM MO solution in 0.5 M H_2SO_4 with a pH of 0.3, using KOH to obtain solutions at different pH values. The pH values for the other solutions were 1.0, 2.1, 4.4, and 12.2. The respective concentrations of MO were 0.0167 mM,

0.00833 mM, 0.0075 mM, and 0.0125 mM. Platinum was used as the CE and Ag/AgCl in 3M KCl as the RE. The WE was prepared by drop casting the photocatalyst ink, prepared as for the electrochemical methods, onto carbon paper. 200 µL of the ink was drop cast a total of four times, corresponding to a total amount of 800 µL to achieve a dense layer of catalyst. The samples were illuminated with light at discrete wavelengths from 290 nm to 800 nm with a frequency of 1 Hz. A constant white background light was also applied. Based on the results from UV-visible spectroscopy before and after IPCE, the amount of oxidized MO was calculated.

3.6.9 Degradation of dye

The degradation of MO with time was investigated using a UV-visible spectrophotometer (Thermo Scientific Evolution 220), an integrating sphere (AvaSphere-50), and a monochromator (Newport 74125). 1 mg of the photocatalyst powder was mixed with a 50 mL solution containing a mixture of 0.5 M H_2SO_4 and 0.5 M KOH with pH values of 2.2 and 4.4, respectively. The solutions were mixed in an ultrasonic bath (VWR USC300TH) for 10 minutes before adding 2 mg of MO. Further mixing using an electromagnetic stirrer was performed for 15 minutes in the dark. The resulting solutions were illuminated with white light using an integrating sphere, and 3 mL samples were taken every 15 minutes for a total of 60 minutes. These samples, including one prior to illumination, were subject to UV-visible spectroscopy to monitor the amount of degraded MO as a reduction in absorption peak. The curves were measured from 800 nm to 200 nm with a bandwidth of 1 nm.

4 Results

4.1 X-Ray Diffraction

Results from the XRD analysis are given in Figures 4.1 and 4.2 for exfoliation and doping, respectively, and they both indicate successful processes. For the exfoliation, the main peak located at $2\theta = 27.4°$ has shifted +0.15° after the process. This implies a successful exfoliation, as a shift towards higher 2θ values indicates an increased lattice spacing following equation 2.4. The main peak located at $2\theta = 27.4°$ corresponds to the (002) plane, which is the interlayer stacking peak of aromatic systems. A second peak is located at $2\theta = 13°$, corresponding to the (100) plane, which corresponds to the interlayer structural packing. Both of these peaks are reported in literature [46].

For the doped samples, a decrease in intensity for the peaks situated at the same 2θ values are observed. An additional broadening of the peak located at $2\theta = 27.4°$ occurs for all the doped samples. It is also clear that the doping synthesis at 500°C made the samples more crystalline, as can be seen from the many sharp peaks for B500Air and B500Argon.

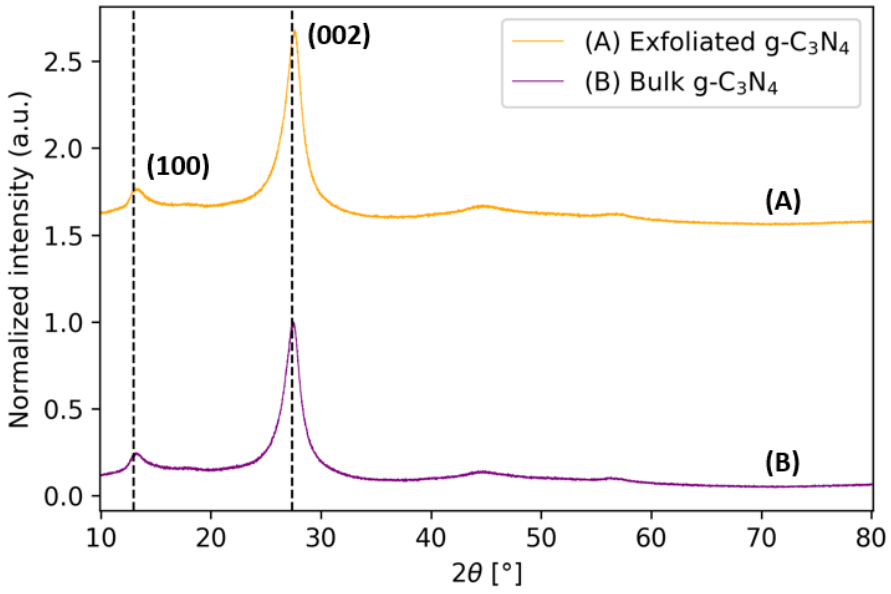

Figure 4.1: X-ray diffractograms of exfoliated (A) and bulk (B) g-C_3N_4 for 2θ values ranging from 10-80°. The two vertical lines correspond to $2\theta = 13°$ and 27.4°, the (100) and (002) planes associated with g-C_3N_4, respectively.

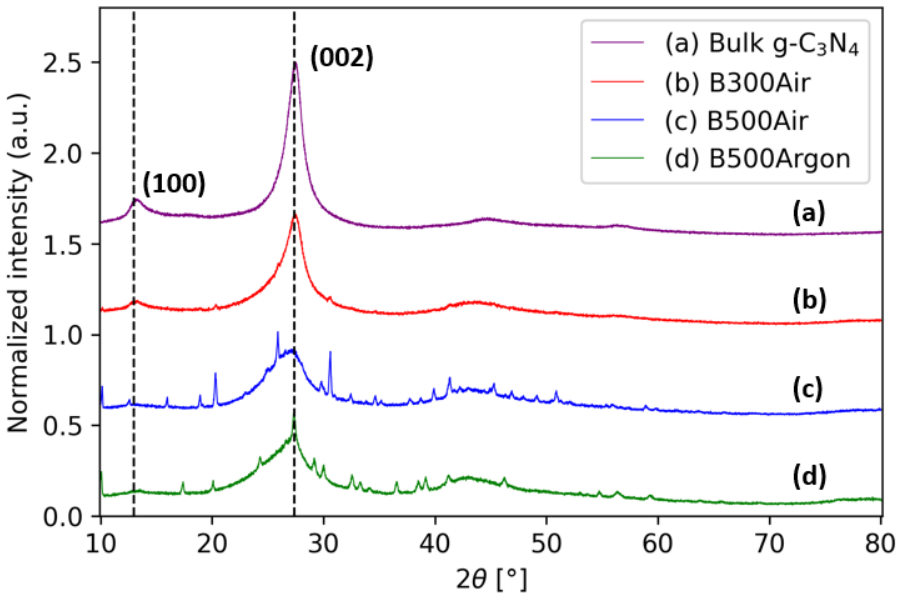

Figure 4.2: X-ray diffractograms of bulk g-C_3N_4 (a), B300Air (b), B500Air (c) and B500Argon (d) for 2θ values ranging from 10-80°. In these sample names, B denotes boron-doped, 300 and 500 denote the synthesis temperature, and Air and Argon denote the atmosphere used in the doping synthesis. The two vertical lines correspond to 2θ = 13° and 27.4°, the (100) and (002) planes associated with g-C_3N_4, respectively.

4.2 Fourier Transform Infrared Spectroscopy

The spectroscopic results obtained from FTIR are given in Figure 4.3. The main peaks are located at 810 cm^{-1}, 900-1800 cm^{-1}, 2180 cm^{-1} and 3000-3500 cm^{-1}, and they are the only peaks present for both pristine and boron-doped g-C_3N_4. The peak situated at 2180 cm^{-1} corresponds to the asymmetric stretching vibration of N≡C- groups, which is formed during the doping [6]. This peak is visible for the boron-doped samples, but not for pristine g-C_3N_4. Furthermore, the peaks situated at 810 cm^{-1} correspond to the out-of-plane bending of heptazine rings, which makes up the g-C_3N_4 structure [6]. Lastly, the peaks situated between 900-1800 cm^{-1} correspond to -C-N- stretching, and the peaks situated between 3000-3500 cm^{-1} correspond to -N-H stretching vibrations.

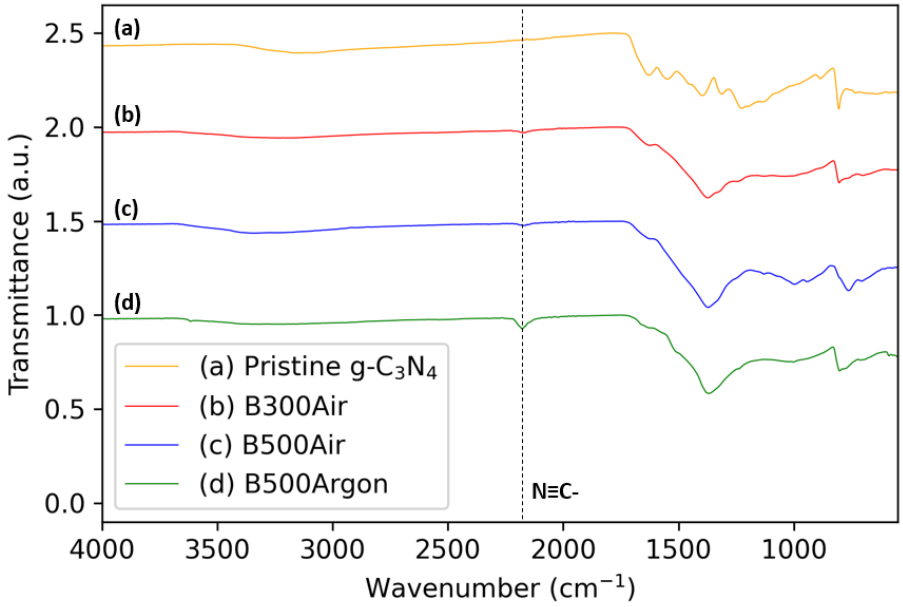

Figure 4.3: Fourier transform infrared spectra of pristine g-C_3N_4 (a), B300Air (b), B500Air (c) and B500Argon (d). In these sample names, B denotes boron-doped, 300 and 500 denote the synthesis temperature, and Air and Argon denote the atmosphere used in the doping synthesis. The vertical line located at 2180 cm^{-1} corresponds to the N≡C- peak, which is a bond that forms during doping.

4.3 Determination of the band gap

The DRS results, given in Figure 4.4, show a decreased reflectance of light with increased boron content in the lattice. The respective Tauc plots are given in Figure 4.5, in which the band gap is reduced with increased boron content in the lattice. Pristine g-C_3N_4, B300Air, B500Air, and B500Argon display band gaps of 3.10 eV, 2.38 eV, 1.73 eV, and 1.59 eV, respectively.

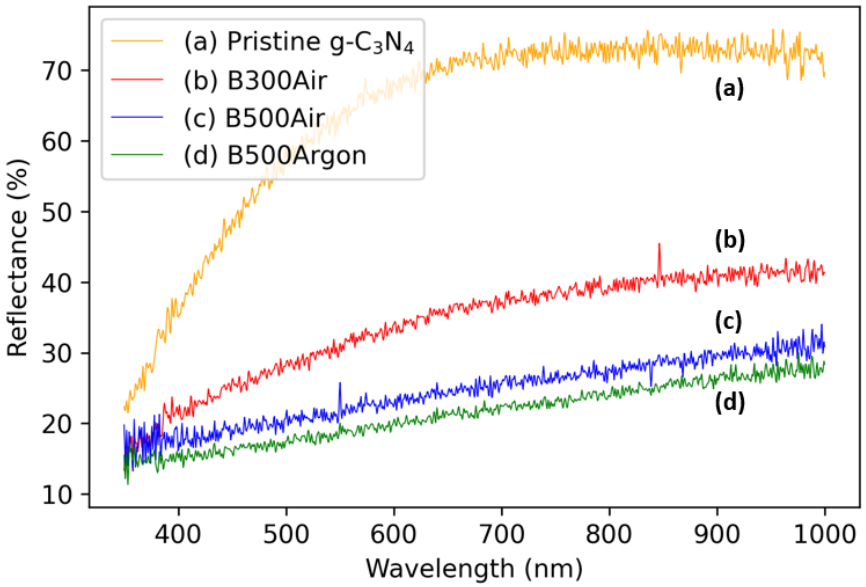

Figure 4.4: Obtained diffuse reflectance spectra of pristine g-C_3N_4 (a), B300Air (b), B500Air (c) and B500Argon (d). In these sample names, B denotes boron-doped, 300 and 500 denote the synthesis temperature, and Air and Argon denote the atmosphere used in the doping synthesis.

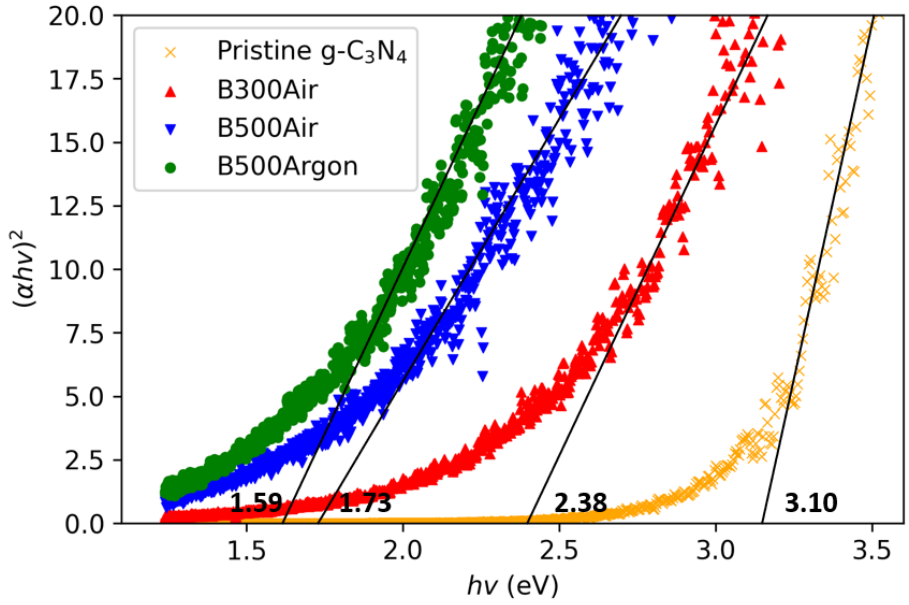

Figure 4.5: Obtained Tauc plots of pristine g-C_3N_4 (×), B300Air (△), B500Air (▽) and B500Argon (◯). In these sample names, B denotes boron-doped, 300 and 500 denote the synthesis temperature, and Air and Argon denote the atmosphere used in the doping synthesis.

To obtain the flat band potential and thus the location of the band edges, a Mott Schottky analysis was performed. The results are given in Figure 4.6 for pristine and boron-doped g-C_3N_4 at a frequency of 1 kHz and different pH. The samples display an n-type behavior, as the slopes in the linear part of the curves are positive. In general, the slope of these curves decreases when the pH is increased, where a more drastic decrease is observed when the pH is raised from 2 to 3. It is also observed that g-C_3N_4 does not follow a linear trend in the reduction of flat band potential with pH. It generally decreases for a pH up to 4.5, but for pristine g-C_3N_4 and B300Air, the flat band potential has increased again for a pH of 13. For B500Air and B500Argon, the flat band potential at a pH of 13 is approximately the same as that of a pH of 4.5.

In general, the flat band potentials of B300Air are located at more anodic values than pristine g-C_3N_4, especially for very acidic and alkaline solutions. The flat band potentials of B500Air and B500Argon are also located at slightly more anodic values at a pH of 0.3. However, as the pH increases, the flat band potentials become more cathodic or practically equal to those of pristine g-C_3N_4. The exception is for a pH of 3.3, where the Mott Schottky curves possess a small bump and give flat band potentials located at more anodic values than pristine g-C_3N_4.

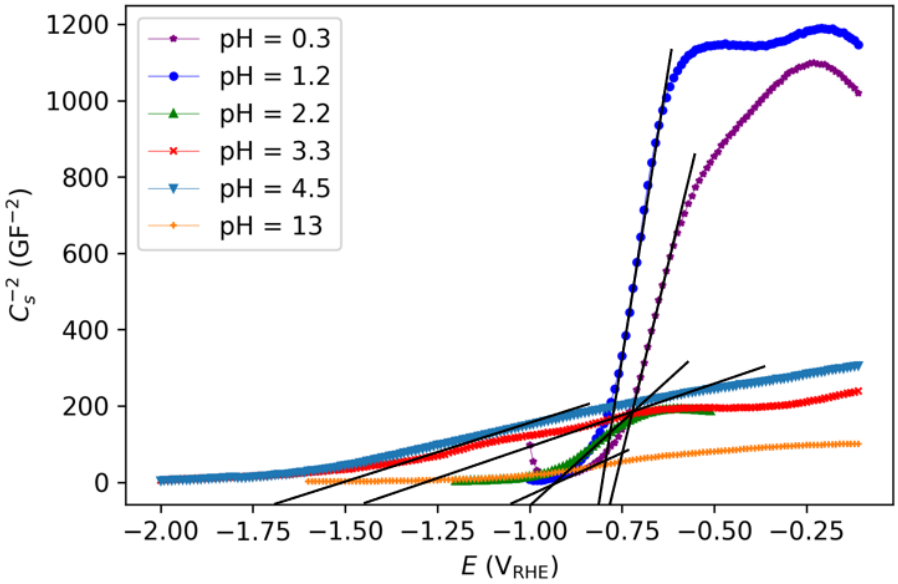
pH = 0.3
pH = 1.2
pH = 2.2
pH = 3.3
pH = 4.5
pH = 13
C_s^{-2} (GF^{-2})
E (V_{RHE})

(a)

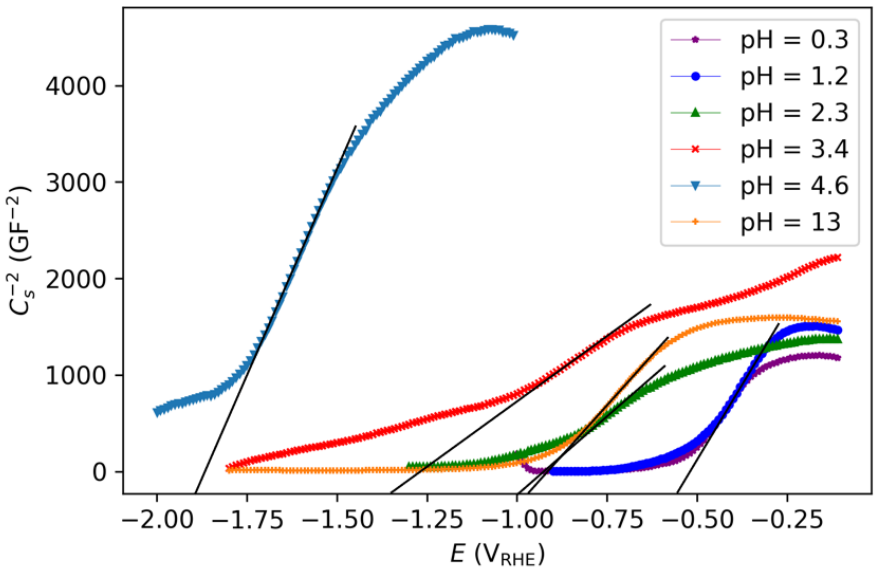
pH = 0.3
pH = 1.2
pH = 2.3
pH = 3.4
pH = 4.6
pH = 13
C_s^{-2} (GF^{-2})
E (V_{RHE})

(b)

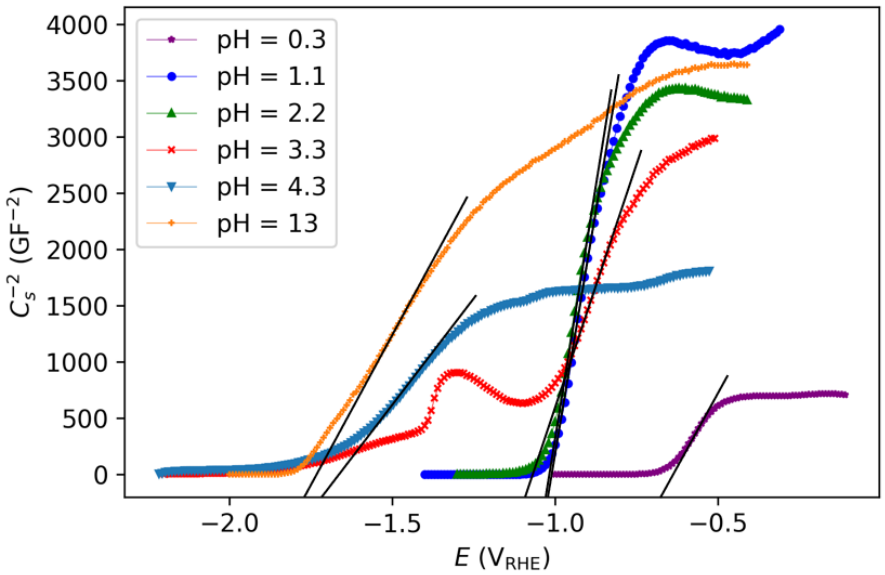

(c)

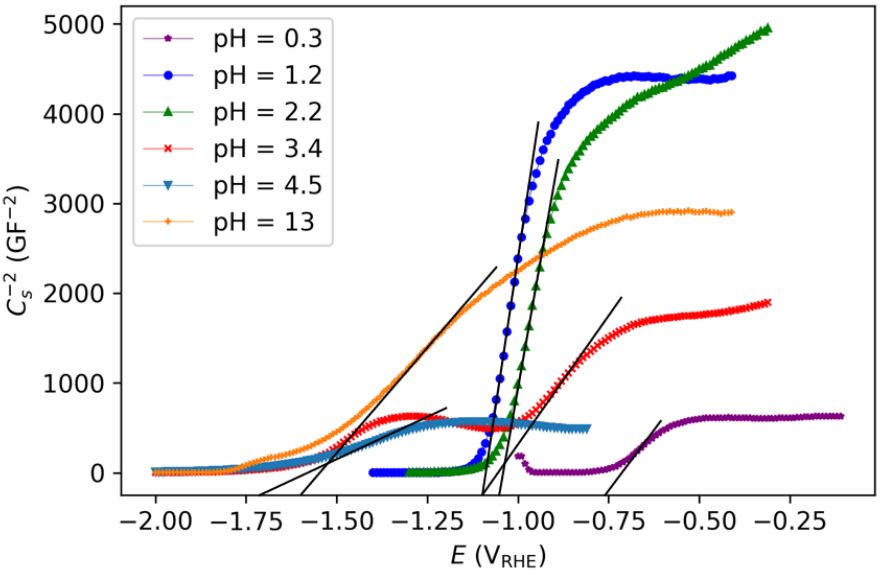

(d)

Figure 4.6: Mott Schottky plots of a) pristine g-C_3N_4, b) B300Air, c) B500Air and d) B500Argon at 1 kHz and different pH. In these sample names, B denotes boron-doped, 300 and 500 denote the synthesis temperature, and Air and Argon denote the atmosphere used in the doping synthesis. The potential measurements ranged from -2.2 V_{RHE} to -0.1 V_{RHE} with a potential step of 10 mV. The extrapolations of the linear parts of the curves are also demonstrated.

Visualizations of how the band gaps move with increasing pH are given in Appendix B, based on the Mott Schottky results. A Mott Schottky analysis was also performed for frequencies equal to 1.7 and 3 kHz at different pH, given in Appendix A. The analysis at 1 kHz was used as a basis due to less noise compared to 1.7 and 3 kHz. Additionally, the numeric values for the flat band potentials are also given in Appendix A. In general, a higher frequency leads to more cathodic values of the flat band potential and thus for the band edges, and more noise in the measurements.

The obtained values for the flat band potentials as a function of an acidic pH are given in Figure 4.7 for a frequency of 1 kHz. The flat band potential at a pH of 13 was not included as it did not follow the same trend as for acidic pH. The general trend is that the flat band potential becomes more cathodic when the pH is increased. Corresponding plots of flat band potentials as a function of pH are given in Appendix A for frequencies equal to 1.7 and 3 kHz.

A corresponding overview of how the measured flat band potential changes with acidic pH for a frequency of 1 kHz is given in Table 4.1. The respective linear fits of these pH-dependencies are given in Appendix A, along with the results from 1.7 and 3 kHz. For the boron-doped samples, an increased doping concentration leads to a reduced pH dependence of the flat band potential. The flat band potentials of B300Air display a higher pH dependence than those of pristine g-C_3N_4, while the flat band potentials of B500Air and B500Argon display a lower pH dependence than those of pristine g-C_3N_4. For an increased frequency, the flat band potentials' pH dependence generally increases.

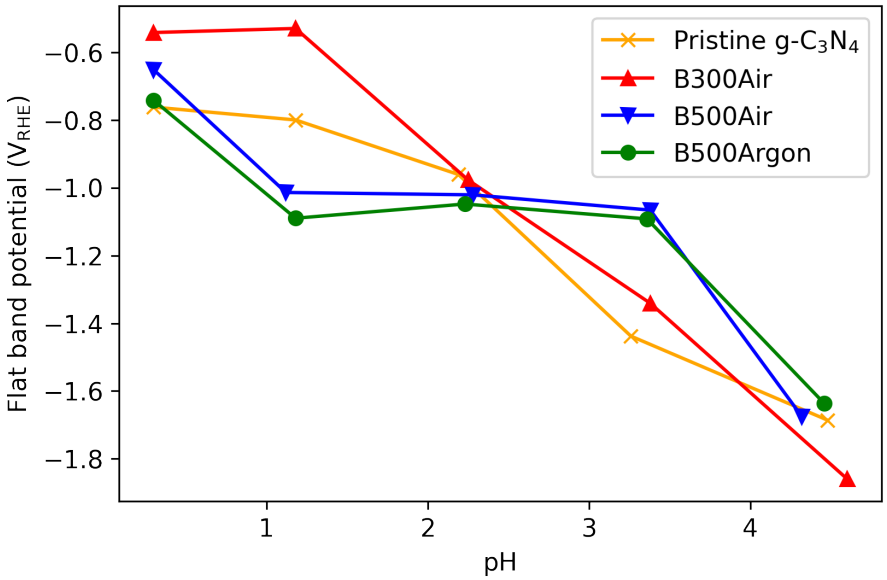

Figure 4.7: Measured flat band potentials vs. acidic pH for pristine g-C_3N_4 ($\times$), B300Air ($\triangle$), B500Air ($\triangledown$) and B500Argon ($\bigcirc$) at a frequency of 1 kHz. In these sample names, B denotes boron-doped, 300 and 500 denote the synthesis temperature, and Air and Argon denote the atmosphere used in the doping synthesis. The flat band potential moves towards more cathodic potentials with pH.

Table 4.1: Measured flat band potential as a function of acidic pH at a frequency of 1 kHz for pristine and boron-doped g-C_3N_4. For the sample names in the table, B denotes boron-doped, 300 and 500 denote the synthesis temperature, and Air and Argon denote the atmosphere used in the doping synthesis.

	Flat band potential vs. pH ($mVpH^{-1}$)
Pristine g-C_3N_4	-241
B300Air	-323
B500Air	-200
B500Argon	-170

To visualize the effects of doping on the flat band potential, Figure 4.8 displays Mott Schottky plots of pristine and boron-doped g-C_3N_4 at a frequency of 1 kHz and a pH of 2.2. From these plots, an increased slope in the linear parts of the curves is clearly visible. The flat band potential also shifts slightly towards more cathodic values for increasing boron content. The respective values can be found in Table A.1 in Appendix A.

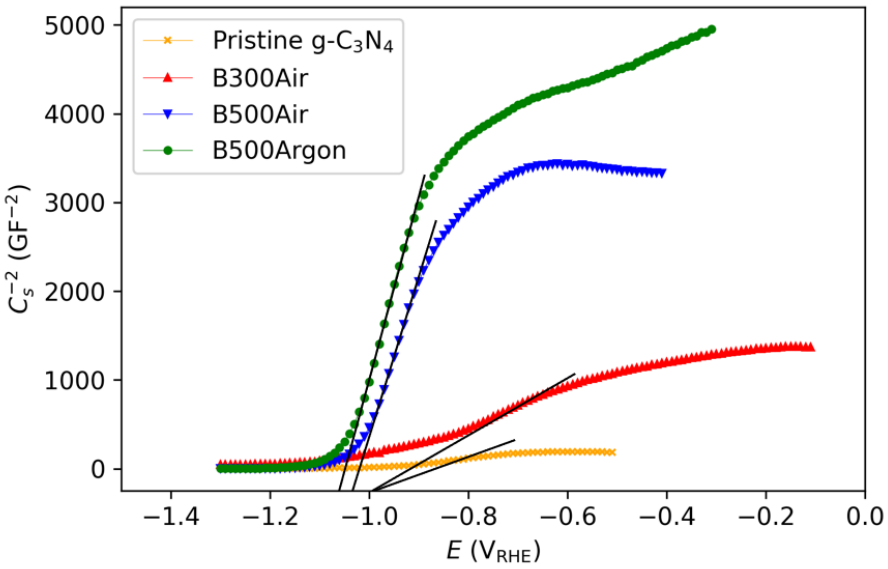

Figure 4.8: Mott Schottky plots of pristine g-C_3N_4 (×), B300Air (△), B500Air (▽) and B500Argon (◯) at a frequency of 1 kHz and a pH of 2.2. In these sample names, B denotes boron-doped, 300 and 500 denote the synthesis temperature, and Air and Argon denote the atmosphere used in the doping synthesis. The potential measurements ranged from -1.3 V_{RHE} to -0.1 V_{RHE} with a potential step of 10 mV.

To verify the placements of the band edges obtained by the Mott Schottky analysis, LSV of the $Fe(CN)_6^{3-/4-}$ redox couple was performed at a pH of 2.2 and 4.4 for pristine g-C_3N_4 and B500Argon. The results are given in Figure 4.9, where both anodic and cathodic faradaic currents exist for both samples, placing the Fermi level of the redox pair ($Fe(CN)_6^{3-/4-}$) approximately at the same potential as the VB of the semiconductors. At a pH of 2.2, this redox potential was measured to be around 0.63 V_{RHE}, but at a pH of 4.4, it was closer to 0.76 V_{RHE}. This can be seen in the LSV where the current is equal to zero.

The obtained maximum currents from the LSVs are much lower than the limiting currents for the $Fe(CN)_6^{3-/4-}$ redox couple, which could be obtained from the CV of the system without any g-C_3N_4. This is given in Figure C.1 in Appendix C, where the limiting anodic and cathodic currents are 11.7 and -11.2 mA, respectively.

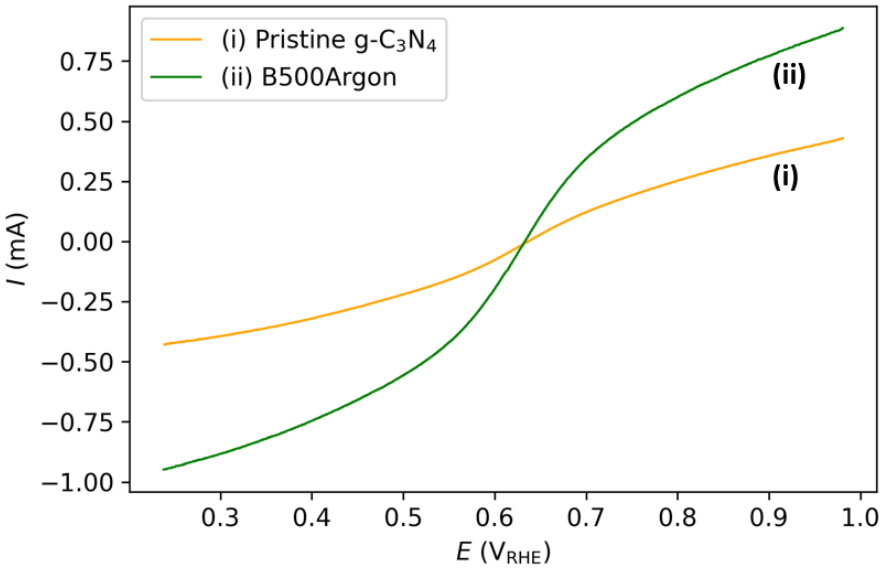

(a)

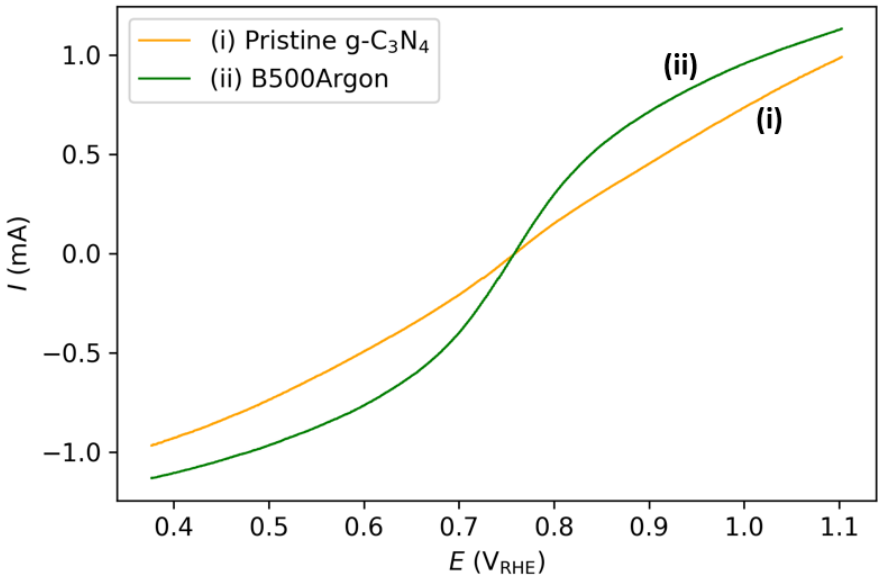

(b)

Figure 4.9: Linear sweep voltammetry of the $Fe(CN)_6^{3-/4-}$ redox couple for pristine g-C_3N_4 (i) and B500Argon (ii) at a) pH 2.2 and b) pH 4.4, centered around the redox potential of $Fe(CN)_6^{3-/4-}$. In the sample name, B denotes boron-doped, 500 denotes the synthesis temperature, and Argon denotes the atmosphere used in the doping synthesis. The potential was swiped from 0.98 V_{RHE} to 0.24 V_{RHE} for a pH of 2.2 and from 1.1 V_{RHE} to 0.38 V_{RHE} for a pH of 4.4 with a scan rate of -5 mVs^{-1}. The Fermi level of the redox pair was equal at 0.63 V_{RHE} for a pH of 2.2 and 0.76 V_{RHE} for a pH of 4.4.

For a pH of 2.2, the redox potential of $Fe(CN)_6^{3-/4-}$, and thus the VB of pristine g-C_3N_4 and B500Argon, is equal to 0.63 V_{RHE}. Pristine g-C_3N_4 has a band gap of 3.10 eV, placing the respective CB at -2.47 V_{RHE}. B500Argon has a band gap of 1.59 eV, placing the CB at -0.96 V_{RHE}. When compared with the results from the Mott Schottky analysis, the band edges of pristine g-C_3N_4 are located at much more cathodic potentials, while the band edges of B500Argon are located at slightly more anodic potentials. An illustration of this is given in Figure C.2 in Appendix C. Based on the Mott Schottky analysis, pristine g-C_3N_4 is suitable for the oxidation of MO, but B500Argon is not. Based on the results from the LSV of the $Fe(CN)_6^{3-/4-}$ redox couple, neither semiconductor sample is suitable for the oxidation of MO.

The same is the case for a pH of 4.4, where the CB of pristine g-C_3N_4 is located at -2.34 V_{RHE} and the CB of B500Argon is located at -0.83 V_{RHE}, according to the LSV of the $Fe(CN)_6^{3-/4-}$ redox couple. Here, the band edges of pristine g-C_3N_4 are more cathodic than for the Mott Schottky analysis, and the band edges of B500Argon are more anodic. As the VB of both pristine g-C_3N_4 and B500Argon is located at 0.76 V_{RHE}, neither semiconductor sample is suitable for the oxidation of MO.

4.4 Oxidation potential of methyl orange

The obtained CVs of 0.31 mM MO in 0.1 M Na_2SO_4 for different pH are given in Figure 4.10a, where only oxidation peaks of MO in acidic solutions are visible in the given potential range. MO displays oxidation potentials equal to 1.22-1.24 V_{RHE} for the acidic form of the dye (at a pH below 4.3 V_{RHE}), and closer to 1.3 V_{RHE} for the alkaline form of the dye (at a pH above 4.3 V_{RHE}). No reduction peaks are visible in the voltammograms, which indicates that the oxidation of MO is an irreversible reaction.

Only MO displayed clearly visible oxidation peaks in the voltammograms, so this was the only dye considered for further testing. CVs of 0.21 mM RhB in 0.1 M Na_2SO_4 are given in Figure D.1 in Appendix D. As the oxidation peaks only are evident for an acidic pH, a more thorough investigation of the oxidation potential as a function of different acidic pH was performed, as demonstrated in Figure D.2 in Appendix D. Here, the respective curve with oxidation potential as a function of pH for the acidic form of the dye is given in Figure 4.10b.

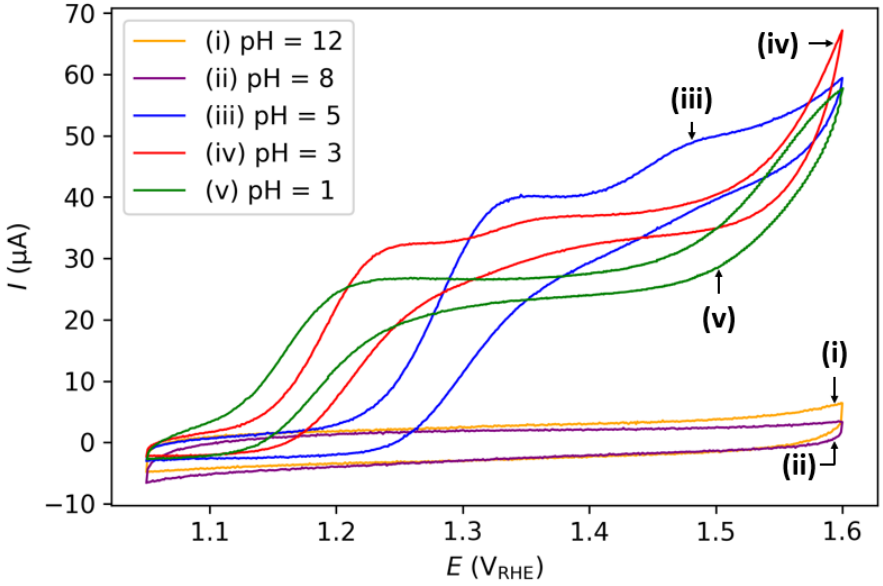

(a)

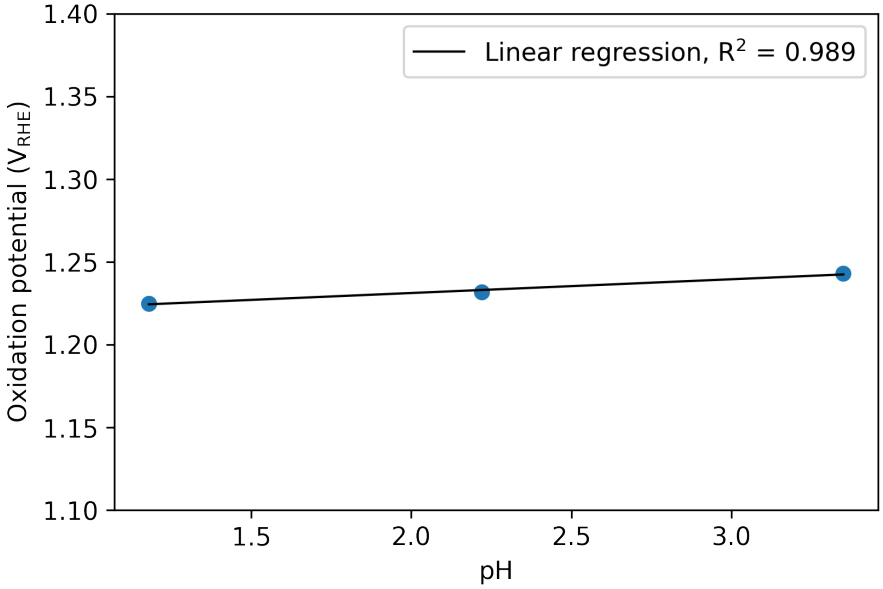

(b)

Figure 4.10: a) Obtained cyclic voltammetry displaying oxidation potentials for 0.31 mM methyl orange in 0.1 M Na_2SO_4 at different pH, from 1.05 V_{RHE} to 1.6 V_{RHE}, at a scan rate of 500 mVs^{-1} and b) the respective oxidation potential vs. pH for the acidic form of the dye. The linear fit has an R^2 value of 0.989 and a slope equal to 0.0083 VpH^{-1}.

The slope in the oxidation potential vs. pH curve is equal to 0.0083 VpH^{-1}, meaning the oxidation potential is practically independent of the pH for the acidic form of the dye.

4.5 Platinum deposition

To confirm the presence of platinum nanoparticles on the g-C_3N_4 substrates, both UV-visible spectroscopy during the sonochemical synthesis and S(T)EM were utilized. The obtained spectra from UV-visible spectroscopy are given in Appendix E, where a reduction of the PtI_6^{2-} peak indicates a reduction of the platinum(IV) ions to metallic platinum. The obtained S(T)EM images of pristine g-C_3N_4 are given in Figure 4.11 for both secondary electron (SE) and bright field (BF) modes. The platinum nanoparticles are clearly visible as the small dots deposited evenly across the g-C_3N_4 substrate. The corresponding measured particle size was (3.2 $\pm$ 1.8) nm.

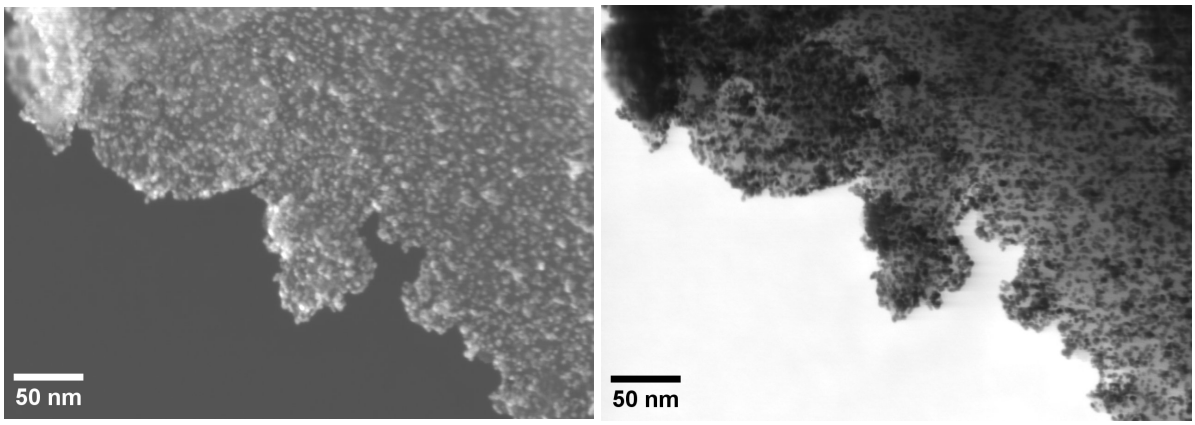

Figure 4.11: Scanning (Transmission) Electron Microscopy images of pristine g-C_3N_4 with deposited platinum nanoparticles in a) secondary electron mode and b) bright field mode. The measured size of the nanoparticles was (3.2 $\pm$ 1.8) nm.

To see if the platinum deposition was hindered by the boron doping, EDS of these samples was performed. The respective EDS spectra are given in Appendix E, and they indicate that platinum is present for all boron-doped samples.

4.6 Photoelectrochemical tests

IPCE was used to measure the photocurrent response of pristine and boron-doped g-C_3N_4. The resulting spectra are given in Figure 4.12 for different pH. The overall IPCE values for all samples are in the range of 0-2 μ%, which is quite low. Both pristine g-C_3N_4 and B500Air possess one peak located slightly higher than the rest, at 0.65 μ% for a pH of 0.3 and 1.77 μ% for a pH of 12.2, respectively. The corresponding wavelengths of light are 338 nm and 596 nm. B300Air possesses two such peaks, one at 350 nm with an IPCE of 1.34 μ% and one at 474 nm with an IPCE of 1.02 μ%. The respective values of the pH are 4.4 and 12.2. For B500Air, there are no peaks located at slightly higher IPCE values than the rest.

After the IPCE tests, the MO solution was subject to UV-visible spectroscopy to estimate the amount of oxidized dye after the illumination. The resulting spectra are given in Figure F.1 in Appendix F for the different pH values, where the measured absorption can be used to find the amount of oxidized MO. A summary of the amount of oxidized MO as a function of pH is given in Figure 4.13, with corresponding tabulated values given in Table F.1 in Appendix F. From this figure, it is observed that pristine g-C_3N_4 has oxidized the most MO for every pH above 0.3, but for a pH of 0.3, B500Argon and B500Air oxidized slightly more MO than pristine g-C_3N_4. At a pH of 12.2, no MO has been oxidized at all.

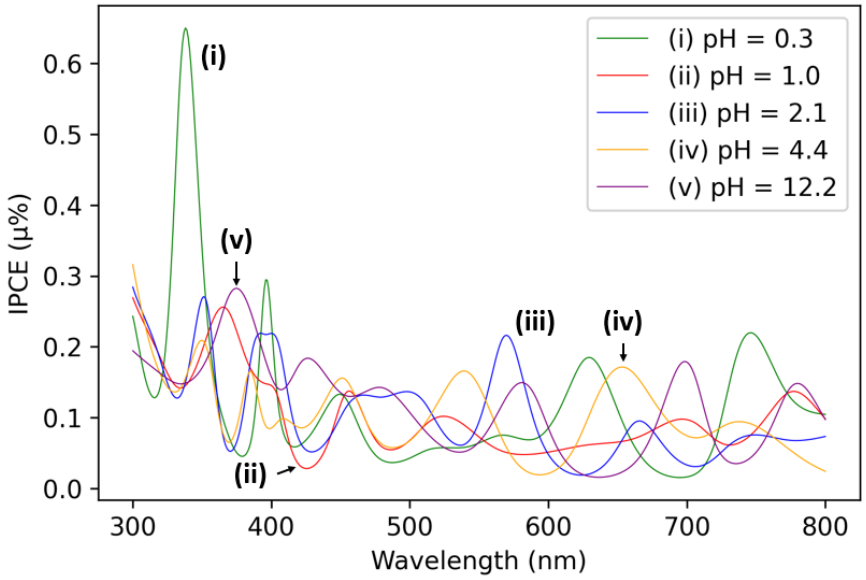
(i) pH = 0.3
(ii) pH = 1.0
(iii) pH = 2.1
(iv) pH = 4.4
(v) pH = 12.2
(i)
(v)
(iii)
(iv)
(ii)
IPCE (μ%)
Wavelength (nm)
0.0
0.1
0.2
0.3
0.4
0.5
0.6
300
400
500
600
700
800

(a)

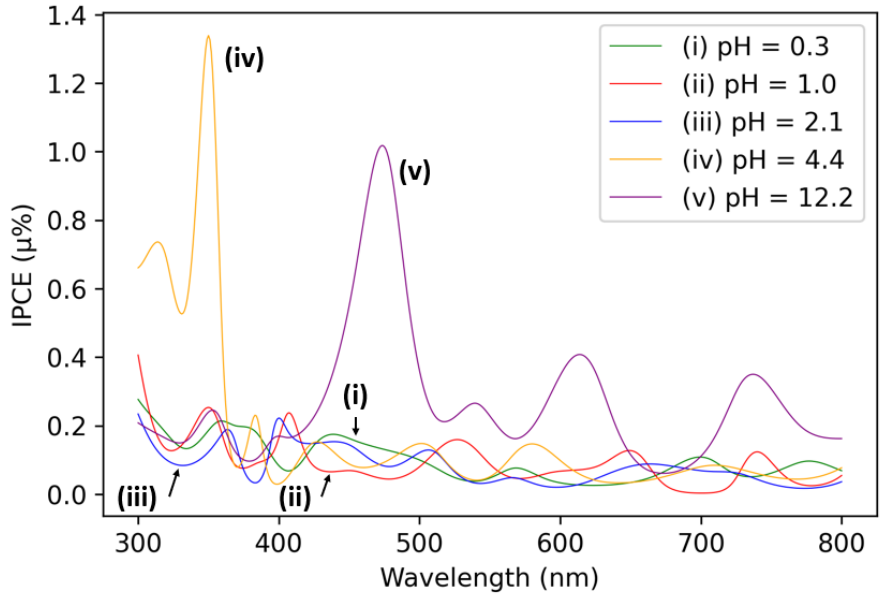
(i) pH = 0.3
(ii) pH = 1.0
(iii) pH = 2.1
(iv) pH = 4.4
(v) pH = 12.2
(iv)
(v)
(i)
(iii)
(ii)
IPCE (μ%)
Wavelength (nm)
0.0
0.2
0.4
0.6
0.8
1.0
1.2
1.4
300
400
500
600
700
800

(b)

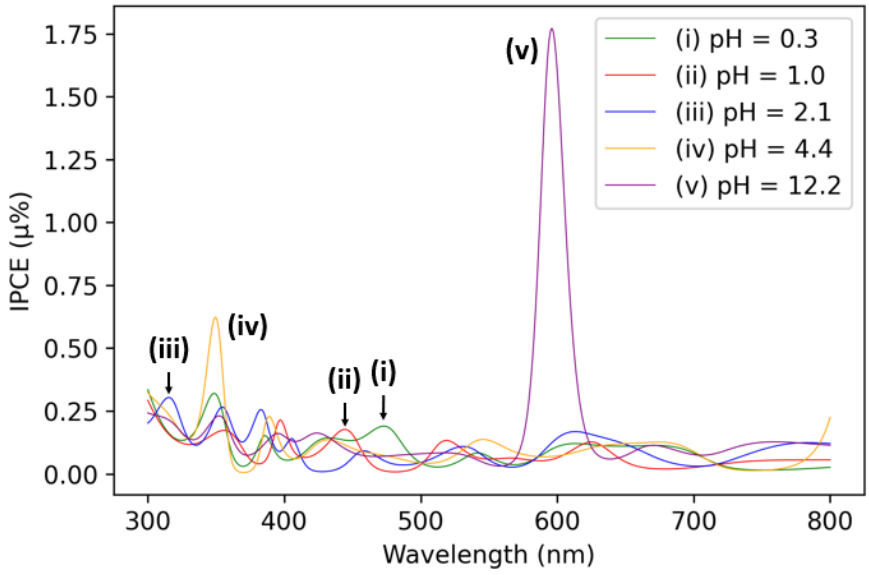

(c)

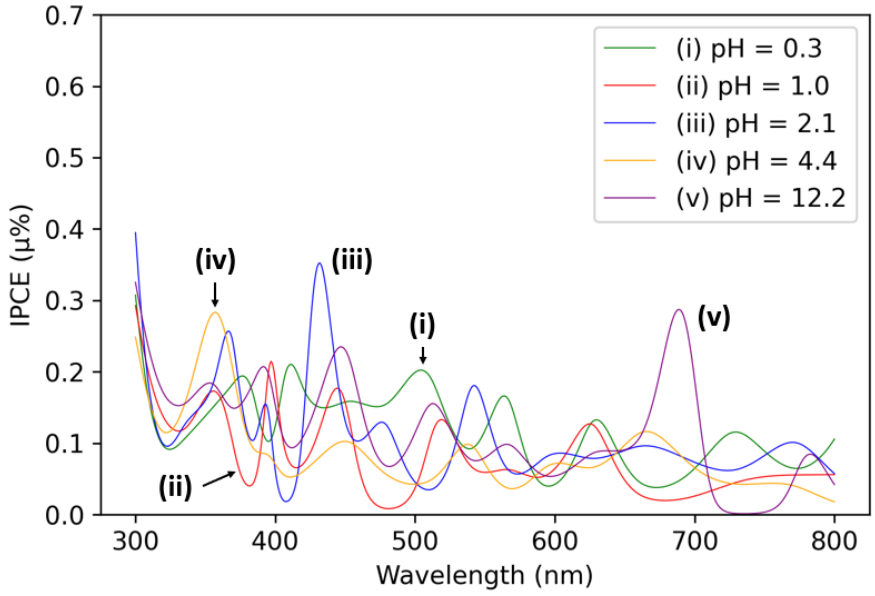

(d)

Figure 4.12: IPCE of a) pristine g-C_3N_4, b) B300Air, c) B500Air and d) B500Argon at different pH. In these sample names, B denotes boron-doped, 300 and 500 denote the synthesis temperature, and Air and Argon denote the atmosphere used in the doping synthesis. The curves were measured from 290 nm to 800 nm at 1 Hz. All IPCE values are in the range of 0-2 μ%.

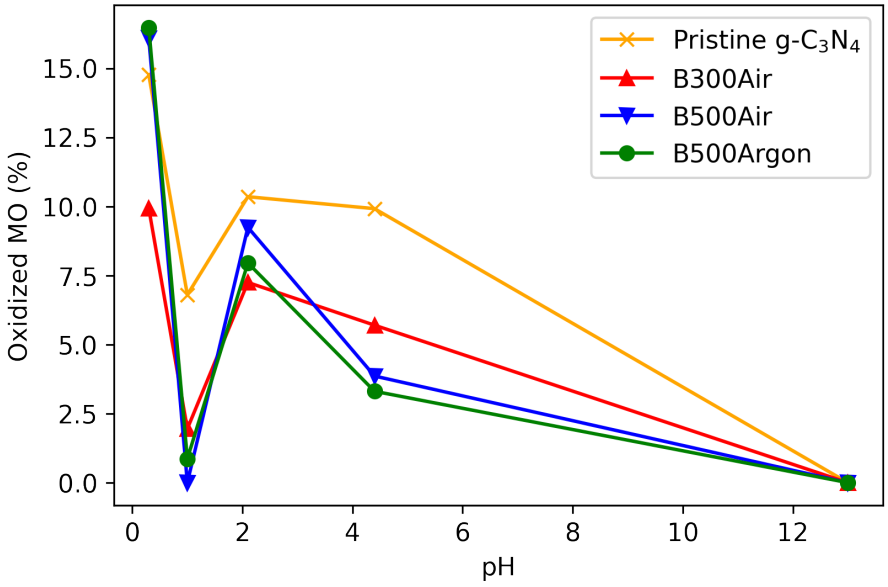

Figure 4.13: Amount of oxidized methyl orange as a function of pH for pristine g-C_3N_4 (×), B300Air (△), B500Air (▽), and B500Argon (◯). In these sample names, B denotes boron-doped, 300 and 500 denote the synthesis temperature, and Air and Argon denote the atmosphere used in the doping synthesis. The amount of oxidized methyl orange decreases with increasing pH.

4.7 Degradation of methyl orange

A degradation experiment of MO under illumination was conducted with pristine g-C_3N_4 and B500Argon, the two extremes in terms of the band gap, at a pH of 2.2 and 4.4. The obtained results are given in Table 4.2, where the corresponding absorption spectra are given in Appendix F. Both samples were more efficient at degrading MO at a pH of 2.2 compared to a pH of 4.4. At a pH of 2.2, B500Argon was more efficient than pristine g-C_3N_4, with 5.8% degraded MO after 60 minutes compared to 3.8%. For a pH of 4.4, pristine g-C_3N_4 was more efficient than B500Argon, with 3.0% degraded MO after 60 minutes compared to only 1.7%.

B500Argon without deposited platinum was also subject to this experiment at a pH of 4.4 to see how platinum affected the degradation of MO. These results are also given in Table 4.2, where the corresponding absorption spectrum is given in Appendix F. The amount of degraded MO is approximately the same for B500Argon with and without platinum.

Table 4.2: Calculated amount of degraded methyl orange from measured absorption peaks obtained from UV-visible spectroscopy after 60 minutes of illumination. The results are given for pristine g-C_3N_4 and B500Argon with and without platinum in electrolytes containing 0.12 mM methyl orange and a pH equal to 2.2 and 4.4. Here, B denotes boron-doped, 500 denotes the synthesis temperature, and Argon denotes the atmosphere used in the doping synthesis.

pH		Absorption peak	Degraded MO after 60 min (%)
2.2	MO before, pristine g-C_3N_4	1.839	
	MO after, pristine g-C_3N_4	1.769	3.8
2.2	MO before, B500Argon	1.940	
	MO after, B500Argon	1.827	5.8
4.4	MO before, pristine g-C_3N_4	1.559	
	MO after, pristine g-C_3N_4	1.512	3.0
4.4	MO before, B500Argon	1.968	
	MO after, B500Argon	1.934	1.7
4.4	MO before, B500Argon without Pt	1.375	
	MO after, B500Argon without Pt	1.350	1.8

5 Discussion

Oxidation of MO was used as a target reaction for the photocatalytic activity of g-C_3N_4, where the obtained results suggest that B500Air and B500Argon oxidized more MO than pristine g-C_3N_4 upon illumination at a low pH (Figure 4.13 and Table 4.2), due to the effect of band edge unpinning (Figure 4.9). As the pH was increased, the overall oxidation of MO was reduced and pristine g-C_3N_4 proved more efficient than the boron-doped samples, due to the flat band potentials, and thus the VBs, becoming more cathodic for the boron-doped samples (Figure 4.7).

Band edge unpinning may lead to an anodic shift of the flat band potential and thus of the band edges, as established by Kelly et al. [25]. This is due to the build-up of the minority carriers, holes, leading to an increased potential drop in the Helmholtz layer, and thus a downward shift of the energy bands, as explained in section 2.1.4. In turn, oxidation of MO upon illumination can be made possible even though the VBs are placed below the oxidation potential of MO in the dark. The occurrence of band edge unpinning in aqueous solutions can be found from the LSV of the $Fe(CN)_6^{3-/4-}$ redox couple without illumination (Figure 4.9). Here, the obtained value of the VB for B500Argon was located at a slightly more anodic potential than that obtained from the Mott Schottky analysis, illustrated in Figure C.2 in Appendix C. This anodic shift is an indication of band edge unpinning for the boron-doped sample, further supported by the Fermi level, as obtained from the Mott Schottky analysis, being located outside of the band gap. The same is not observed for pristine g-C_3N_4, where a cathodic shift of band edges is observed instead. Thus, the obtained Fermi level is located inside the band gap, some distance from the CB. As pristine g-C_3N_4 is theoretically an intrinsic semiconductor, this is a plausible explanation. In contrast, B500Argon is heavily doped, meaning that the approximation of the Fermi level being located at or near the CB is more valid. Thus, band edge unpinning is likely only occurring for the boron-doped sample in the dark. The reason why band edge unpinning occurs for this boron-doped sample in the dark is likely due to the presence of a good hole injector; $Fe(CN)_6^{3-}$.

In the dark, $Fe(CN)_6^{3-}$ may inject minority carriers, holes, into the surface states of g-C_3N_4, thus causing unpinning of the energy bands. This is possible if there is a good interaction between $Fe(CN)_6^{3-}$ and g-C_3N_4. In general, poor interaction between g-C_3N_4 and the electrolyte would lead to a poor transfer of holes across the semiconductor-electrolyte interface, as

stated by [10]. In the dark, this means that the electrolyte would not have been able to inject g-C_3N_4 with holes, and no unpinning of bands would occur due to a lack of built-up charge. As a small amount of band edge unpinning can be observed for B500Argon in the $Fe(CN)_6^{3-/4-}$ electrolyte, there appears to be an interaction between the g-C_3N_4 sample and the electrolyte. However, upon illumination in such an electrolyte, this would lead to the photogenerated holes being easily transported to the electrolyte, thus inhibiting band edge unpinning. This is due to the $Fe(CN)_6^{3-/4-}$ electrolyte also containing a good hole acceptor; $Fe(CN)_6^{4-}$. For poor interaction between g-C_3N_4 and the electrolyte, the photogenerated holes will instead accumulate at the semiconductor-electrolyte interface, resulting in increased band edge unpinning. Thus, the amount of band edge unpinning is different with and without illumination for a given electrolyte. Upon illumination, the g-C_3N_4 samples are immersed in electrolytes containing water and MO. For some layered n-type semiconductors, low interaction with water is the case in aqueous solutions, which could also be the case for g-C_3N_4 [10]. Additionally, if MO is a poor hole acceptor, this would further increase the amount of band edge unpinning. If a low interaction is the case, a high amount of band edge unpinning can occur upon illumination in an aqueous electrolyte.

As the MO oxidation is possible upon illumination, a higher amount of band edge unpinning likely occurs for illumination compared to that in the dark. This is indicated by the obtained VBs in the dark, which are located at more cathodic potentials than the oxidation potential of MO. An explanation for this higher amount of unpinning upon illumination is likely that more holes are generated, and thus accumulated at the semiconductor-electrolyte interface, by the incoming light compared to what $Fe(CN)_6^{3-}$ can inject into the semiconductor in the dark. If this is the case, then a reduced band gap would lead to more photogenerated holes and thus more band edge unpinning. This means that the amount of boron in the samples affects the amount of unpinning. In addition to the size of the band gap, the amount of boron in the g-C_3N_4 samples may also affect the number of surface states in the semiconductor. If the boron-doped samples generate more surface states in the semiconductor compared to pristine g-C_3N_4, they also have the ability to generate more build-up of charge and thus more unpinning of bands. Studies performed on other systems have reported an increase in generated surface states when dopants were added to the substrate [47][48]. Thus, the introduced boron in the g-C_3N_4 samples may have led to a larger amount of band edge unpinning due to more photogenerated holes accumulating in more surface states. However, the number of surface

states in the g-C_3N_4 samples are likely the same with and without illumination, indicating that the amount of unpinning is not saturated in the dark.

The amount of band edge unpinning is likely unsaturated in the dark, but as light with higher intensities is incident on the semiconductor upon illumination, the amount of band edge unpinning saturates. The saturation is a result of all surface states in the semiconductor becoming occupied by the photogenerated holes, as stated by Kelly et al. [25]. This assumption is supported by the occurrence of band edge unpinning for pristine g-C_3N_4 during illumination, but not in the dark, which makes the oxidation of MO possible. A saturation results in the existence of a maximum value for the VBs at a pH of 0.3, decreasing with an increasing pH (Figure 4.13). This indicates a pH dependence of the obtained overpotential towards the MO oxidation.

The amount of oxidized MO, and thus the overpotential for this oxidation reaction, is clearly pH dependent (Figure 4.13 and Table 4.2). Generally, a higher amount of MO is oxidized at a lower pH, with the exception of a pH equal to 1 for the IPCE measurements. Additionally, no MO has been oxidized at all at a pH of 12.2, which is expected due to the absence of an oxidation potential of MO in alkaline solutions for the given potential range (Figure 4.10a). The higher amount of oxidized MO at a lower pH is likely due to a higher overpotential towards this oxidation reaction, due to both more anodic VBs and more cathodic oxidation potentials for the MO (Figure 4.10). For all the g-C_3N_4 samples, the band edge unpinning is likely the reason why oxidation of MO is possible, but the amount of unpinning under illumination appears to be unaffected by the increase in pH.

The pH independence of the band edge unpinning is indicated by the Mott Schottky results (Figure 4.7). Here, a cathodic change in flat band potential, and thus the Fermi level and the VB, is observed for an increased pH. For the pH changing from 0.3 to 4.5 for pristine g-C_3N_4 and B500Argon, the extremes in terms of the band gap are illustrated in Figure 5.1. The oxidation potential of MO also shifts to slightly more anodic potentials for an increasing pH, but this is less prominent than the shift of the Fermi level. The expected result in terms of MO oxidation is thus a decrease in efficiency, which is observed in the experimental results (Figure 4.13 and Table 4.2). This indicates that the amount of band edge unpinning upon illumination is not enough to compensate for the cathodic movement of the VB, supporting the assumption of a saturated band edge unpinning upon illumination, and thus independence of the pH. Without illumination, however, the amount of band edge unpinning appears to be pH-dependent.

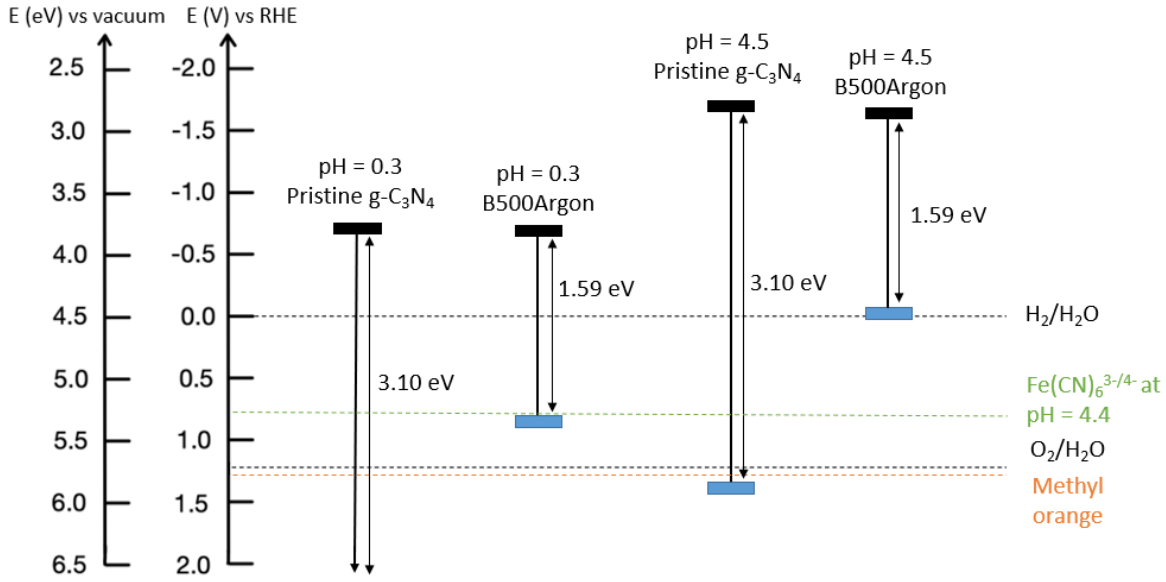

Figure 5.1: Band edges of pristine g-C_3N_4 and B500Argon at a pH of 0.3 and 4.5, based on the Mott Schottky results. In this sample name, B denotes boron-doped, 500 denotes the synthesis temperature, and Argon denotes the atmosphere used in the doping synthesis. The oxidation potential of methyl orange aligns with that of the oxygen evolution reaction at a pH of 0.3 and is added as the orange dashed line for a pH of 4.5. The redox potential of the $Fe(CN)_6^{3-/4-}$ couple at a pH of 4.4, the most anodic potential of those measured, is also given.

The band edge unpinning of B500Argon without illumination, as given by the LSV of the $Fe(CN)_6^{3-/4-}$ redox couple (Figure 4.9), display a strong pH dependence. At a pH of 2.2, a slight anodic shift of 90 mV occurs (illustrated in Figure C.2), but at a pH of 4.4, this anodic shift is equal to 810 mV. This is also shown in Figure 5.1, where the VB would thus be located at the redox potential of $Fe(CN)_6^{3-/4-}$. This means that far more holes are injected into the B500Argon sample at a higher pH, which could be due to the lower concentration of H^+ ions in the electrolyte solution. If H^+ ions are poor hole injectors for g-C_3N_4, they will not contribute to the unpinning of energy bands in this process. Thus, they might instead prevent the injection of holes into the semiconductor by blocking the $Fe(CN)_6^{3-}$ ions from reaching the semiconductor surface. This assertion could be supported by the Mott Schottky results (Figure 4.6), which display a decreasing amount of available donors at the semiconductor surface for a more acidic pH, as the slopes of the plots increase. Thus, this can be interpreted as the protons in the electrolyte solution occupying these donors, which are electron-rich nitrogen atoms for g-C_3N_4, as stated by Das et al. [21]. This effect is also more prominent for the boron-doped samples

compared to pristine g-C_3N_4, as Figure 4.8 demonstrates a lower amount of available donors for an increased boron content at a given pH. For a lower pH, the injection of holes into the semiconductor from $Fe(CN)_6^{3-}$ is, therefore, more difficult than at a higher pH, leading to more band edge unpinning for a higher pH. This pH dependence is thus a result of a lack of saturated band edge unpinning without illumination, as more holes can be trapped in surface states at an increased pH. Upon illumination, the band edge unpinning saturates, and more MO can be oxidized. The exception is for a pH of 1, where all samples oxidized less than expected according to the trend (Figure 4.13).

The oxidation of MO after the IPCE tests is clearly decreasing with increasing pH, except for a pH of 1 (Figure 4.13). Here, a dip in the amount of oxidized MO is observed for all samples, which may indicate a lower overpotential for the MO oxidation at this pH. The overpotential towards MO oxidation is dependent on the potential of the VB and the oxidation potential of MO. As the oxidation potential of MO is approximately the same as that of a pH of 0.3 and 2.1 (Figure 4.10b), the most likely cause of a reduced overpotential is the placement of the VB. When the samples are illuminated, a saturation of the amount of band edge unpinning occurs, leading to an anodic shift of the VB, the size which is most likely independent of the pH. Thus, the placement of the VB before illumination is likely the issue, which is dependent on the measured Fermi level from the Mott Schottky analysis (Figure 4.7). For pristine g-C_3N_4 and B300Air, the Fermi level lies closer to that of a pH equal to 0.3, but for B500Air and B500Argon the Fermi level is much closer to that of a pH equal to 2.2. Thus, for pristine g-C_3N_4 and B300Air, the amount of oxidized MO at a pH of 1 should have been closer to that of a pH of 0.3. For B500Air and B500Argon, the amount of oxidized MO should have been closer to that of a pH of 2.2, due to the approximately constant value of the oxidation potential of MO. However, since this dip is observed for all samples at this pH, another concern is related to experimental parameters concerning the electrolyte solution. This can i.e., be the distribution of the oxidized MO in the solution, related to the extracted amount that was further examined. In terms of pH, this is not the only deviation found in the study. For a pH of 2.2, the photocatalytic efficiency of B500Argon relative to pristine g-C_3N_4 is different for the MO oxidation after the IPCE and the degradation experiments.

At a pH of 2.2, B500Argon is more efficient than pristine g-C_3N_4 in terms of degrading MO, but this is not the case for the IPCE measurements. As the general amounts of oxidized MO

after illumination for 60 minutes are lower than those after the IPCE measurements, it could indicate a lower amount of light incident on the g-C_3N_4 particles. This may be a natural consequence of the light being incident directly on the semiconductor particles on a carbon paper substrate for the IPCE measurements, whereas in the degradation experiments, the semiconductor particles were simply mixed into the MO solution. Thus, the incident light may not have hit all the semiconductor particles in the MO solution and the corresponding distribution of the particles is of importance. If B500Argon has higher miscibility in the MO solution compared to pristine g-C_3N_4, more light could have been incident on these particles. At a pH of 4.4, pristine g-C_3N_4 is again more efficient than B500Argon in terms of MO oxidation, which is in accordance with the results from the IPCE measurements. This indicates that the reduced overpotential for the MO oxidation at a pH of 4.4 for B500Argon may have dominated over the easier miscibility of B500Argon in the MO solution. Even though the amounts of oxidized MO after the IPCE measurements are higher than for the degradation experiments, these are still overall low amounts of oxidized MO. This could be a result of a low generated photocurrent, as can be seen by the low values for the IPCE measurements (Figure 4.12).

The obtained values for the IPCE measurements (Figure 4.12) are all very low, likely a result of a too high loading of co-catalyst on the g-C_3N_4 substrates. As all the values for the IPCE are in the range of 0-2 μ%, a lot of this response may be noise instead of an actual response from the photocurrent. The occurrence of band edge unpinning is known to reduce the generated photocurrent, but low IPCE values are obtained for all samples, even though the amount of unpinned bands may vary for the different samples. Thus, a more plausible explanation for the low IPCE values could be drawn from the deposited platinum co-catalyst.

As the g-C_3N_4 samples are deposited with a relatively high amount of platinum, this may cause a blockage of the g-C_3N_4 substrate from the incoming light and thus low IPCE values. In this study, 20 wt% platinum was used, which may be too high. If this is the case, a very low photocurrent will be generated. Previous studies performed on the same system, but with 1 wt% platinum instead of 20 wt%, obtained IPCE values up to 0.25‰, indicating more light incident on the g-C_3N_4 substrate [49]. Thus, an optimum concentration of deposited platinum exists, where 20 wt% is too much to be effective. However, other contributions such as recombination and high charge transfer resistance would also lead to a lowered photocurrent response and thus lower IPCE, but likely not as much as the deposited platinum. Still, these contributions would

have to be investigated further to examine their effect on the obtained IPCE values. In terms of degraded MO, platinum is likely also a major cause of the overall low amount of oxidized MO.

Due to the low value of the IPCE, only a small photocurrent is generated and available for the degradation of MO, meaning that the co-catalyst is of importance in terms of catalyzing the oxidation reaction. After 60 minutes of illumination, less than 6% of the MO had been degraded by all samples (Table 4.2), which is a relatively low amount. From the results reported for B500Argon without platinum (Table 4.2), it is clear that platinum is not an optimal co-catalyst for the degradation of MO, as the same amount of MO is oxidized for B500Argon with and without platinum. Other co-catalysts such as nickel have proven to be more efficient in this regard [21]. Still, some MO has been oxidized after illumination, for which the amount varies with the concentration of boron in the g-C_3N_4 samples. This means that the discussed explanations given up to this point all assume a successful doping synthesis.

As can be seen in in Figures 4.2, 4.3, 4.4 and 4.5, boron has been successfully incorporated into the lattice of g-C_3N_4. For the XRD analysis, the reduced intensity of the main peaks situated at $2\theta = 13^\circ$ and 27.4° is an indication of a successful doping synthesis [6]. Additionally, the broadening of the main peak located at $2\theta = 27.4^\circ$ may also indicate successful doping as the dopant atoms cause a hindrance of crystal growth and inhibition of polymeric condensation of g-C_3N_4 [21]. For the FTIR results, the increased size of the N≡C- peak at 2180 cm^{-1} indicates an increased amount of boron incorporated into the g-C_3N_4 lattice [6]. As no new peaks were generated after the doping synthesis, apart from the one at 2180 cm^{-1}, this suggests that the structural framework remains intact after doping [21]. Furthermore, the results obtained from DRS and the respective Tauc plots show that the boron-doped samples utilize more of the available light as the reflectance has been reduced and that the band gaps are reduced with increasing concentration of dopant. Additionally, the increased amount of boron can be seen as an increased slope in the Mott Schottky plots (Figure 4.8). Here, the number of donors in the semiconductor-electrolyte interface is decreased with increasing boron content in the lattice. This is likely due to electronic interactions between the donors of g-C_3N_4 and the dopant atoms [21]. Thus, these results indicate an evident incorporation of boron into the g-C_3N_4 lattice. The incorporation of boron resulted in B500Air and B500Argon being more photocatalytic efficient than pristine g-C_3N_4 at a pH of 0.3, as measured towards the MO oxidation, but also to less efficient oxidation at an increased pH, compared to pristine g-C_3N_4.

6 Conclusion

The obtained results indicate that the introduced boron has reduced the band gap, placed the band edges at slightly more cathodic potentials, and increased the effect of band edge unpinning. As a result, heavily boron-doped g-C_3N_4 is approximately 2% more efficient than pristine g-C_3N_4 in terms of oxidation of MO at a pH of 0.3, for which further optimization can likely improve this efficiency. As the pH increased, the overpotential and thus driving force for the MO oxidation became larger for pristine g-C_3N_4 than for the boron-doped samples. The main reason for this was the more anodic band edges for pristine g-C_3N_4 due to a more anodic Fermi level, as the amount of band edge unpinning was saturated upon illumination and thus independent of the pH. An overall low amount of oxidized MO was observed for all samples, likely due to very low generated photocurrents for the samples. Band edge unpinning leads to a reduced photocurrent, but the main cause for the low IPCE values was probably the amount of deposited platinum on the g-C_3N_4 substrates. Thus, the deposited platinum may have blocked the g-C_3N_4 substrates from the incoming light, as 20 wt% platinum was too much. Furthermore, platinum was a rather poor co-catalyst for MO oxidation. If another target reaction, such as the HER, is used, platinum may prove to be a more efficient co-catalyst.

7 Further Work

In this study, the target reaction for the photocatalytic activity of g-C_3N_4 was the oxidation of MO. To further investigate the photocatalytic efficiency of the HER, gas chromatography (GC) is a useful test method where the amount of evolved hydrogen gas can be measured as a function of time. Another test method that can be used to investigate the HER for the g-C_3N_4 samples is LSV, where the obtained cathodic current can be used as an indication of the amount of developed hydrogen gas. As platinum is a co-catalyst for hydrogen evolution, different concentrations of deposited platinum on the g-C_3N_4 substrate can be investigated with the HER as the target reaction. Thus, an optimum concentration in terms of reduced recombination and increased photocurrent response can be obtained. It was clear from this study that 20 wt% platinum was too much. Furthermore, thermogravimetric analysis (TGA) can be performed to determine the real amount of wt% platinum, as only a theoretical value has been operated with in this study.

Furthermore, it would be interesting to investigate the effect of different co-catalysts for the oxidation of MO, such as i.e., nickel. As seen in this study, platinum is not an optimal co-catalyst for the MO oxidation reaction; it is more suitable for the hydrogen evolution reaction. If more suitable co-catalysts for the MO oxidation are found, the reaction rate as a function of pH can also be investigated for the different co-catalysts. Lastly, the usage of other organic dyes to measure the photocatalytic activity of g-C_3N_4 can be investigated. Rhodamine B was not prioritized in this study due to a lack of observed oxidation peaks, but other studies have reported successful degradation of this dye by g-C_3N_4 [8][50].

To investigate the behavior of g-C_3N_4 upon illumination, such as the effect of band edge unpinning, more closely, chopped light voltammetry can be performed. Chopped light voltammetry can also be used to investigate the effect of recombination. As both band edge unpinning and recombination lead to a reduced generated photocurrent, a closer investigation of these contributions are beneficial to better evaluate and improve the photocatalytic activity of g-C_3N_4.

Another contribution that might reduce the overall generated photocurrent is the charge transfer resistance. This can be investigated using electrochemical impedance spectroscopy (EIS), where the internal charge transfer resistance can be estimated from the resulting spectra. As the charge transfer resistance of g-C_3N_4 may change upon illumination, EIS both in the dark

and upon illumination is interesting to investigate.

The charge transfer resistance can't be used as a direct indicator of conductivity, meaning that proper conductivity measurements, such as the van der Pauw method or current sensing atomic force microscopy (CS-AFM), could be performed to evaluate the effect of doping on conductivity. For the van der Pauw method, a 4-point probe measurement is used for thin films to measure the conductivity. This method can also be used to give more quantitative results of the doping. The CS-AFM technique is used to determine the local conductivity of samples for different voltages. Pristine g-C_3N_4 has a relatively low conductivity, which means that an increase in this could lead to more efficient charge transport to the semiconductor-electrolyte interface.

In this study, two different methods were used to obtain the placements of the VB in aqueous solutions for the g-C_3N_4 samples; Mott Schottky and LSV of the $Fe(CN)_6^{3-/4-}$ redox couple. As they obtained different results, other methods such as X-ray photoelectron spectroscopy (XPS) may be used to more precisely determine the positions of the VBs for the g-C_3N_4 powders. This is performed for boron-doped g-C_3N_4 samples by Zhao et al. [6] and Wen et al. [7].

A doping synthesis using $NaBH_4$ was utilized in this study, but another boron source that is less toxic and safer to operate would be more desirable to use. Therefore, different doping syntheses would be interesting to investigate. Additionally, the effect of different dopants can be investigated.

References

[1] UN, "The 17 goals." `https://sdgs.un.org/goals`. Accessed: 2022-09-06.

[2] SINTEF, "About Green Hydrogen." `https://www.sintef.no/projectweb/greenh2webinars/about-green-hydrogen/`. Accessed: 2022-12-12.

[3] A. J. Nozik and R. Memming, "Physical Chemistry of Semiconductor-Liquid Interfaces," *The Journal of Physical Chemistry*, vol. 100, no. 31, pp. 13061–13078, 1996.

[4] S. Kumar, K. Sekar, and A. Lee, "g-C3N4-Based Nanomaterials for Visible Light-Driven Photocatalysis," *Catalysts*, vol. 8, p. 74, 2018.

[5] H. Wang, M. Thangamuthu, Z. Wu, J. Yang, H. Yuan, M. K. Bayazit, and J. Tang, "Self-assembled sulphur doped carbon nitride for photocatalytic water reforming of methanol," *Chemical Engineering Journal*, vol. 445, p. 136790, 2022.

[6] D. Zhao, C.-L. Dong, B. Wang, C. Chen, Y.-C. Huang, Z. Diao, S. Li, L. Guo, and S. Shen, "Synergy of Dopants and Defects in Graphitic Carbon Nitride with Exceptionally Modulated Band Structures for Efficient Photocatalytic Oxygen Evolution," *Advanced Materials*, vol. 31, no. 43, p. 1903545, 2019.

[7] Y. Wen, D. Qu, L. An, X. Gao, W. Jiang, D. Wu, D. Yang, and Z. Sun, "Defective g-C3N4 Prepared by the NaBH4 Reduction for High-Performance H2 Production," *ACS Sustainable Chemistry & Engineering*, vol. 7, no. 2, pp. 2343–2349, 2019.

[8] S. C. Yan, Z. S. Li, and Z. G. Zou, "Photodegradation of Rhodamine B and Methyl Orange over Boron-Doped g-C3N4 under Visible Light Irradiation," *Langmuir*, vol. 26, no. 6, pp. 3894–3901, 2010. PMID: 20175583.

[9] T. R. J. D., *Understanding Solids: the Science of Materials*. Wiley & Sons, 2nd ed., 2013.

[10] R. Memming, *Semiconductor Electrochemistry*. Wiley-VCH, 1st ed., 2001.

[11] K. B. Oldham, J. Myland, and A. M. Bond, *Electrochemical Science and Technology: Fundamentals and Applications*. Wiley & Sons, 1st ed., 2012.

[12] Y. Yu, K. A. Click, S.-C. Chien, J. Sun, A. Curtze, L.-C. Lin, and Y. Wu, "Decoupling pH

Dependence of Flat Band Potential in Aqueous Dye-Sensitized Electrodes," *The Journal of Physical Chemistry C*, vol. 123, no. 14, pp. 8681–8687, 2019.

[13] I. A. Lervik, M. Tsypkin, L.-E. Owe, and S. Sunde, "Electronic structure vs. electrocatalytic activity of iridium oxide," *Journal of Electroanalytical Chemistry*, vol. 645, no. 2, pp. 135–142, 2010.

[14] M. Ismael, Y. Wu, D. H. Taffa, P. Bottke, and M. Wark, "Graphitic carbon nitride synthesized by simple pyrolysis: role of precursor in photocatalytic hydrogen production," *New J. Chem.*, vol. 43, pp. 6909–6920, 2019.

[15] S. J. Mun and S.-J. Park, "Graphitic Carbon Nitride Materials for Photocatalytic Hydrogen Production via Water Splitting: A Short Review," *Catalysts*, vol. 9, no. 10, 2019.

[16] N. H. Nygård, "Synthesis of a graphitic carbon nitride electrode for hydrogen production by photoelectrolysis of water and ultrasound deposition of nanoparticles," *NTNU Open*, 2021.

[17] X. Wang, C. Liow, A. Bisht, X. Liu, T. C. Sum, X. Chen, and S. Li, "Engineering Interfacial Photo-Induced Charge Transfer Based on Nanobamboo Array Architecture for Efficient Solar-to-Chemical Energy Conversion," *Advanced Materials*, vol. 27, no. 13, pp. 2207–2214, 2015.

[18] L. M. Peter, A. B. Walker, T. Bein, A. G. Hufnagel, and I. Kondofersky, "Interpretation of photocurrent transients at semiconductor electrodes: Effects of band-edge unpinning," *Journal of Electroanalytical Chemistry*, vol. 872, p. 114234, 2020. Dr. Richard Compton 65th birthday Special issue.

[19] F. Decker and S. Cattarin, "PHOTOELECTROCHEMICAL CELLS | Overview," in *Encyclopedia of Electrochemical Power Sources* (Jürgen Garche, ed.), pp. 1–9, Amsterdam: Elsevier, 2009.

[20] H. Chou, B. J. Hwang, and C. L. Sun, "Chapter 9 - catalysis in fuel cells and hydrogen production," in *New and Future Developments in Catalysis* (S. L. Suib, ed.), pp. 217–270, Amsterdam: Elsevier, 2013.

[21] D. Das, D. Banerjee, M. Mondal, A. Shett, B. Das, N. Das, U. Ghorai, and K. Chattopadhyay, "Nickel doped graphitic carbon nitride nanosheets and its application for dye degradation by chemical catalysis," *Materials Research Bulletin*, vol. 101, pp. 291–304, 2018.

[22] A. Tripathi and S. Narayanan, "Potassium doped graphitic carbon nitride with extended optical absorbance for solar light driven photocatalysis," *Applied Surface Science*, vol. 479, pp. 1–11, 2019.

[23] P.-W. Chen, K. Li, Y.-X. Yu, and W.-D. Zhang, "Cobalt-doped graphitic carbon nitride photocatalysts with high activity for hydrogen evolution," *Applied Surface Science*, vol. 392, pp. 608–615, 2017.

[24] B. Wardle, *Principles and Applications of Photochemistry*. John Wiley & Sons, 1st ed., 2009.

[25] J. J. Kelly and R. Memming, "The Influence of Surface Recombination and Trapping on the Cathodic Photocurrent at p-Type III-V Electrodes," *Journal of The Electrochemical Society*, vol. 129, p. 730, apr 1982.

[26] C. Sinn, D. Meissner, and R. Memming, "Charge Transfer Processes at WSe2 Electrodes with pH-Controlled Stability," *Journal of The Electrochemical Society*, vol. 137, p. 168, Jan 1990.

[27] H. Lin, J. Wu, F. Zhou, X. Zhao, P. Lu, G. Sun, Y. Song, Y. Li, X. Liu, and H. Dai, "Graphitic carbon nitride-based photocatalysts in the applications of environmental catalysis," *Journal of Environmental Sciences*, vol. 124, pp. 570–590, 2023.

[28] N. Chaukura, E. Murimba, and W. Gwenzi, "Synthesis, characterisation and methyl orange adsorption capacity of ferric oxide–biochar nano-composites derived from pulp and paper sludge," *Applied Water Science*, vol. 7, p. 2175–2186, 2016.

[29] M. Eumann and C. Schaeberle, "Chapter 5 - Water," in *Brewing Materials and Processes* (Charles W. Bamforth, ed.), pp. 97–111, San Diego: Academic Press, 2016.

[30] H. Tahir and M. Saad, "Chapter 3 - Using dyes to evaluate the photocatalytic activity,"

in *Photocatalysis: Fundamental Processes and Applications* (Mehrorang Ghaedi, ed.), vol. 32 of *Interface Science and Technology*, pp. 125–224, Elsevier, 2021.

[31] J. Han, H.-Y. Zeng, S. Xu, C.-R. Chen, and X.-J. Liu, "Catalytic properties of CuMgAlO catalyst and degradation mechanism in CWPO of methyl orange," *Applied Catalysis A: General*, vol. 527, pp. 72–80, 2016.

[32] A. Galembeck, S. B. Silva, J. A. P. Silva, and J. Del Nero, "Polyphosphate gel/methyl orange supramolecular composites," *Optical Materials*, vol. 24, no. 4, pp. 637–641, 2004.

[33] W. B. Jensen, "Faraday's Laws or Faraday's Law?," *Journal of Chemical Education*, vol. 89, no. 9, pp. 1208–1209, 2012.

[34] G. Cao, *Nanostructures & Nanomaterials: Synthesis, Properties & Applications*. Imperial College Press, 1st ed., 2014.

[35] C. M. Magdalane, G. M. A. Priyadharsini, K. Kaviyarasu, A. I. Jothi, and G. G. Simiyon, "Synthesis and characterization of TiO2 doped cobalt ferrite nanoparticles via microwave method: Investigation of photocatalytic performance of congo red degradation dye," *Surfaces and Interfaces*, vol. 25, p. 101296, 2021.

[36] K. Gelderman, L. Lee, and S. W. Donne, "Flat-Band Potential of a Semiconductor: Using the Mott–Schottky Equation," *Journal of Chemical Education*, vol. 84, no. 4, p. 685, 2007.

[37] J. Bian, L. Xi, J. Li, Z. Xiong, C. Huang, K. M. Lange, J. Tang, M. Shalom, and R.-Q. Zhang, "C=C π Bond Modified Graphitic Carbon Nitride Films for Enhanced Photoelectrochemical Cell Performance," *Chemistry – An Asian Journal*, vol. 12, no. 9, pp. 1005–1012, 2017.

[38] B. G. Pollet and M. Ashokkumar, *Introduction to Ultrasound, Sonochemistry and Sonoelectrochemistry*. Springer, 1st ed., 2019.

[39] H. E. Hansen, F. Seland, S. Sunde, O. S. Burheim, and B. G. Pollet, "Frequency controlled agglomeration of Pt-nanoparticles in sonochemical synthesis," *Ultrasonics Sonochemistry*, vol. 85, p. 105991, 2022.

[40] R. Holze, *Experimental Electrochemistry. A Laboratory Textbook*. Wiley-VCH, 1st ed.,

2009.

[41] R. Nikzad-Langerodi, W. Zellinger, S. Saminger-Platz, and B. A. Moser, "Domain adaptation for regression under Beer–Lambert's law," *Knowledge-Based Systems*, vol. 210, p. 106447, 2020.

[42] H. y. Jung, M. j. Chae, J. h. Park, Y. i. Song, J. c. Ro, and S. j. Suh, "Effects of Platinum Group Metals on MoS2 Nanosheets for a High-Performance Hydrogen Evolution Reaction Catalyst," *ACS Applied Energy Materials*, vol. 4, no. 10, pp. 10748–10755, 2021.

[43] S. Gottesfeld, "Faradaic Processes at the Ir/Ir Oxide Electrode," *Journal of The Electrochemical Society*, vol. 127, p. 1922, sep 1980.

[44] A. Slami and N. Benramdane, "Manual Method for Measuring The External Quantum Efficiency for solar cells," *E3S Web of Conferences*, vol. 229, p. 01005, 2021.

[45] K. Giribabu, Y. Haldorai, M. Rethinasabapathy, S.-C. Jang, R. Suresh, W.-S. Cho, Y.-K. Han, C. Roh, Y. S. Huh, and V. Narayanan, "Glassy carbon electrode modified with poly(methyl orange) as an electrochemical platform for the determination of 4-nitrophenol at nanomolar levels," *Current Applied Physics*, vol. 17, no. 8, pp. 1114–1119, 2017.

[46] S. C. Yan, Z. S. Li, and Z. G. Zou, "Photodegradation of Rhodamine B and Methyl Orange over Boron-Doped g-C3N4 under Visible Light Irradiation," *Langmuir*, vol. 26, no. 6, pp. 3894–3901, 2010.

[47] G. M. Stephen, I. Naumov, S. Tyagi, O. A. Vail, J. E. DeMell, M. Dreyer, R. E. Butera, A. T. Hanbicki, P. J. Taylor, I. Mayergoyz, P. Dev, and A. L. Friedman, "Effect of Sn Doping on Surface States of Bi2Se3 Thin Films," *The Journal of Physical Chemistry C*, vol. 124, no. 49, pp. 27082–27088, 2020.

[48] Y. Niu, Y. Zhou, P. Niu, H. Shen, and Y. Ma, "Effects of Ti Doping on Hematite Photoanodes: More Surface States," *Journal of nanoscience and nanotechnology*, vol. 19, no. 6, p. 3437–3446, 2019.

[49] K. D. Log, "Band gap alterations of graphitic carbon nitride for photoelectrochemical

water splitting," *Unpublished*, 2022.

[50] M. Nguyen Van, O. L. T. Mai, C. Pham Do, H. Lam Thi, C. Pham Manh, H. Nguyen Manh, D. Pham Thi, and B. Do Danh, "Fe-Doped g-C3N4: High-Performance Photocatalysts in Rhodamine B Decomposition," *Polymers*, vol. 12, no. 9, 2020.

A Mott Schottky analysis

In addition to a frequency of 1 kHz, Mott Schottky analyses for frequencies equal to 1.7 and 3 kHz were also performed to investigate the effect of frequency on the flat band potential. The resulting curves for pristine and boron-doped g-C_3N_4 at frequencies of 1.7 and 3 kHz are given in Figures A.1 and A.2, respectively. In general, a higher frequency led to a more cathodic flat band potential.

A summary of the flat band potentials and the corresponding VB for the samples at all frequencies are given in Tables A.1, A.2, and A.3. In these calculations, it is assumed that the flat band potential, and thus the Fermi level, is approximately equal to the CB. Thus, the VB can be found by adding the value of the band gap to the flat band potential.

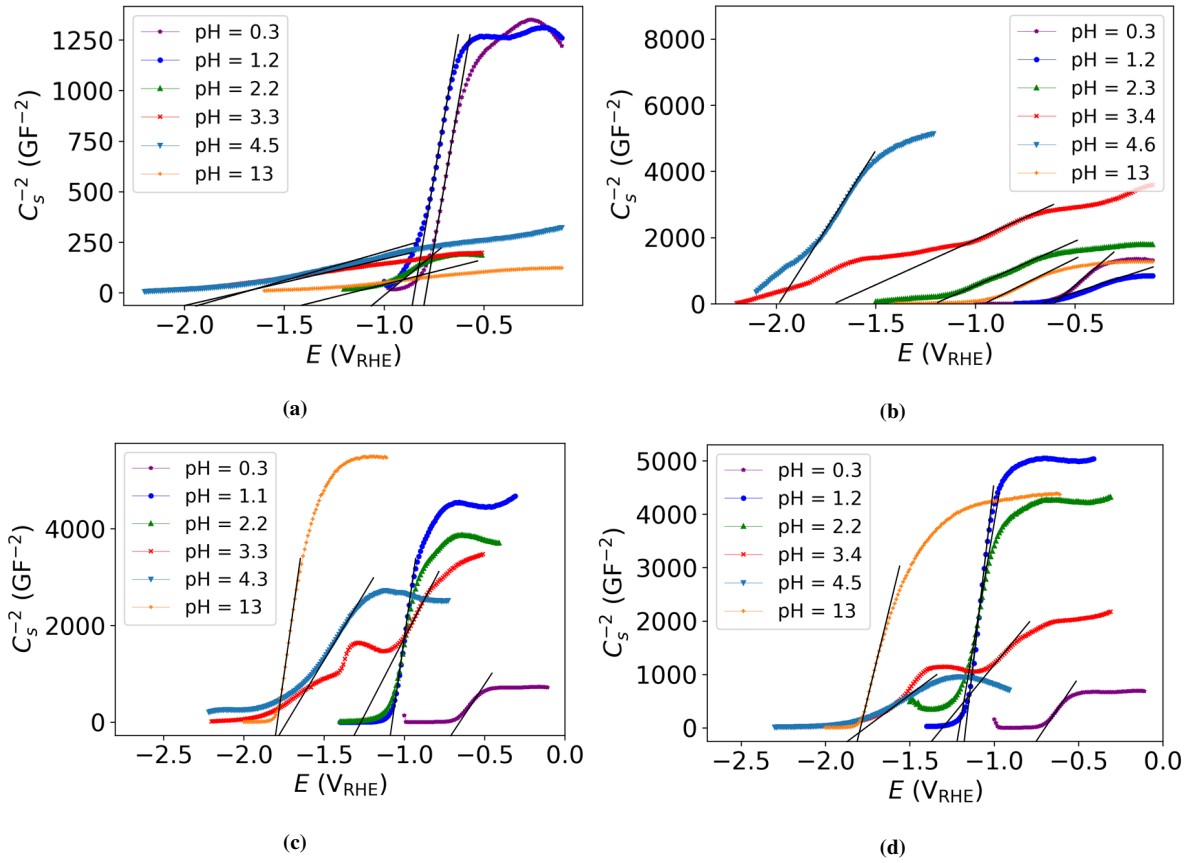

Figure A.1: Mott Schottky plots of a) pristine g-C_3N_4, b) B300Air, c) B500Air and d) B500Argon at 1.7 kHz and different pH. In these sample names, B denotes boron-doped, 300 and 500 denote the synthesis temperature, and Air and Argon denote the atmosphere used in the doping synthesis. The potential measurements ranged from -2.3 V_{RHE} to -0.1 V_{RHE} with a potential step of 10 mV. The extrapolations of the linear parts of the curves are also demonstrated.

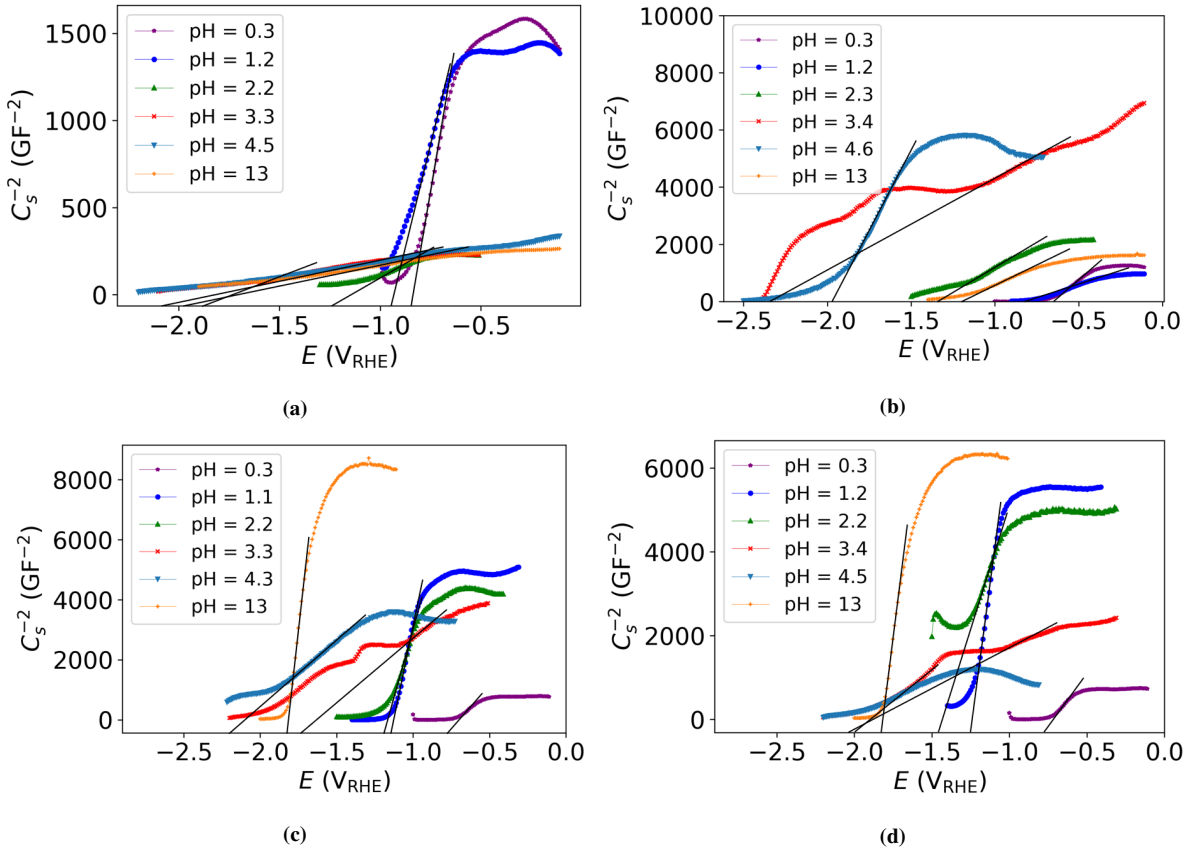

Figure A.2: Mott Schottky plots of a) pristine g-C_3N_4, b) B300Air, c) B500Air and d) B500Argon at 3 kHz and different pH. In these sample names, B denotes boron-doped, 300 and 500 denote the synthesis temperature, and Air and Argon denote the atmosphere used in the doping synthesis. The potential measurements ranged from -2.5 V_{RHE} to -0.1 V_{RHE} with a potential step of 10 mV. The extrapolations of the linear parts of the curves are also demonstrated.

Table A.1: Measured flat band potentials and corresponding valence bands for pristine and boron-doped g-C_3N_4 at a frequency of 1 kHz and different pH. For the sample names in the table, B denotes boron-doped, 300 and 500 denote the synthesis temperature, and Air and Argon denote the atmosphere used in the doping synthesis. The flat band potential is assumed to correspond to the conduction band and the valence band is thus calculated by adding the energy of the band gap.

	pH	Flat band potential (V_{RHE})	E_g (eV)	Valence band (V_{RHE})
Pristine g-C_3N_4	0.3	-0.76	3.10	2.34
	1.2	-0.80	3.10	2.30
	2.2	-0.96	3.10	2.14
	3.3	-1.44	3.10	1.66
	4.5	-1.69	3.10	1.41
	13	-1.08	3.10	2.02
B300Air	0.3	-0.54	2.38	1.84
	1.2	-0.53	2.38	1.85
	2.3	-0.98	2.38	1.40
	3.4	-1.34	2.38	1.04
	4.6	-1.86	2.38	0.52
	13	-0.92	2.38	1.46
B500Air	0.3	-0.65	1.73	1.08
	1.1	-1.01	1.73	0.72
	2.2	-1.02	1.73	0.71
	3.3	-1.07	1.73	0.66
	4.3	-1.68	1.73	0.05
	13	-1.76	1.73	-0.03
B500Argon	0.3	-0.74	1.59	0.85
	1.2	-1.09	1.59	0.50
	2.2	-1.05	1.59	0.54
	3.4	-1.09	1.59	0.50
	4.5	-1.64	1.59	-0.05
	13	-1.58	1.59	0.01

Table A.2: Measured flat band potentials and corresponding valence bands for pristine and boron-doped g-C_3N_4 at a frequency of 1.7 kHz and different pH. For the sample names in the table, B denotes boron-doped, 300 and 500 denote the synthesis temperature, and Air and Argon denote the atmosphere used in the doping synthesis. The flat band potential is assumed to correspond to the conduction band and the valence band is thus calculated by adding the energy of the band gap.

	pH	Flat band potential (V_{RHE})	E_g (eV)	Valence band (V_{RHE})
Pristine g-C_3N_4	0.3	-0.79	3.10	2.31
	1.2	-0.85	3.10	2.25
	2.2	-1.05	3.10	2.05
	3.3	-2.00	3.10	1.10
	4.5	-1.81	3.10	1.29
	13	-1.42	3.10	1.68
B300Air	0.3	-0.59	2.38	1.79
	1.2	-0.61	2.38	1.77
	2.3	-1.22	2.38	1.16
	3.4	-1.67	2.38	0.71
	4.6	-1.97	2.38	0.41
	13	-0.94	2.38	1.44
B500Air	0.3	-0.68	1.73	1.05
	1.1	-1.07	1.73	0.66
	2.2	-1.09	1.73	0.64
	3.3	-1.30	1.73	0.43
	4.3	-1.77	1.73	-0.04
	13	-1.79	1.73	-0.06
B500Argon	0.3	-0.71	1.59	0.88
	1.2	-1.16	1.59	0.43
	2.2	-1.22	1.59	0.37
	3.4	-1.42	1.59	0.17
	4.5	-1.83	1.59	-0.24
	13	-1.80	1.59	-0.21

Table A.3: Measured flat band potentials and corresponding valence bands for pristine and boron-doped g-C_3N_4 at a frequency of 3 kHz and different pH. For the sample names in the table, B denotes boron-doped, 300 and 500 denote the synthesis temperature, and Air and Argon denote the atmosphere used in the doping synthesis. The flat band potential is assumed to correspond to the conduction band and the valence band is thus calculated by adding the energy of the band gap.

	pH	Flat band potential (V_{RHE})	E_g (eV)	Valence band (V_{RHE})
Pristine g-C_3N_4	0.3	-0.85	3.10	2.25
	1.2	-0.94	3.10	2.16
	2.2	-1.23	3.10	1.87
	3.3	-1.82	3.10	1.28
	4.5	-2.05	3.10	1.05
	13	-1.92	3.10	1.18
B300Air	0.3	-0.66	2.38	1.72
	1.2	-0.76	2.38	1.62
	2.3	-1.33	2.38	1.05
	3.4	-2.36	2.38	0.02
	4.6	-1.95	2.38	0.43
	13	-1.22	2.38	1.16
B500Air	0.3	-0.72	1.73	1.01
	1.1	-1.13	1.73	0.60
	2.2	-1.17	1.73	0.56
	3.3	-1.71	1.73	0.02
	4.3	-2.12	1.73	-0.39
	13	-1.84	1.73	-0.11
B500Argon	0.3	-0.73	1.59	0.86
	1.2	-1.25	1.59	0.34
	2.2	-1.46	1.59	0.13
	3.4	-2.03	1.59	-0.44
	4.5	-2.00	1.59	-0.41
	13	-1.81	1.59	-0.22

An overview of how the flat band potentials generally move with increasing pH in the acidic region is given in Figure A.3 for the respective frequencies. Here, the flat band potentials generally move towards more cathodic potentials with increasing pH for all samples.

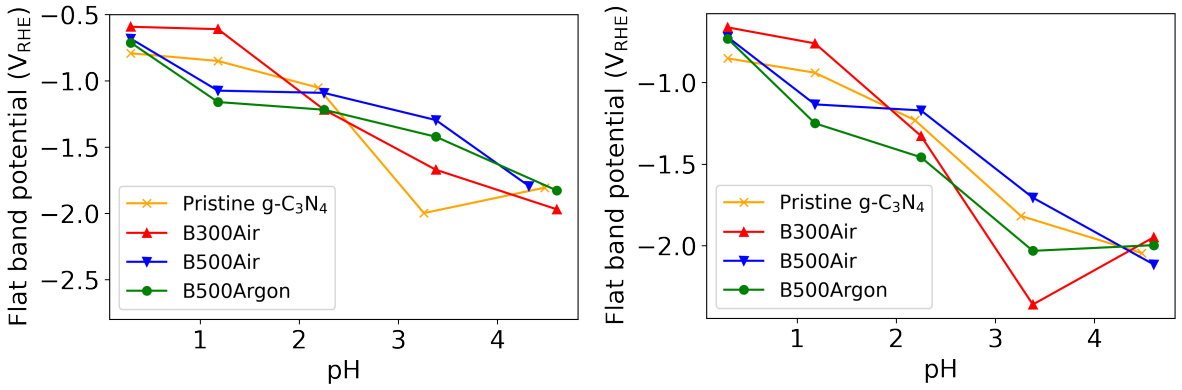

Figure A.3: Measured flat band potentials vs. acidic pH for pristine g-C_3N_4 (×), B300Air (△), B500Air (▽) and B500Argon (◯) at a frequency of a) 1.7 kHz and b) 3 kHz. In these sample names, B denotes boron-doped, 300 and 500 denote the synthesis temperature, and Air and Argon denote the atmosphere used in the doping synthesis. The flat band potential generally moves towards more cathodic potentials with an increasing pH.

For 1 kHz, the linear fits obtained for the flat band potentials as a function of pH are given in Figure A.4 for pristine and boron-doped g-C_3N_4. The obtained slopes are -241 $mVpH^{-1}$, -323 $mVpH^{-1}$, -200 $mVpH^{-1}$, and -170 $mVpH^{-1}$ for pristine g-C_3N_4, B300Air, B500Air, and B500Argon, respectively, with corresponding R^2 values of 0.936, 0.958, 0.777, and 0.768 for the linear fit. This indicates a varying degree of linearity for the flat band potential vs. pH for the different samples. A summary of the slopes is given in Table 4.1.

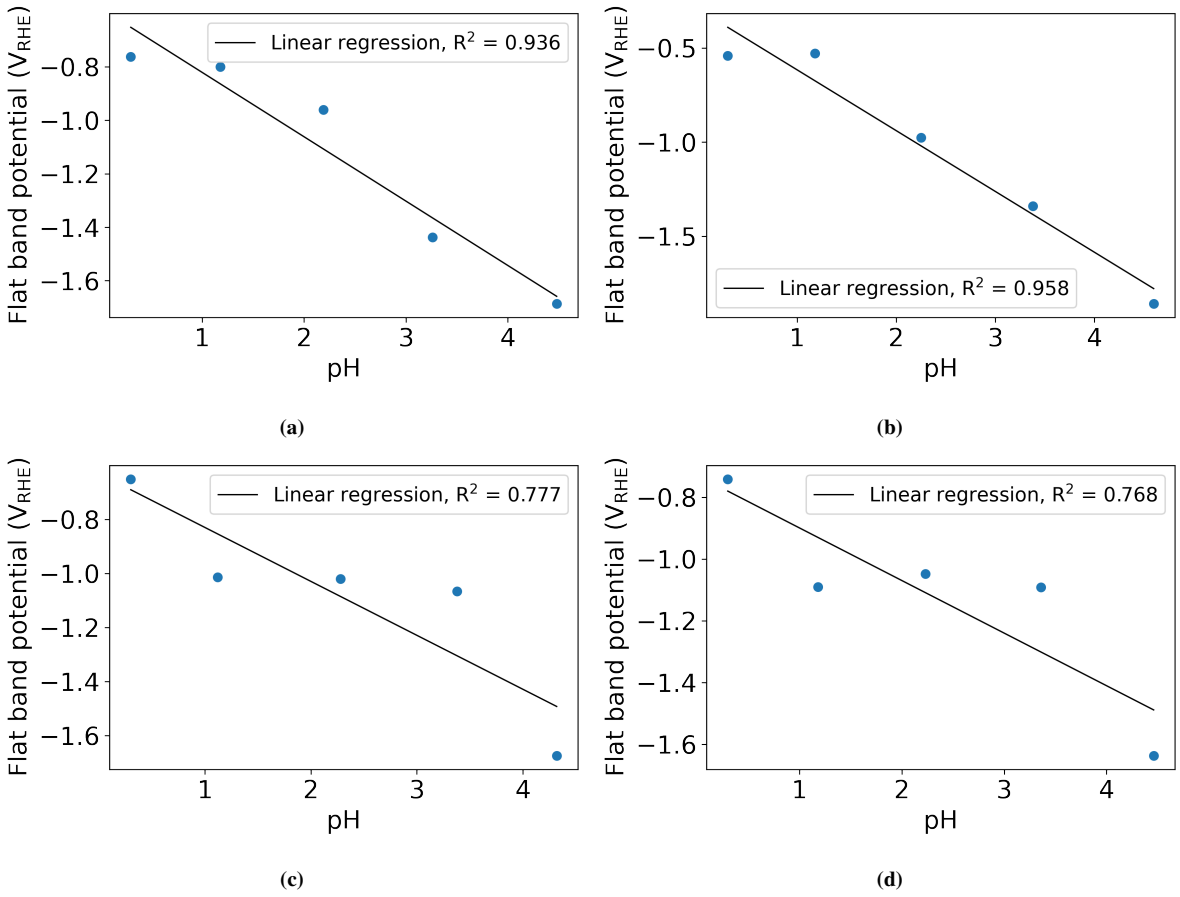

Figure A.4: Flat band potential as a function of pH for a) pristine g-C_3N_4, b) B300Air, c) B500Air, and d) B500Argon at a frequency of 1 kHz. In these sample names, B denotes boron-doped, 300 and 500 denote the synthesis temperature, and Air and Argon denote the atmosphere used in the doping synthesis. The linearly fitted curves with corresponding R^2 values are given.

For 1.7 kHz, the obtained flat band potentials as a function of pH are given in Figure A.5 for pristine and boron-doped g-C_3N_4. The obtained slopes are -304 $mVpH^{-1}$, -355 $mVpH^{-1}$, -237 $mVpH^{-1}$, and -230 $mVpH^{-1}$ for pristine g-C_3N_4, B300Air, B500Air, and B500Argon, respectively, with corresponding R^2 values of 0.796, 0.961, 0.895, and 0.936 for the linear fit. This indicates a varying degree of linearity for the flat band potential vs. pH for the different samples. A summary of the slopes is given in Table A.4.

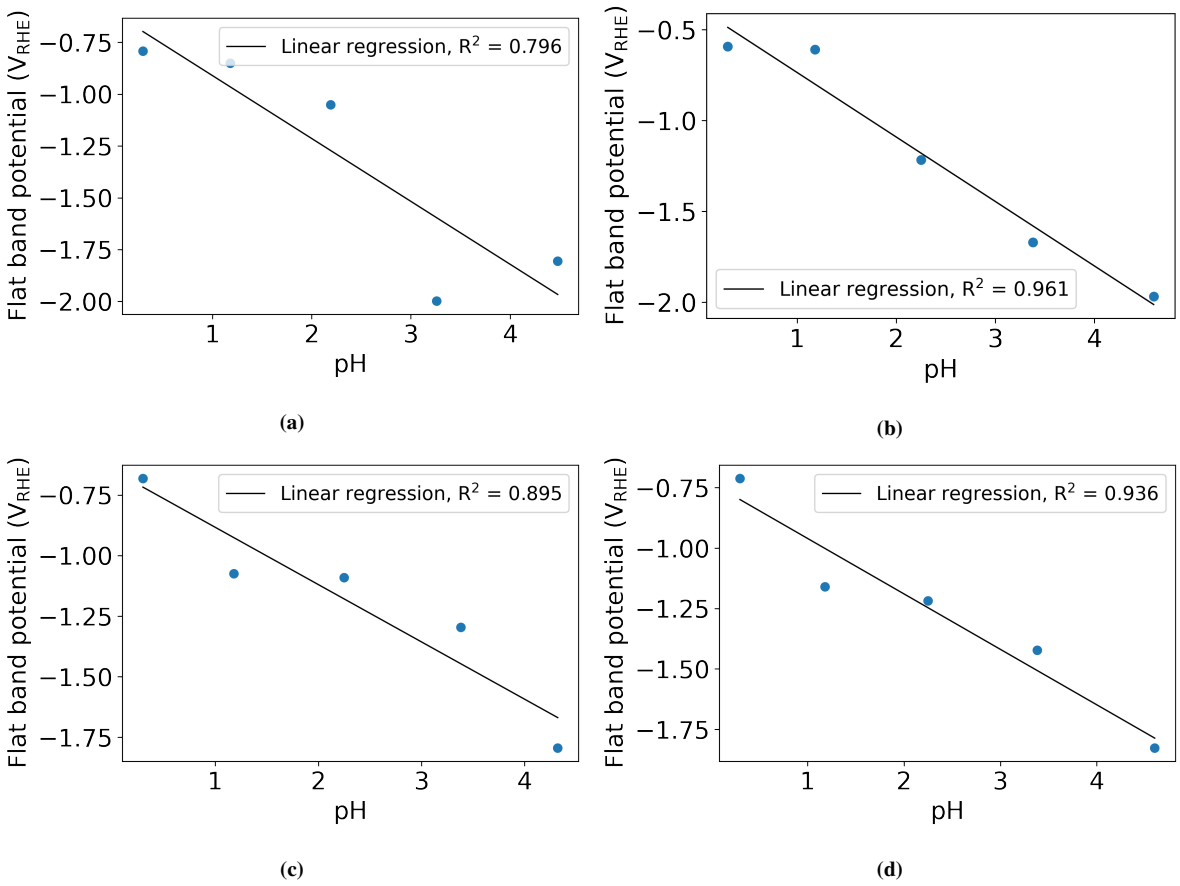

Figure A.5: Flat band potential as a function of pH for a) pristine g-C_3N_4, b) B300Air, c) B500Air, and d) B500Argon at a frequency of 1.7 kHz. In these sample names, B denotes boron-doped, 300 and 500 denote the synthesis temperature, and Air and Argon denote the atmosphere used in the doping synthesis. The linearly fitted curves with corresponding R^2 values are given.

Table A.4: Measured flat band potential as a function of acidic pH at a frequency of 1.7 kHz for pristine and boron-doped g-C_3N_4. For the sample names in the table, B denotes boron-doped, 300 and 500 denote the synthesis temperature, and Air and Argon denote the atmosphere used in the doping synthesis.

	Flat band potential vs. pH ($mVpH^{-1}$)
Pristine g-C_3N_4	-304
B300Air	-355
B500Air	-237
B500Argon	-230

For 3 kHz, the obtained flat band potentials as a function of pH are given in Figure A.6 for pristine and boron-doped g-C_3N_4. The obtained slopes are -314 $mVpH^{-1}$, -384 $mVpH^{-1}$, -312 $mVpH^{-1}$, and -302 $mVpH^{-1}$ for pristine g-C_3N_4, B300Air, B500Air, and B500Argon, respectively, with corresponding R^2 values of 0.956, 0.790, 0.960, and 0.903 for the linear fit. This indicates a varying degree of linearity for the flat band potential vs. pH for the different samples. A summary of the slopes is given in Table A.5.

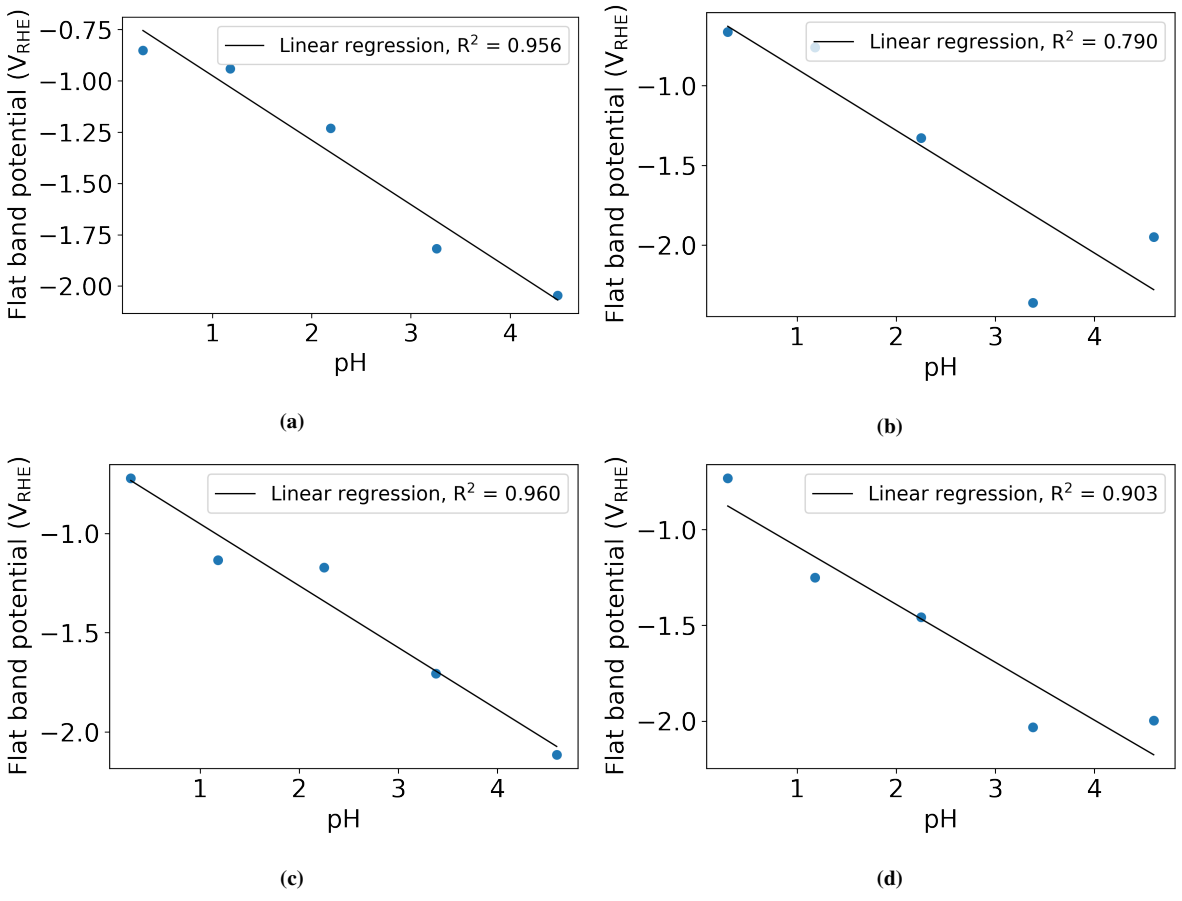

Figure A.6: Flat band potential as a function of pH for a) pristine g-C_3N_4, b) B300Air, c) B500Air, and d) B500Argon at a frequency of 3 kHz. In these sample names, B denotes boron-doped, 300 and 500 denote the synthesis temperature, and Air and Argon denote the atmosphere used in the doping synthesis. The linearly fitted curves with corresponding R^2 values are given.

Table A.5: Measured flat band potential as a function of acidic pH at a frequency of 3 kHz for pristine and boron-doped g-C_3N_4. For the sample names in the table, B denotes boron-doped, 300 and 500 denote the synthesis temperature, and Air and Argon denote the atmosphere used in the doping synthesis.

	Flat band potential vs. pH ($mVpH^{-1}$)
Pristine g-C_3N_4	-314
B300Air	-384
B500Air	-312
B500Argon	-302

B Band gap visualizations

Visualizations of the band gaps can be made based on the Mott Schottky results given in section 4.3. These are presented in Figures B.1, B.2, B.3, and B.4 for pristine g-C_3N_4, B300Air, B500Air, B500Argon, respectively. As can be seen in these figures, the cathodic change in flat band potential occurs for all samples at an increasing pH in the acidic region. For pristine g-C_3N_4 and B300Air, the flat band potential moves to more anodic values for a pH of 13. For B500Air and B500Argon, the flat band potential at a pH of 13 is located approximately at the same value as that for a pH of 4.5. A jump in the flat band potential for a pH of approximately 4.5 is also observed for all samples.

These band gap visualizations are more accurate for the boron-doped samples than for pristine g-C_3N_4, due to the approximation of the Fermi level being located at or near the CB for these samples being more valid. For pristine g-C_3N_4, the VB proved to be located at much more cathodic potentials than that obtained from the Mott Schottky analysis when performing LSV of the $Fe(CN)_6^{3-/4-}$ redox couple. Thus, the approximation of the flat band potential, and thus the Fermi level, being located near the CB for pristine g-C_3N_4 is not valid. As a result, the band edges of pristine g-C_3N_4, and perhaps also B300Air due to the lower amount of dopant concentration compared to B500Air and B500Argon, are likely located at more cathodic potentials than those given in the figures below. The most anodic redox potential for the $Fe(CN)_6^{3-/4-}$ couple, obtained at a pH of 4.4, is presented along with the oxidation potential of MO in the figures.

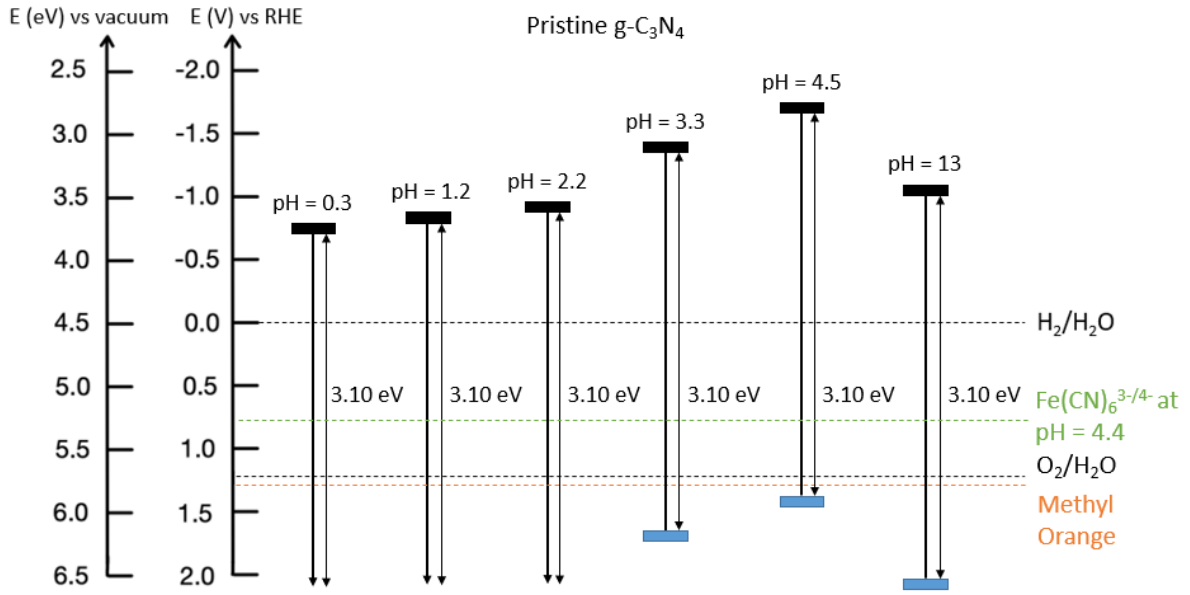

Figure B.1: Band edges of pristine g-C_3N_4 at 1 kHz and different pH, based on the Mott Schottky results. The redox potential of the $Fe(CN)_6^{3-/4-}$ couple at a pH of 4.4 and the oxidation potential of methyl orange is given as the colored dotted lines in the figure.

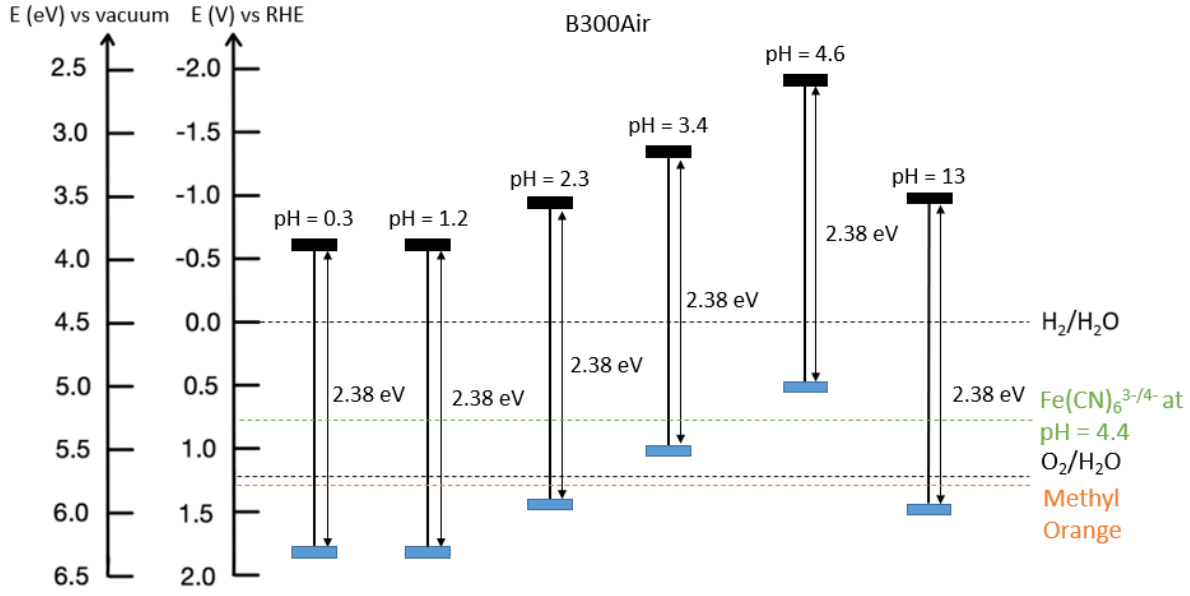

Figure B.2: Band edges of B300Air at 1 kHz and different pH, based on the Mott Schottky results. In this sample name, B denotes boron-doped, 300 denotes the synthesis temperature, and Air denotes the atmosphere used in the doping synthesis. The redox potential of the $Fe(CN)_6^{3-/4-}$ couple at a pH of 4.4 and the oxidation potential of methyl orange is given as the colored dotted lines in the figure.

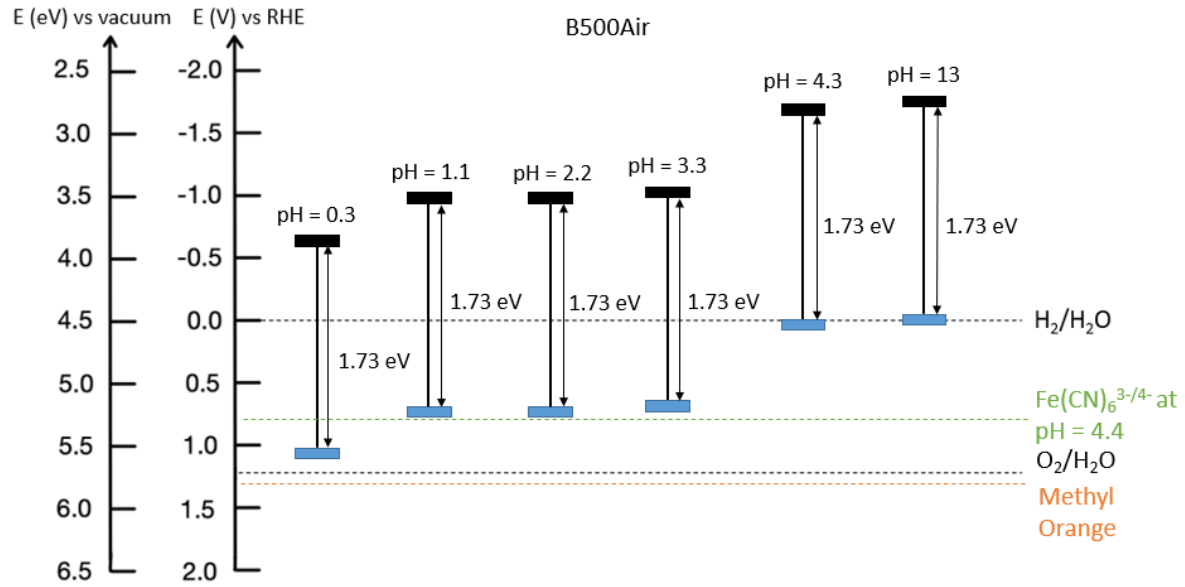

Figure B.3: Band edges of B500Air at 1 kHz and different pH, based on the Mott Schottky results. In this sample name, B denotes boron-doped, 500 denotes the synthesis temperature, and Air denotes the atmosphere used in the doping synthesis. The redox potential of the $Fe(CN)_6^{3-/4-}$ couple at a pH of 4.4 and the oxidation potential of methyl orange is given as the colored dotted lines in the figure.

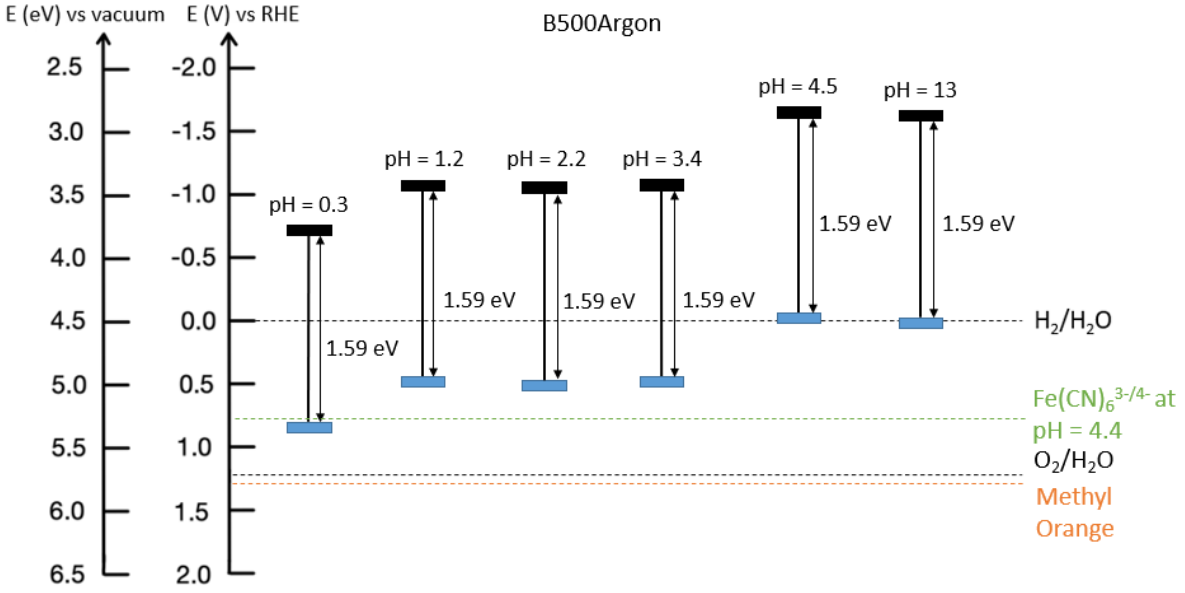

Figure B.4: Band edges of B500Argon at 1 kHz and different pH, based on the Mott Schottky results. In this sample name, B denotes boron-doped, 500 denotes the synthesis temperature, and Argon denotes the atmosphere used in the doping synthesis. The redox potential of the $Fe(CN)_6^{3-/4-}$ couple at a pH of 4.4 and the oxidation potential of methyl orange is given as the colored dotted lines in the figure.

C The Fe(CN)$_6^{3-/4-}$ redox couple

A CV of the Fe(CN)$_6^{3-/4-}$ redox couple at a pH of 4.4 is given in Figure C.1. The voltammogram displays anodic and cathodic limiting currents of 11.7 and -11.2 mA, respectively. The oxidation potential at this pH is about 1.0 V_{RHE} and the reduction potential is 0.55 V_{RHE}.

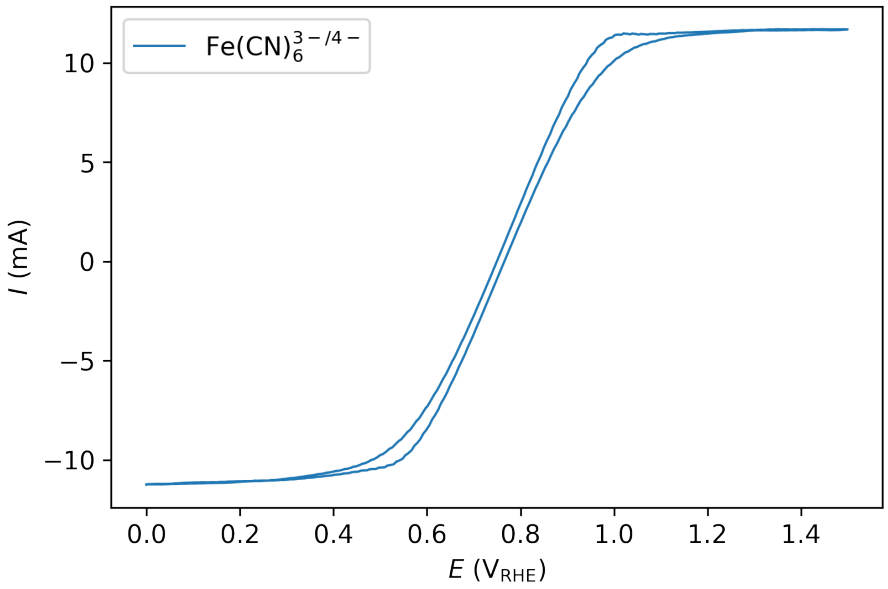

Figure C.1: Cyclic voltammetry of the Fe(CN)$_6^{3-/4-}$ redox couple at a pH of 4.4 from 0 V_{RHE} to 1.5 V_{RHE} at a scan rate of 500 mVs^{-1}, displaying an oxidation peak at around 1.0 V_{RHE}, a reduction peak at around 0.55 V_{RHE}, and limiting currents equal to 11.7 and -11.3 mA.

As the resulting band edges obtained from the Mott Schottky analysis and the LSV of the Fe(CN)$_6^{3-/4-}$ redox couple differed, a visualization of the difference is given in Figure C.2 for pristine g-C_3N_4 and B500Argon at a pH of 2.2. The Mott Schottky analysis gave more anodic band edges than the LSV of the Fe(CN)$_6^{3-/4-}$ redox couple for pristine g-C_3N_4, but more cathodic band edges for B500Argon.

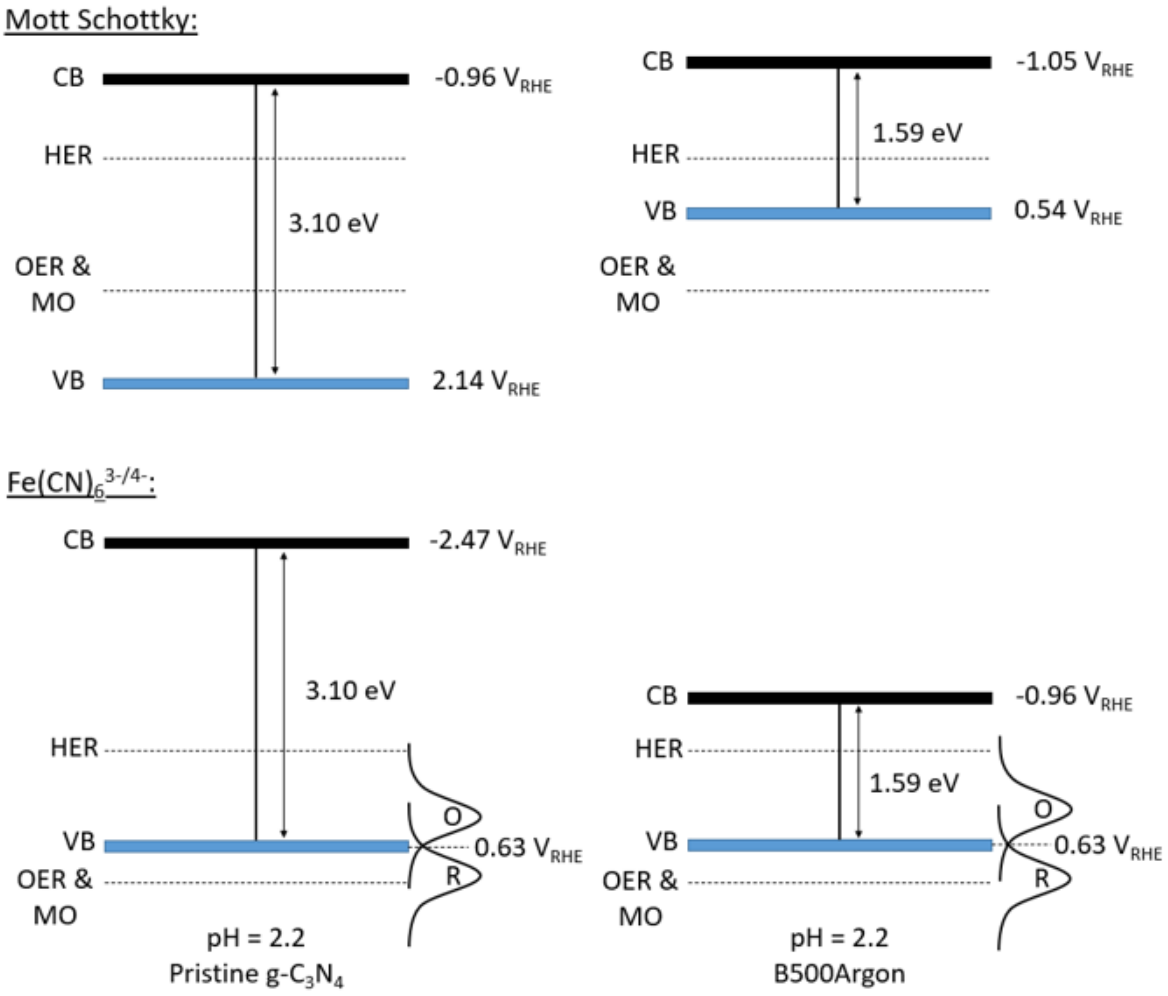

Figure C.2: Comparison of the results from the Mott Schottky analysis and the Fe(CN)$_6^{3-/4-}$ redox couple at a pH of 2.2 for pristine g-C_3N_4 (left) and B500Argon (right). Here, B denotes boron-doped, 500 denotes the synthesis temperature, and Argon denotes the atmosphere used in the doping synthesis. The Mott Schottky results place the valence bands at 2.14 V_{RHE} and 0.54 V_{RHE} for pristine g-C_3N_4 and B500Argon, respectively. The results from the linear sweep voltammetry of the Fe(CN)$_6^{3-/4-}$ redox couple places the valence band at 0.63 V_{RHE} for both samples. In this figure, *O* denotes the oxidized form of Fe(CN)$_6^{3-/4-}$ and *R* denotes the reduced form of Fe(CN)$_6^{3-/4-}$.

D Methyl orange and rhodamine B

Obtained CVs of RhB at different pH are given in Figure D.1. No visible oxidation peaks are observed in this potential region, resulting in MO being more interesting to investigate further than RhB.

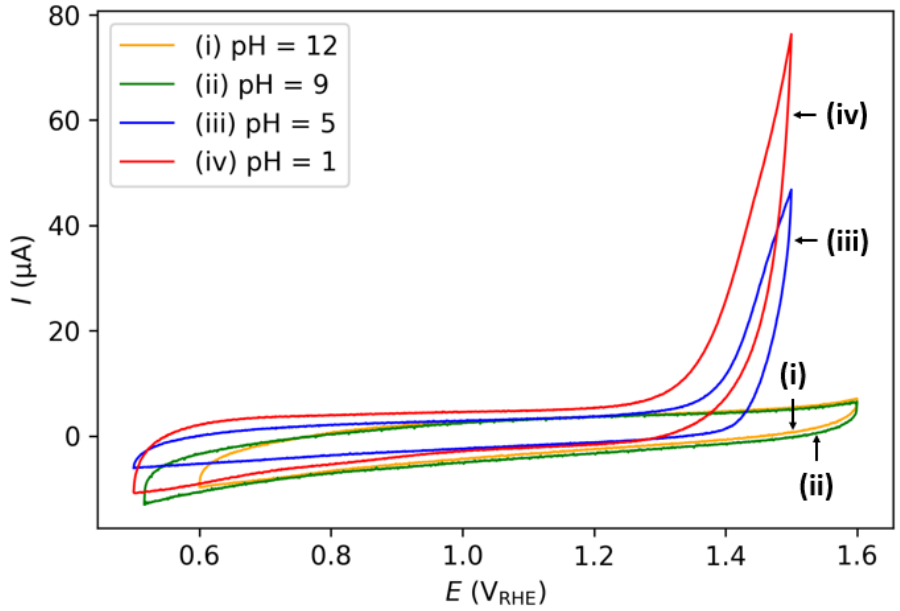

Figure D.1: Obtained cyclic voltammetry for 0.21 mM rhodamine B in 0.1 M Na_2SO_4 at different pH, from 0.5 V_{RHE} to 1.6 V_{RHE}, at a scan rate of 500 mVs^{-1}. No visible oxidation or reduction peaks are observed in this potential range.

As MO was chosen to investigate further instead of RhB, a more thorough examination of the pH dependence of MO's oxidation potential was performed, for which the CVs are given in Figure D.2. These oxidation peaks were used to obtain the dependence given in Figure 4.10b for the acidic form of MO.

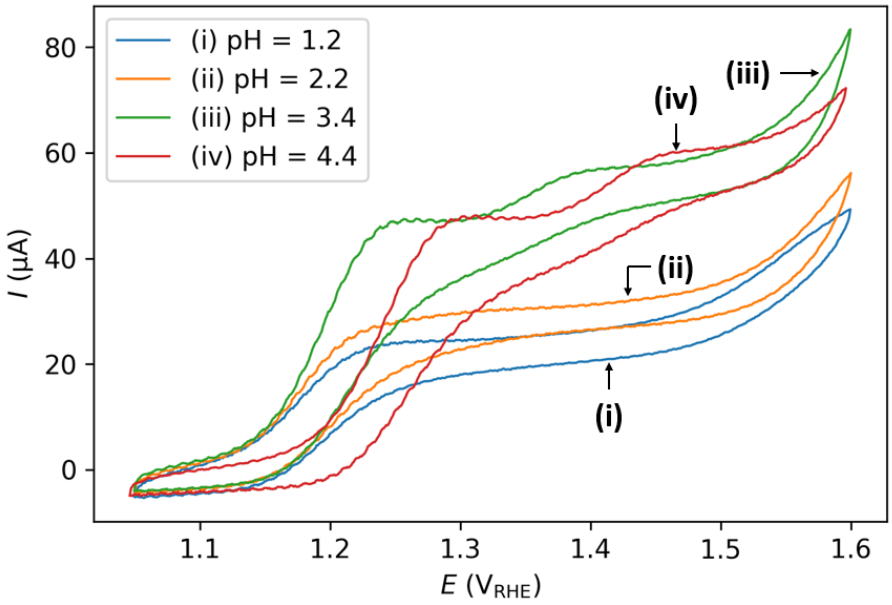

Figure D.2: Obtained cyclic voltammetry displaying oxidation potentials in acidic solutions for 0.31 mM methyl orange in 0.1 M Na_2SO_4 from 1.05 V_{RHE} to 1.6 V_{RHE} with a scan rate of 500 mVs^{-1}. These oxidation peaks were used to obtain the pH dependence displayed in Figure 4.10b.

Using UV-visible spectroscopy, calibration curves of MO and RhB were obtained. These are given in Figure D.3. For MO at a pH above 4.3, the main absorption peak is situated at around 464 nm, whilst for RhB the main absorption peak is situated at around 507 nm. A decrease in absorbance with decreasing concentration is observed for both MO and RhB. Only MO was interesting to use as a target reaction for the photocatalytic efficiency of pristine and boron-doped g-C_3N_4, meaning that only the absorbances of MO were used in this study.

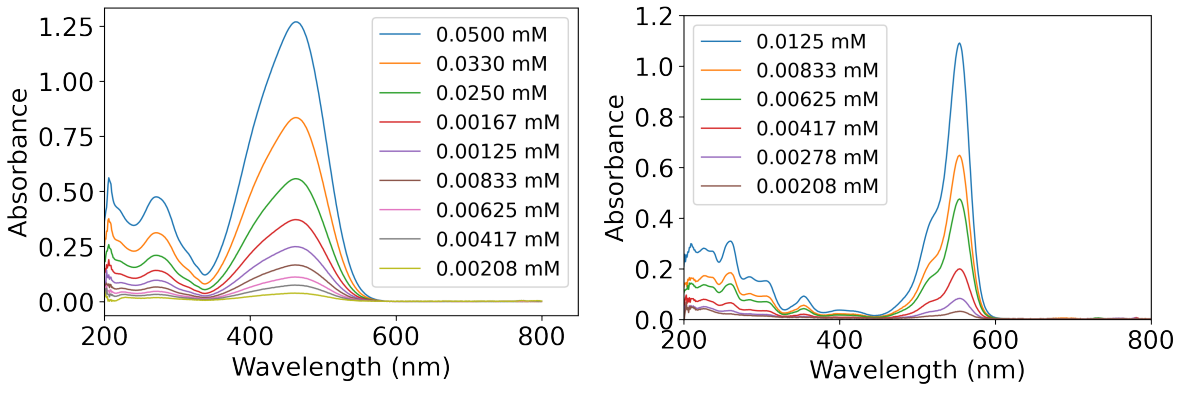

Figure D.3: Calibration curves of concentration vs. absorption peak for a) methyl orange and b) rhodamine B. The curves were measured from 800 nm to 200 nm with a bandwidth of 1 nm.

A plot of measured absorption as a function of the concentration of MO was used to verify a linear relationship between them. The resulting plot is given in Figure D.4, where the linear fit has an R^2 value of 0.996, indicating a strong linear relationship between measured absorption and concentration. Thus, the reduction in absorption peak for MO after illumination can be used to calculate the amount of reduced MO concentration.

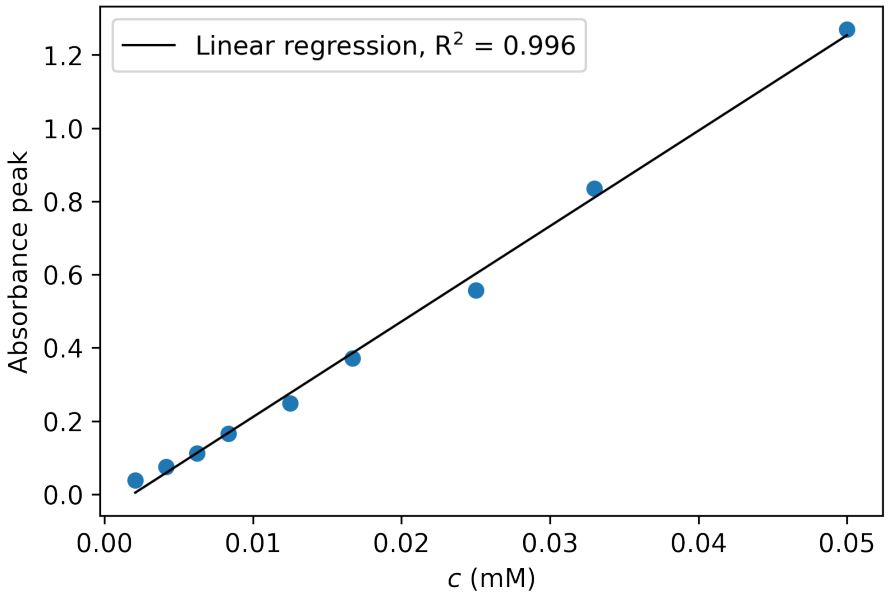

Figure D.4: Measured absorption as a function of the concentration of methyl orange. There is a clear linear relationship as the R^2 value is equal to 0.996.

E Deposition of platinum

UV-visible spectroscopy of the platinum solution was performed during the sonochemical synthesis to ensure a sufficient reduction of the platinum precursor to metallic nanoparticles. These are given in Figure E.1 for pristine g-C_3N_4, B300Air, B500Air, and B500Argon. The absorption peaks located at 495 nm and 345 nm, corresponding to PtI_6^{2-} and PtI_4^{2-}, respectively, are significantly reduced.

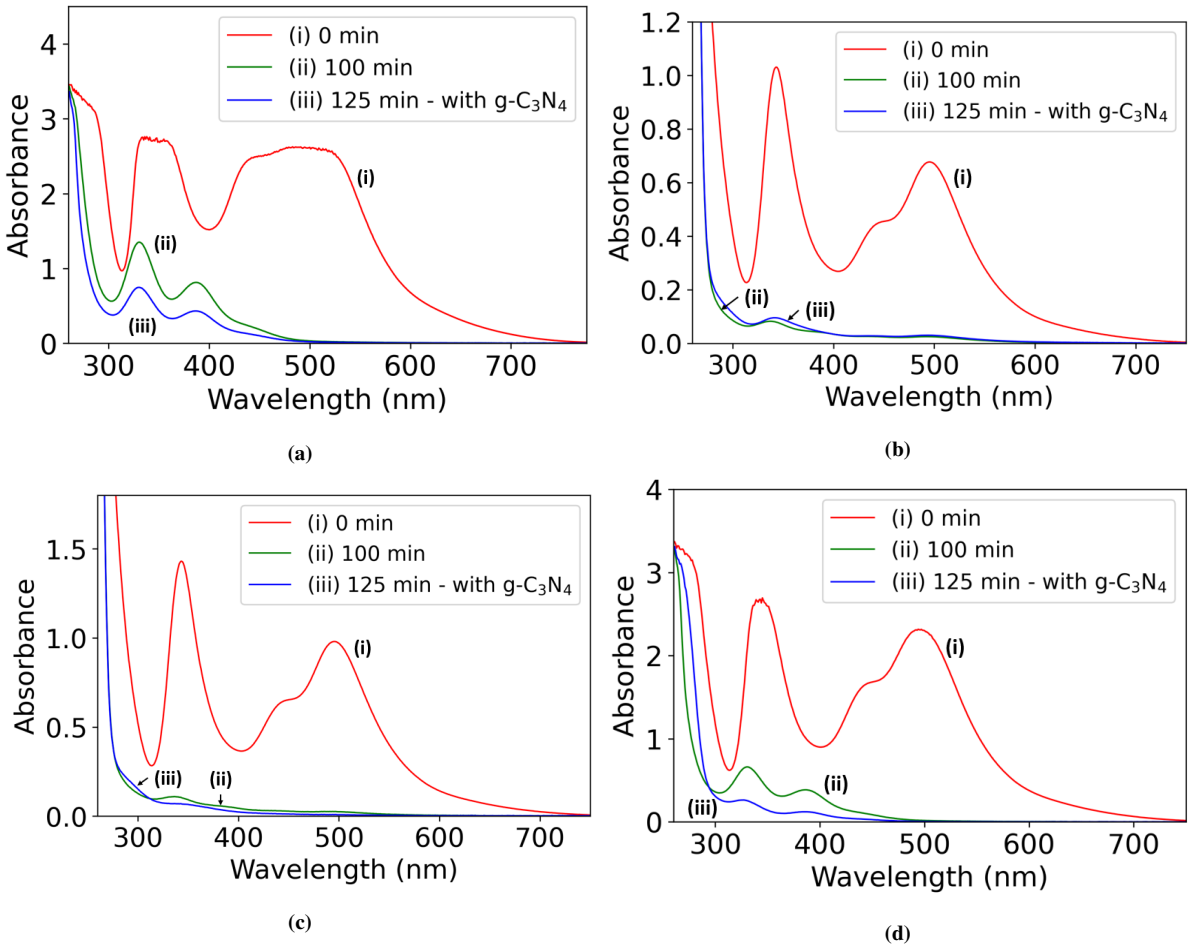

Figure E.1: UV-visible spectroscopy of the sonochemical platinum deposition on a) pristine g-C_3N_4, b) B300Air, c) B500Air and d) B500Argon. In these sample names, B denotes boron-doped, 300 and 500 denote the synthesis temperature, and Air and Argon denote the atmosphere used in the doping synthesis. After 100 minutes, the boron-doped g-C_3N_4 powder was added and sonicated for an additional 25 minutes.

A visible way to confirm that the platinum precursor had been sufficiently reduced to metallic nanoparticles was the change in color of the solution when mixed with KI. This is illustrated in Figure E.2, where the bright red color disappeared after 100 minutes, and turned completely

blank after 125 minutes. Additionally, the platinum solution subject to sonication, without mixing with KI, turned more and more black as metallic nanoparticles were produced.

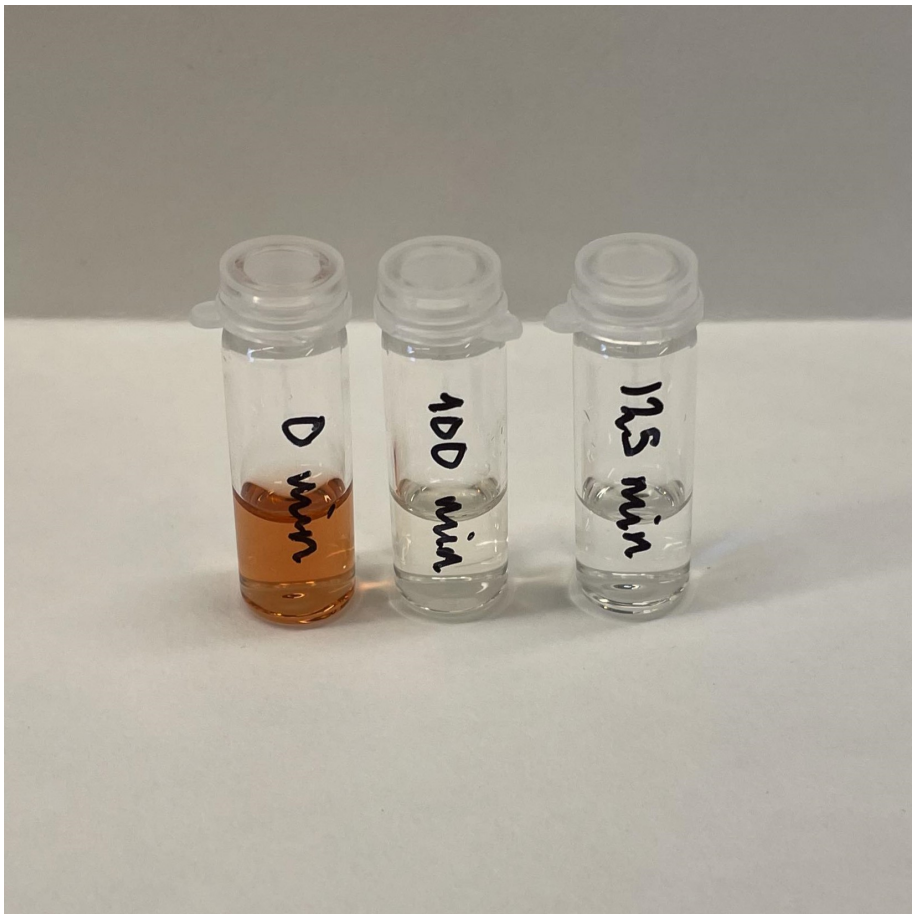

Figure E.2: Visible indication of Pt^{4+} reduction to metallic nanoparticles after 100 and 125 minutes. The red start solution lost its color completely after 125 minutes.

Furthermore, EDS was performed on the boron-doped samples to confirm the presence of platinum. The obtained spectra are given in Figures E.3, E.4 and E.5, where a platinum peak is observed for all samples.

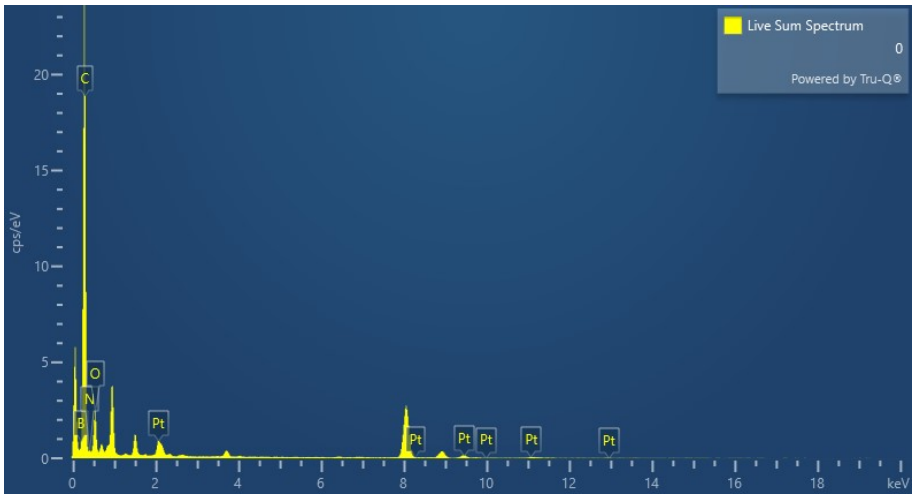

Figure E.3: Obtained spectrum for energy-dispersive X-ray spectroscopy of B300Air. In this sample name, B denotes boron-doped, 300 denotes the synthesis temperature, and Air denotes the atmosphere used in the doping synthesis. Platinum was detected in the sample.

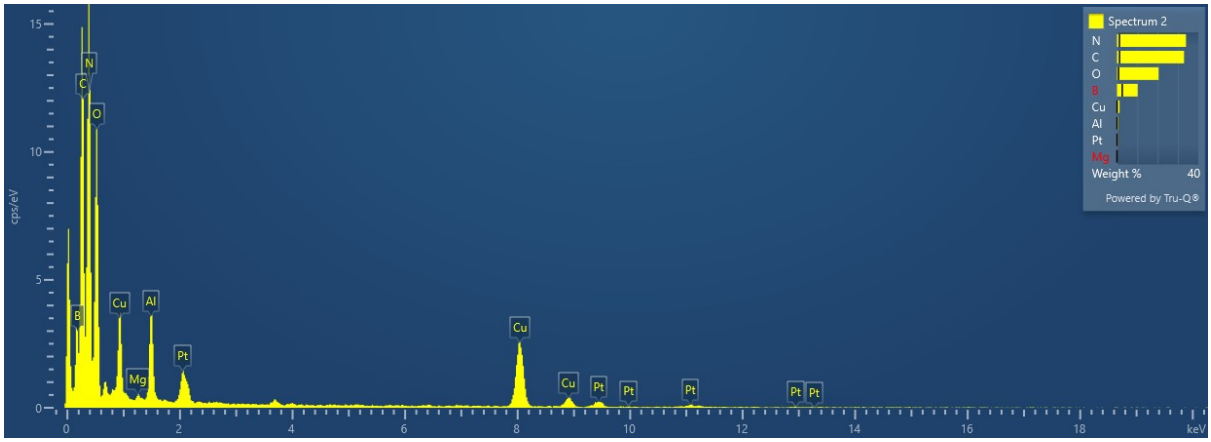

Figure E.4: Obtained spectrum for energy-dispersive X-ray spectroscopy of B500Air. In this sample name, B denotes boron-doped, 500 denotes the synthesis temperature, and Air denotes the atmosphere used in the doping synthesis. Platinum was detected in the sample.

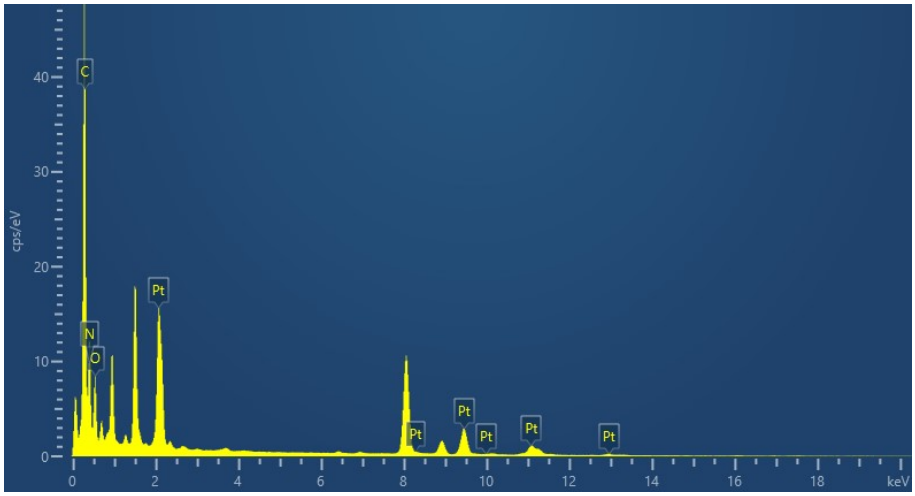

Figure E.5: Obtained spectrum for energy-dispersive X-ray spectroscopy of B500Argon. In this sample name, B denotes boron-doped, 500 denotes the synthesis temperature, and Argon denotes the atmosphere used in the doping synthesis. Platinum was detected in the sample.

F Photoelectrochemical tests

The obtained absorption spectra of the MO solution at different pH values before and after the IPCE tests with pristine and boron-doped g-C_3N_4 are given in Figure F.1. The measured absorption can be used to find the amount of oxidized MO, where a summary of the numerical results are given in Table F.1. The starting concentration of MO and the resulting measured absorbance does not correspond to each other for a pH of 0.3 and 1.0, as the solution had to be diluted 50/50 with DI water before the UV-visible spectroscopy to obtain low enough absorbance values. This was due to the generally higher measured absorbance from the acidic form of MO compared to that of the alkaline form of the dye.

The amount of oxidized MO is calculated from the resulting decrease in absorption peak obtained from UV-visible spectroscopy. The corresponding trends in the amount of oxidized MO are illustrated in Figure 4.13 in section 4.6.

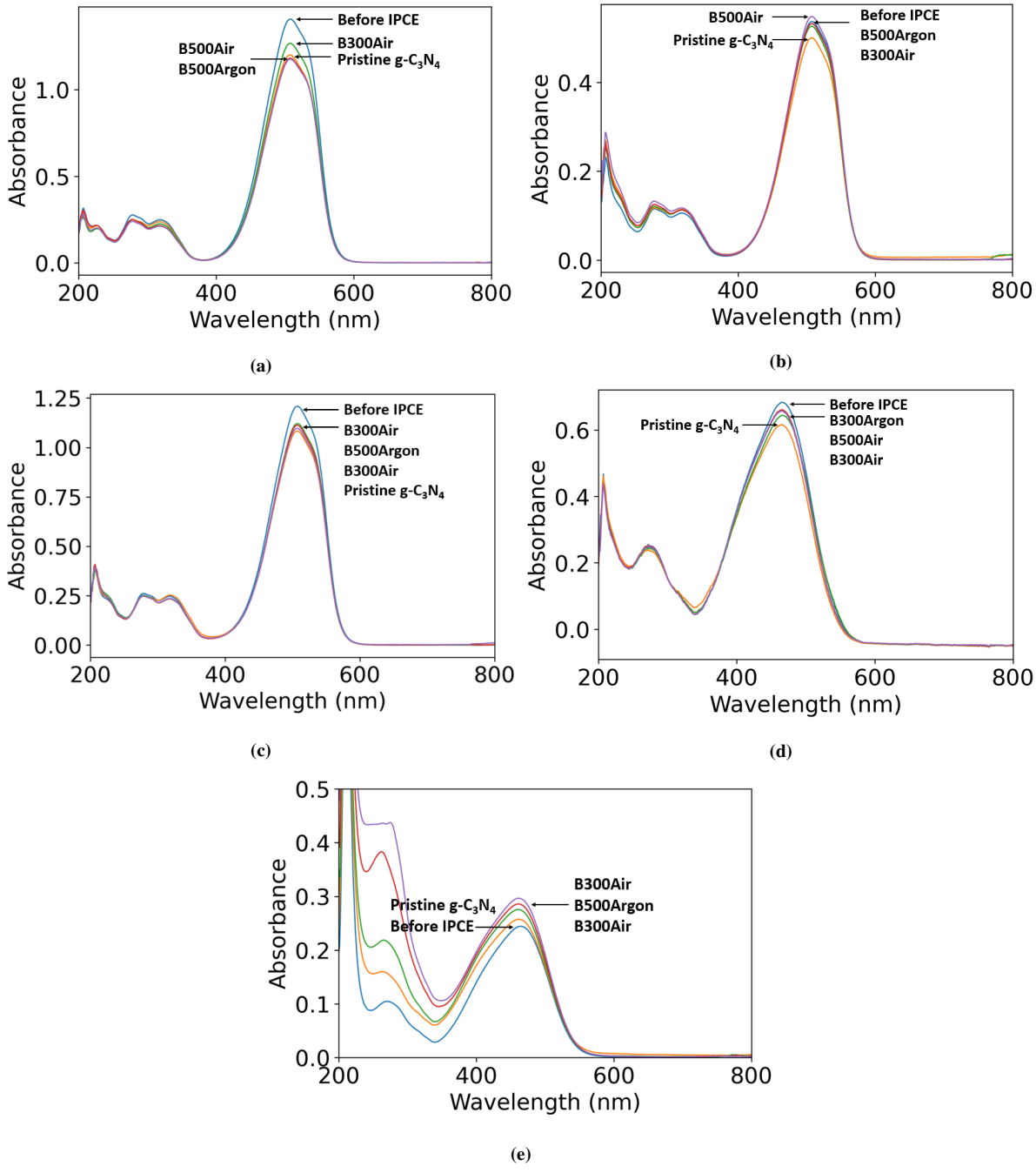

Figure F.1: UV-visible spectroscopy of methyl orange before and after IPCE with pristine and boron-doped g-C_3N_4 at a) pH of 0.3, b) pH of 1.0, c) pH of 2.1, d) pH of 4.4, and e) pH of 12.2. For the sample names in the figure, B denotes boron-doped, 300 and 500 denote the synthesis temperature, and Air and Argon denote the atmosphere used in the doping synthesis. The curves were measured from 800 nm to 200 nm with a bandwidth of 1 nm.

Table F.1: Calculated amount of oxidized methyl orange from measured absorption peaks obtained from UV-visible spectroscopy after IPCE tests. The results are given for pristine and boron-doped g-C_3N_4 in electrolytes containing various concentrations of methyl orange and different pH. For the sample names in the table, B denotes boron-doped, 300 and 500 denote the synthesis temperature, and Air and Argon denote the atmosphere used in the doping synthesis.

pH		Absorption peak	Oxidized methyl orange (%)
0.3	MO before	1.408	
	MO after, pristine g-C_3N_4	1.200	14.8
	MO after, B300Air	1.268	9.9
	MO after, B500Air	1.182	16.1
	MO after, B500Argon	1.176	16.5
1.0	MO before	0.536	
	MO after, pristine g-C_3N_4	0.500	6.8
	MO after, B300Air	0.526	2.0
	MO after, B500Air	0.548	0.0
	MO after, B500Argon	0.532	0.9
2.1	MO before	1.209	
	MO after, pristine g-C_3N_4	1.084	10.4
	MO after, B300Air	1.121	7.2
	MO after, B500Air	1.097	9.2
	MO after, B500Argon	1.113	8.0
4.4	MO before	0.684	
	MO after, pristine g-C_3N_4	0.616	9.9
	MO after, B300Air	0.645	5.7
	MO after, B500Air	0.657	3.9
	MO after, B500Argon	0.661	3.3
12.2	MO before	0.244	
	MO after, pristine g-C_3N_4	0.257	0.0
	MO after, B300Air	0.276	0.0
	MO after, B500Air	0.297	0.0
	MO after, B500Argon	0.286	0.0

Measured absorption spectra were also obtained for the MO solution during the degradation experiment with pristine g-C_3N_4 and B500Argon for a pH of 2.2 and 4.4. Here, the absorbance was measured every 15 minutes for a total duration of 60 minutes. The resulting spectra are given in Figures F.2 and F.3, where a slight decrease in MO concentration with time is observed for all samples. Additionally, the degradation experiment was performed for B500Argon without platinum at a pH of 4.4 to investigate the effect of the co-catalyst. The results are given in Figure F.4, where the resulting amount of degraded MO is approximately the same for B500Argon with and without platinum.

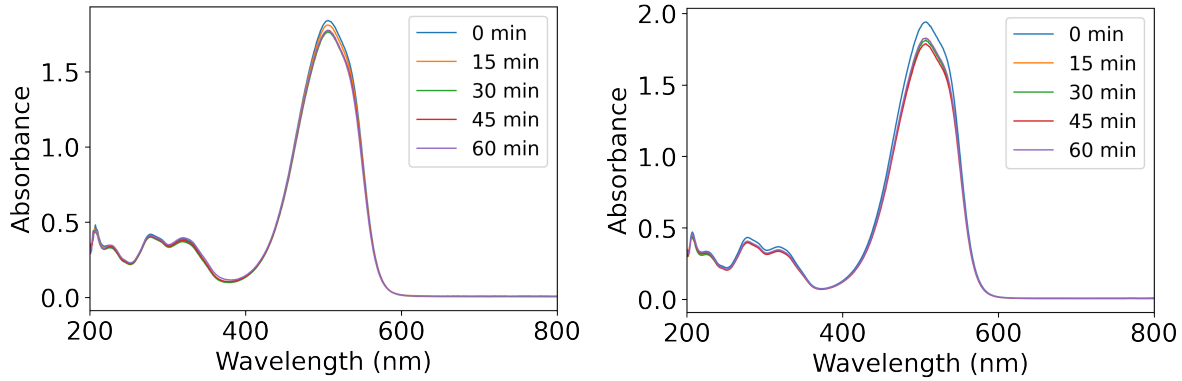

Figure F.2: Degradation of methyl orange by a) pristine g-C_3N_4 and b) B500Argon with time at a pH of 2.2. Here, B denotes boron-doped, 500 denotes the synthesis temperature, and Argon denotes the atmosphere used in the doping synthesis. The curves were measured from 800 nm to 200 nm with a bandwidth of 1 nm.

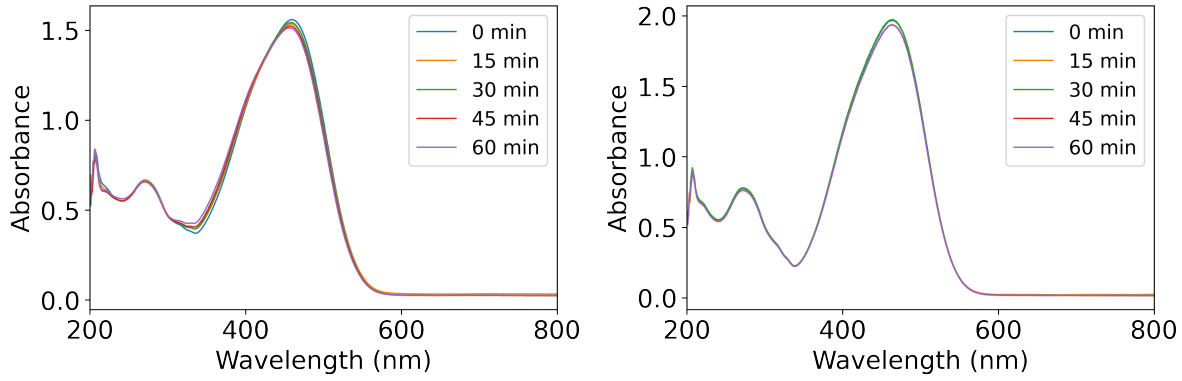

Figure F.3: Degradation of methyl orange by a) pristine g-C_3N_4 and b) B500Argon with time at a pH of 4.4. Here, B denotes boron-doped, 500 denotes the synthesis temperature, and Argon denotes the atmosphere used in the doping synthesis. The curves were measured from 800 nm to 200 nm with a bandwidth of 1 nm.

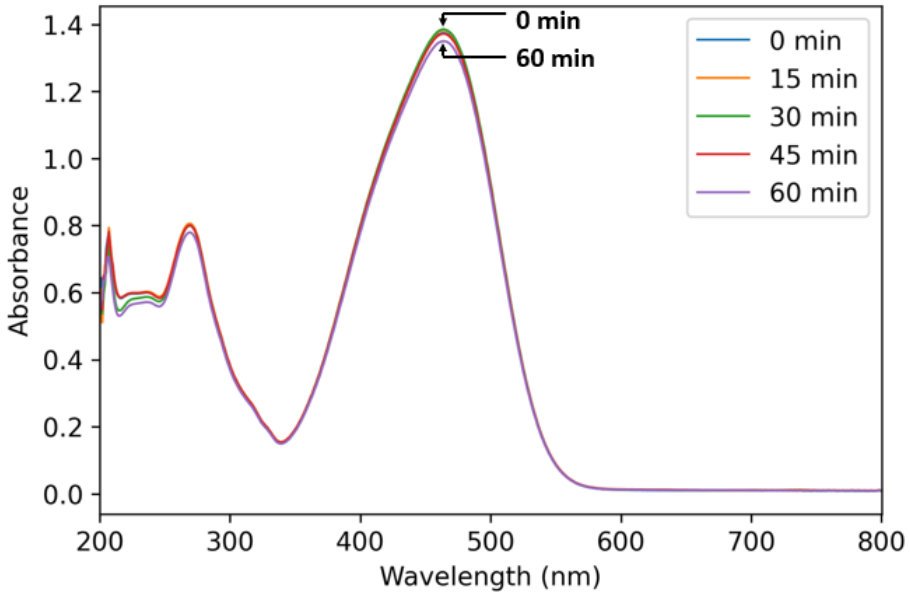

Figure F.4: Degradation of methyl orange by B500Argon without platinum with time at a pH of 4.4. Here, B denotes boron-doped, 500 denotes the synthesis temperature, and Argon denotes the atmosphere used in the doping synthesis. The curves were measured from 800 nm to 200 nm with a bandwidth of 1 nm.

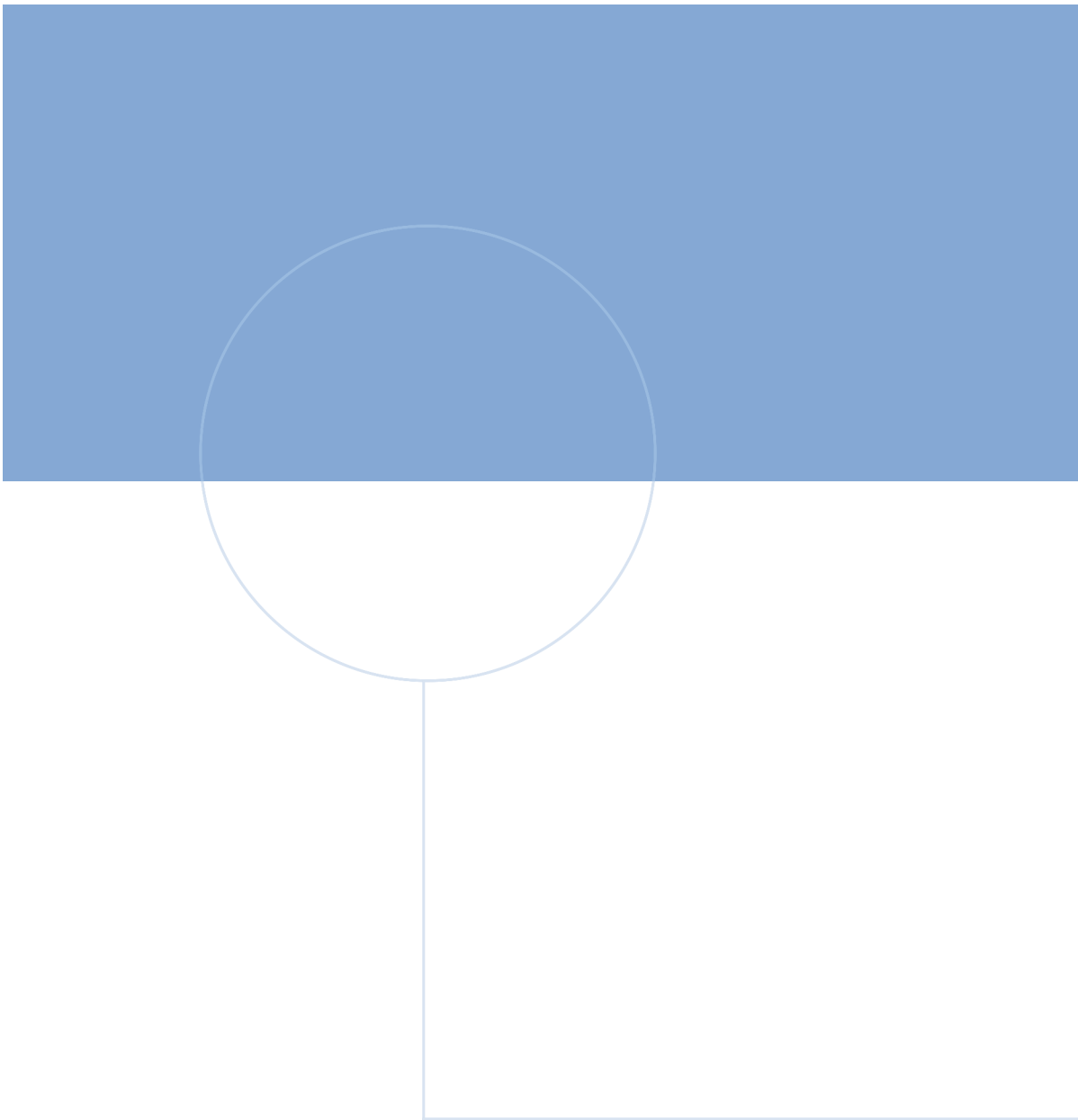

NTNU

Norwegian University of
Science and Technology